Efficient Singlet-triplet-spin-qubit-to-photon Interface Assisted by a Photonic Crystal Cavity

Von der Fakultät für Elektrotechnik und Informationstechnik der Rheinisch-Westfälischen Technischen Hochschule Aachen zur Erlangung des akademischen Grades eines Doktors der Ingenieurwissenschaften genehmigte Dissertation vorgelegt von

Kui Wu, M. Sc.
aus Hunan, China

Berichter:
Univ.-Prof. Dr. Jeremy Witzens
Univ.-Prof. Dr. Hendrik Bluhm

Tag der mündlichen Prüfung: 16.04.2026

Abstract

Semiconductor qubits implemented on semiconductor platforms are important building blocks for future quantum communication and quantum computation systems, which promise unprecedented communication security and computation efficiency for certain tasks. One important enabler for such systems is the interconnection of distant semiconductor quantum bits (qubits) by flying qubits, quantum information encoded in photons, in an efficient and coherent way. The goal of this dissertation is the design and fabrication of an efficient optical interface between a single mode fiber and a gate-defined double quantum dot (GDQD) hosting a singlet-triplet spin qubit on a 220 nm GaAs/AlGaAs heterostructure membrane. This interface should enhance the extraction efficiency of the photons, to which the quantum information is transferred from the spin qubit and that are emitted by an optically active quantum dot (OAQD) defined by the same gate system, by means of optical nanostructures and coupling them into a free-space Gaussian mode that can be straightforwardly collected by a single mode fiber.

In this dissertation, we successfully conceived and modeled a novel optical interface assisted by a photonic crystal cavity that provides substantial enhancement of the optical coupling efficiency. The photonic crystal cavity provides in-plane optical confinement, efficient out-coupling to an ideal free-space Gaussian beam, while accommodating the gate wiring and the electrical connectivity required by the GDQD and OAQD. To further increase the extraction efficiency, a bottom gold reflector is placed under the membrane to recycle the photons and further improve the beam shaping via coherent interaction. A noteworthy feature of this design is that all the essential components can be lithographically defined and deterministically fabricated on the GaAs/AlGaAs heterostructure membrane, which greatly increases the scalability of on-chip integration. According to our modeling results, the interface provides an overall coupling efficiency of 28.7% into a free-space Gaussian beam, assuming an SiO_2 interlayer fills the space between the reflector and the membrane, which is already an order of magnitude more than for the unpatterned membrane. The performance can

be further increased by removing this SiO_2 interlayer below the photonic crystal. In this case, the overall efficiency is modeled to be 48.5%.

Experimental characterization of the photonic crystal cavity was implemented by room temperature cross-polarization reflection measurements and millikelvin photoluminescence measurements. In reflection measurements, the photonic crystal cavities were illuminated by a tunable laser, and cross-polarized reflections were investigated for both intensity and beam profile. From the recorded far-field reflection patterns and the power spectra, we confirmed the desired Gaussian emission patterns. In photoluminescence experiments at millikelvin temperatures, the photonic crystal cavities were excited by a tunable laser above the bandgap of GaAs under applied gate voltages. From preliminary results, we reproduced the expected Stark-shifted emission spectra of the heterostructure membrane and observed promising emission peaks that might be the desired cavity enhancement.

Kurzfassung (German)

Halbleiter-Qubits, die auf Halbleiterplattformen realisiert werden, stellen wichtige Bausteine für zukünftige Systeme der Quantenkommunikation und Quanteninformationverarbeitung dar, die für bestimmte Anwendungen eine bislang unerreichte Kommunikationssicherheit und Recheneffizienz versprechen. Eine zentrale Voraussetzung für solche Systeme ist die effiziente und kohärente Kopplung räumlich getrennter Halbleiter-Qubits über sogenannte „fliegende Qubits“, also in Photonen kodierte Quanteninformation. Ziel dieser Dissertation ist das Design und die Realisierung einer effizienten optischen Schnittstelle zwischen einer Einmodenfaser und einem gate-definierten Doppel-Quantenpunkt (GDQD), der ein Singulett-Triplett-Spin-Qubit auf einer 220 nm dünnen GaAs/AlGaAs-Heterostrukturmembran beherbergt. Diese Schnittstelle soll die Auskopplungseffizienz der Photonen erhöhen, auf die die Quanteninformation vom Spin-Qubit übertragen wird und die von einem optisch aktiven Quantenpunkt (OAQD), der durch dasselbe Gate-System definiert ist, emittiert werden, indem optische Nanostrukturen genutzt und die Photonen in eine frei propagierende gaußsche Mode gekoppelt werden, die anschließend effizient in eine Einmodenfaser eingekoppelt werden kann.

In dieser Arbeit wurde eine neuartige optische Schnittstelle unter Verwendung eines photonischen Kristallresonators erfolgreich konzipiert und modelliert, die eine deutliche Verbesserung der optischen Kopplungseffizienz ermöglicht. Der photonische Kristallresonator sorgt für eine laterale optische Konfinierung, eine effiziente Auskopplung in einen idealen gaußschen Freistrahl sowie die Integration der Gate-Verdrahtung und der elektrischen Kontakte, die für den Betrieb von GDQD und OAQD erforderlich sind. Zur weiteren Steigerung der Extraktionseffizienz wurde unterhalb der Membran ein Goldreflektor integriert, um die emittierten Photonen zu rezyklieren und durch kohärente Wechselwirkung zusätzlich die Strahlformung zu verbessern. Ein wesentlicher Vorteil dieses Designs besteht darin, dass alle zentralen Komponenten lithographisch definiert und deterministisch auf der GaAs/AlGaAs-Heterostrukturmembran gefertigt werden können, was die Skalierbarkeit für die Integration auf einem Chip erheblich er-

höht. Den Modellierungsergebnissen zufolge erreicht die Schnittstelle eine Gesamtkopplungseffizienz von 28,7% in eine gaußsche Freiraummode, wenn eine SiO_2-Zwischenschicht den Raum zwischen Reflektor und Membran ausfüllt, was bereits eine Größenordnung über der Effizienz einer unstrukturierten Membran liegt. Durch das Entfernen dieser SiO_2-Zwischenschicht unterhalb des photonischen Kristalls kann die Effizienz weiter gesteigert werden; in diesem Fall ergibt sich modellhaft eine Gesamteffizienz von 48,5%.

Die experimentelle Charakterisierung des photonischen Kristallresonators erfolgte mittels raumtemperaturbasierter kreuzpolarisierter Reflexionsmessungen sowie Photolumineszenzmessungen bei Millikelvin-Temperaturen. In den Reflexionsmessungen wurden die photonischen Kristallresonatoren mit einem abstimmbaren Laser angeregt, und die kreuzpolarisierten Reflexionen wurden hinsichtlich Intensität und Strahlprofil untersucht. Anhand der aufgezeichneten Fernfeld-Reflexionsmuster und Leistungsspektren konnten die angestrebten gaußschen Emissionsprofile bestätigt werden. In Photolumineszenzexperimenten bei Millikelvin-Temperaturen wurden die photonischen Kristallresonatoren mit einem abstimmbaren Laser oberhalb der Bandlücke von GaAs unter angelegten Gate-Spannungen angeregt. Erste Ergebnisse zeigen die erwarteten, durch den Stark-Effekt verschobenen Emissionsspektren der Heterostrukturmembran sowie vielversprechende Emissionspeaks, die auf die gewünschte Resonatorverstärkung hindeuten könnten.

List of Publications

Journal Articles

- **K. Wu**, S. Kindel et al., "Modeling an efficient singlet-triplet-spin-qubit-to-photon interface assisted by a photonic crystal cavity." *Physical Review Applied* 21, 054052 (2024).
- **K. Wu**, B. Marzban et al., "High-efficiency gate-defined quantum dot to single mode fiber interface assisted by a photonic crystal cavity". *AIP Advances* 10, 115016 (2020).
- B. Marzban, L. Seidel, T. Liu, **K. Wu** et al., "Strain Engineered Electrically Pumped SiGeSn Microring Lasers on Si". *ACS Photonics* 10, 217-224 (2023).

Conference Proceedings

- **K. Wu** et al. "An Efficient Singlet-Triplet Spin Qubit to Fiber Interface Assisted by a Photonic Crystal Cavity." In: Witzens, J., Poon, J., Zimmermann, L., Freude, W. (eds) The 25th European Conference on Integrated Optics. ECIO 2024. Springer Proceedings in Physics, vol 402. Springer, Cham (2024).
- **K. Wu**, T. Descamps, B. Marzban et al., "Highly efficient spin qubit to photon interface assisted by a photonic crystal cavity," *Proc. SPIE* 11995, Physics and Simulation of Optoelectronic Devices XXX, 1199507 (2022).
- B. Marzban, L. Seidel, T. Liu, V. Kiyek, **K. Wu** et al., "Electrically pumped SiGeSn microring lasers," 2022 IEEE Photonics Society Summer Topicals Meeting Series (SUM), Cabo San Lucas, Mexico, pp. 1-1 (2022).
- C. Culotta-Lopez, **K. Wu**, and D. Heberling, "Radiation center estimation from near-field data using a direct and an iterative approach," 2017 Antenna Measurement Techniques Association Symposium (AMTA), Atlanta, GA, USA, pp. 1-6 (2017).

Education

2011.9 - 2015.6: **Bachelor of Science**, Information and Communication Engineering, Zhejiang University, Hangzhou, China.

2015.9 - 2020.8: **Master of Science**, Information and Telecommunication Technology, RWTH Aachen University, Aachen, Germany.

2016.9 - 2020.8: **Bachelor of Science**, Physics, RWTH Aachen University, Aachen, Germany.

2020.9 - 2025.9: **Reseach Assistant and PhD candidate**, Institute of Integrated Photonics (IPH), RWTH Aachen University, Aachen, Germany.

Acknowledgment

First of all, I would like to express my deepest gratitude to my supervisor, Prof. Dr. Jeremy Witzens. Without his guidance and dedication, this project would not have come into existence or reached completion. His knowledge, generosity, and keen scientific insight have guided me throughout my PhD journey. The knowledge and experience I have gained from him will remain a valuable and lasting part of my life.

I am grateful to Prof. Dr. Hendrik Bluhm and his group members– Sebastian Kindel, Tobias Hangleiter, and former member Dr. Thomas Descamps–for their collaboration and stimulating discussions. Without their contributions, the proposed concept could not have been fabricated or experimentally investigated.

I would also like to thank Dr. Bahareh Marzban, who supervised my master thesis, which became the foundation of this PhD project. Her effort, kindness, and guidance were essential for making this work possible.

Special thanks go to Prof. Dr. Beata Kardynal for her support of this project and for her insightful suggestions.

I would also like to thank Dr. Florian Merget, Dr. Georgios Sinatkas, Dr. Arijit Misra, Rebecca Rodrigo, and Dr. Ibrahim Ghannam for their valuable discussions and assistance.

Finally, I thank all the members of the Institute for Integrated Photonics for their kindness and collegiality, which created a supportive and inspiring working environment.

Contents

Chapter 1

Introduction

1.1 Quantum technology platforms

Quantum computation and communication are emerging technologies that utilize unusual characteristics of quantum systems, such as superposition and entanglement. In contrast to classical digital computation and communication, quantum solutions promise unprecedented advantages. For example, quantum key distribution protocols [1] allow for an unconditionally secure communication channel, thanks to the no-cloning principle of quantum states [2]. As a result, any eavesdropping on a quantum channel is not possible without being noticed by the users. On the other hand, classical digital signals can be detected and arbitrarily copied by a third person hidden from the sender and receiver, and complicated encryptions like the widespread asymmetric Rivest-Shamir-Adleman (RSA) algorithm are thus necessary to protect against eavesdropping.

However, encryption algorithms like RSA, which are practically unbreakable using classical digital computers, can be broken by a quantum computer with quantum bits (qubits) using the Shor algorithm [3]. The reason for the superior performance of quantum computers, for certain tasks like encryption breaking and parallel computing, is two-fold. Firstly, a quantum computer utilizes superposition states of its qubits, which allows for simultaneous manipulation of multiple states representing different data. Secondly, the memory space of the quantum computer is determined by the dimension of the Hilbert space, which scales exponentially with the number

of qubits.

Qubits, the most critical building blocks for quantum systems, are quantum two-level systems that should satisfy the DiVincenzo criteria [4, 5, 6]. To physically implement qubits, various nano-technology platforms attract the interest of researchers [7]. Some of the most well-known candidates are:

- **Semiconductor quantum dots**
  Semiconductor quantum dots confine single electrons or holes in nanoscale potential traps, where the spin or charge degree of freedom can serve as a qubit, for example, charge qubit, Loss-DiVincenzo single spin qubit [8], and singlet-triplet spin qubit [9, 10]. Thanks to the mature semiconductor fabrication technologies, a high integration density of quantum dots on a single chip can be achieved either by growing self-assembled quantum dots (SAQDs) [11, 12, 13] or by patterning gate-defined (double) quantum dots (GDQDs) [14, 15] defined by microscopic metal gates. In a GDQD, single electrons are trapped by tunable electrostatic potential minima applied to a two-dimensional electron gas (2DEG) with the metal gates.

- **Color centers in diamond**
  Color centers, such as nitrogen-vacancy (NV) centers, are atom-scale defects or impurities in diamond. Those imperfections in the diamond lattice create isolated electron energy states inside the bandgap, which are optically addressable. Due to the large bandgap of diamond, the electron spin qubits created in this manner have long coherence times even at room temperature [16, 17].

- **Superconducting circuits**
  Superconducting qubits, implemented by integrating Josephson junctions into electrical circuits, are mesoscopic quantum devices that operate at millikelvin (mK) temperatures. The most promising candidate is the transmon qubit [18]. They offer fast gate times, strong nonlinearities, and have achieved the highest levels of scalability among current quantum computing platforms [7, 19, 20].

- **Trapped ions**

Trapped ion qubits are encoded in the electronic states of isolated single ions confined in electromagnetic traps and manipulated with laser light. Since the ions are free-standing in vacuum, there is no significant noise source that causes decoherence. As a result, the qubits feature extremely long coherence times and high-fidelity gate operations [7], making them ideal for precision quantum information processing. On the other hand, scaling up the number of ions while maintaining control remains a major challenge [21].

1.2 Quantum interconnection

Interconnecting distant stationary qubits, realized by the aforementioned platforms, is another crucial prerequisite for quantum technology applications. A natural choice for implementing such interconnections is to use photons as flying qubits to distribute quantum information between spatially separated stationary qubits.

There are multiple advantages of using photons as information carriers. First, the well-established worldwide optical fiber network provides a solid infrastructure for quantum optical research. The low-loss optical fibers used in long-haul communication (around 0.3 dB/km at 1550 nm) are ideal for transmitting photonic qubits. However, due to the no-cloning theorem, a photonic qubit cannot be duplicated by any optical amplifier without destroying its quantum entanglement with other qubits. As a result, optical loss during transmission is critical and must be as low as possible. This also means that photonic qubits cannot simply be amplified by the erbium-doped fiber amplifiers (EDFAs) integrated into existing intercontinental fiber networks.

To overcome this challenge and distribute quantum entanglement over long distances, quantum repeaters [22] are employed instead of optical amplifiers. Quantum repeaters divide the communication channel into shorter segments where optical loss is manageable. Entanglement is generated within each segment and then swapped between adjacent repeaters, thereby establishing entanglement across the two ends of the entire channel.

A second advantage of using photons is their ability to interact with all

classes of stationary qubits realized in different physical platforms. Quantum dots fabricated on direct-bandgap semiconductors such as GaAs or InGaAs are naturally optically active. Entanglement between the exciton spin and the polarization of emitted photons has been experimentally demonstrated [23]. The optical interaction strength can be enhanced by the Purcell effect [24] by integrating the emitter into well-designed nanophotonic resonators such as photonic crystal cavities [25, 26], nanowire-based cavities [27], or micropillar cavities [28, 29]. Similar Purcell enhancement is possible for color centers in diamond, where certain defect states are optically active, and for trapped ions, whose internal electronic transitions can be optically addressed when the dipole selection rule is satisfied.

In contrast, superconducting qubits operate at much lower transition energies. The energy splitting between the ground and first excited states in a typical transmon qubit corresponds to a frequency of about 5 GHz (around 20 μeV) [18]. As a result, superconducting qubits only interact with microwave photons, whose energies are orders of magnitude lower than optical photons. To interface superconducting qubits with optical quantum networks, microwave-to-optical conversion interfaces are required [30].

In order to bridge stationary qubits and photonic qubits, optical interfaces are necessary to collect the emitted photons and couple them into a single-mode fiber, or vice versa, from a single-mode fiber to the quantum emitter, in an efficient and coherent way. Ideally, the optical interface should achieve near-unity efficiency while preserving the quantum coherence of the system. For stationary qubit systems based on trapped ions, superconducting circuits, color centers, and excitonic states in quantum dots, the coherence between the emitted photon and the stationary qubit is generally preserved if the quantum states before and after the optical transition are well-defined. However, this is not the case for semiconductor qubits defined purely by electron spins. Since the photon emission process arises from the recombination of an electron and a hole, preserving coherence requires that both the electron and hole spin states remain well-defined or are decoupled from each other, for example, through g-factor engineering [31, 32, 33, 34] or by using a coherent information transfer protocol [35].

To enhance the efficiency of the optical interface, carefully designed opti-

cal lens systems with high collection efficiency and minimal optical losses are commonly employed. Beyond conventional optics, nanophotonic structures play a central role in further improving photon extraction efficiency [36]. These structures enable photons to be funneled out of high-refractive-index semiconductor materials into a well-directed free-space mode, which can then be mode-matched to a single-mode fiber. Examples of such nanophotonic structures include distributed Bragg reflectors [37], microlenses [38], bull's-eye cavities [39, 40], nanowire-based cavities [27], and photonic crystal cavities [25, 26, 41, 42].

Such nanophotonic optical interfaces are particularly attractive for semiconductor quantum dots because they can be monolithically integrated using top-down nanofabrication directly on the same chip that hosts the qubits. In contrast, implementing similar structures for trapped ions is far more challenging, as the ions are suspended in vacuum rather than embedded in a solid-state medium. Likewise, for color centers in diamond, integration is limited by the difficulty of fabricating high-quality nanophotonic structures in diamond, which is chemically and mechanically hard to process [43].

One other advantage of using semiconductor platforms is their potential for large-scale integration, enabling thousands- or even millions- of qubits on a single chip. This is possible thanks to the mature semiconductor nanofabrication technologies. In contrast to SAQDs, whose positions are random due to the Stranski-Krastanow growth process [44], GDQDs have their locations determined by lithographically patterned metal gates, allowing deterministic placement. The combination of GDQDs with nanophotonic interfaces fabricated around them enables a fully lithographically defined fabrication process [10], paving the way toward scalable quantum architectures.

GDQD spin qubits in GaAs have fulfilled the necessary requirements for quantum information processing, including initialization, readout, and coherent control [45, 46, 10, 47, 48, 49]. While spin qubits in isotopically purified ^{28}Si demonstrate significantly longer coherence times [50, 51], the indirect bandgap of silicon is not efficient for light emission. As a result, developing an efficient optical interface for spin qubits based on Si remains challenging. In contrast, the direct bandgap of GaAs enables straightforward spin-photon conversions, positioning it as a favorable material for realizing

an efficient optical interface.

1.3 Motivation and scope

Motivated by the growing interest in optical interfaces for semiconductor spin qubits, this thesis presents the design and experimental characterization of a fully lithographically defined and efficient interface between singlet-triplet spin qubits and photons, mediated by a photonic crystal cavity (PCC) (Figure 1.1).

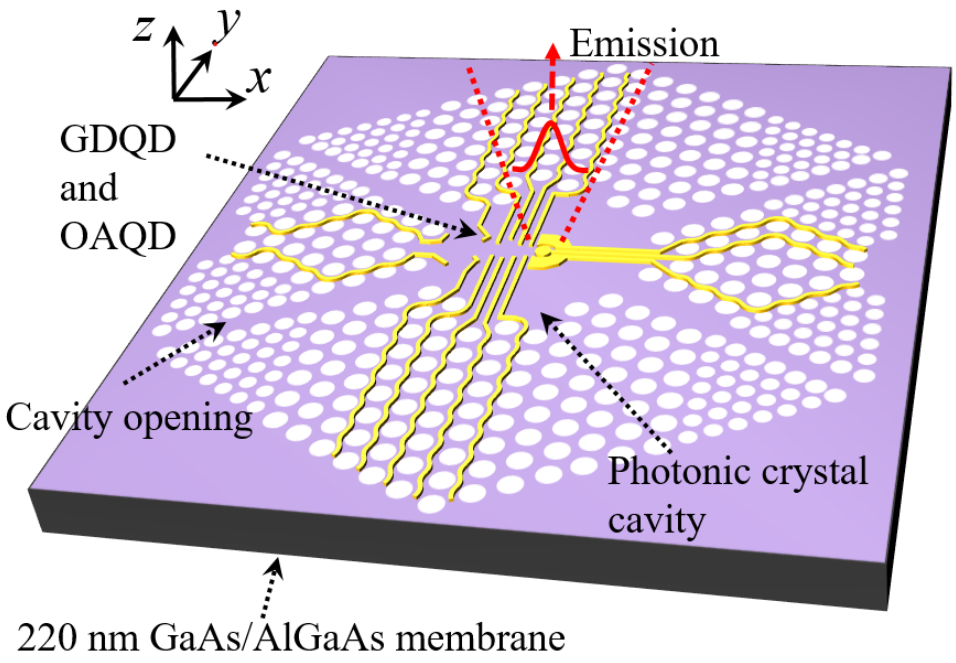

Figure 1.1: Schematic overview of the optical interface, comprising the GaAs/AlGaAs membrane, the PCC, and the electrode system. A detailed structural description is given in Chapter 3. Figure adapted from our publication, Ref. [41].

The spin qubit is encoded in the singlet and triplet states of two electrons confined in a GDQD. Electrical control is achieved via metallic gates patterned on both sides of a 220 nm-thick GaAs/AlGaAs heterostructure membrane [41, 52].

To enable coherent conversion between photonic and spin qubits, a gate-

defined optically active quantum dot (OAQD) is incorporated adjacent to the GDQD. This OAQD serves as an exciton trap, where photogenerated holes are also electrostatically confined, thereby mitigating carrier loss. A transfer protocol [35] based on adiabatic tunnel coupling is employed to coherently map the photogenerated electron onto the spin state of the singlet-triplet qubit with a fidelity of 84%.

Efficient photon-exciton coupling is achieved by embedding the OAQD at the center of a carefully engineered PCC. The cavity provides strong in-plane optical confinement and couples light into a Gaussian free-space mode via Bragg scattering. Its geometry is designed to remain compatible with the metallic gate layout: the gate electrodes are routed between etched holes with sufficiently high overlay precision (see Chapter 5). Additionally, four cavity openings are introduced to allow electrical connectivity to a quantum dot charge sensor without compromising the optical confinement at the target wavelength.

Based on the modeling results, the interface achieves an overall coupling efficiency of 28.7% from the OAQD into a free-space Gaussian beam when an SiO_2 interlayer is used to fill the space between the bottom reflector (not shown in Figure 1.1) and the membrane. This efficiency is already an order of magnitude higher than that of an unpatterned membrane. The performance can be further enhanced by undercutting the SiO_2 interlayer beneath the photonic crystal region, which increases the modeled efficiency to 48.5%. These results demonstrate the strong potential of this approach for realizing efficient and scalable quantum information architectures that integrate GDQDs with photonic crystal cavities.

Experimental characterization of the photonic crystal cavities was performed using room-temperature cross-polarized reflectance measurements. In this method, the cavities are illuminated with a tunable-wavelength laser, and the cross-polarized reflected light is analyzed in terms of both intensity and far-field beam profile. From the measured reflection spectra and far-field patterns, we confirm the expected Gaussian emission profile and cavity enhancement. Preliminary mK photoluminescence results are also presented and discussed in Chapter 7.

1.4 Thesis organization

This thesis is organized as follows:

- Chapter 2 introduces the theoretical background, including the singlet–triplet spin qubit, the transfer protocol for coherent information transfer, photonic crystals, and the theoretical description of an ideal 2D Gaussian beam.
- Chapter 3 details the geometries of the GDQD, OAQD, PCC, and cavity openings, including associated photonic bandgap calculations.
- Chapter 4 presents the full modeling methodology and the simulation results of the optical interface.
- Chapter 5 describes the device fabrication process, the experimental design, and scanning electron microscope (SEM) images of the fabricated samples.
- Chapter 6 reports the room-temperature cross-polarized reflectance measurements, including the experimental setup, measurement procedure, and analysis of the results.
- Chapter 7 presents preliminary results from millikelvin photoluminescence measurements.
- Chapter 8 concludes the thesis and provides an outlook on possible future directions.

Chapter 2

Theoretical Background

2.1 Singlet-triplet spin qubit

2.1.1 Basics of singlet-triplet spin qubit

The singlet-triplet spin qubit (ST qubit) uses the singlet spin state and one of the three triplet spin states as the computational basis. The two electrons defining the ST qubit are generally trapped in a gate-defined double quantum dot (GDQD) with an electrically tunable tunneling barrier and energy detuning between the two quantum dots [10]. The singlet and triplet spin states are

$$\begin{aligned} \text{Singlet state:} \quad & |S\rangle = \frac{1}{\sqrt{2}}\left(|\uparrow\downarrow\rangle - |\downarrow\uparrow\rangle\right) \\ \text{Triplet states:} \quad & |T_+\rangle = |\uparrow\uparrow\rangle \\ & |T_0\rangle = \frac{1}{\sqrt{2}}\left(|\uparrow\downarrow\rangle + |\downarrow\uparrow\rangle\right) \\ & |T_-\rangle = |\downarrow\downarrow\rangle\,. \end{aligned} \tag{2.1}$$

Depending on which triplet state is used in the computational basis, there are three types of ST qubits: the ST_0, ST_+, and ST_- qubits. Compared to the single-spin qubit (or the Loss-DiVincenzo qubit [8]), which requires AC magnetic fields to drive Rabi oscillations and manipulate the spin state, ST qubits feature rapid fully electrical control based on the electrically tunable

exchange interaction [53, 54], which is their main advantage. The control scheme will be introduced in Section 2.1.2.

Among the three types of ST qubits, the ST_0 qubit is particularly interesting because the $|S\rangle$ state has total spin zero, while the $|T_0\rangle$ state has total spin one but zero spin projection ($m_s = 0$). As a result, the ST_0 qubit is decoupled from fluctuations of global magnetic fields and thus exhibits a longer coherence time [10]. In contrast, the energies of the $|T_-\rangle$ and $|T_+\rangle$ states shift with the global magnetic field strength due to the Zeeman effect. In the following sections, we focus on the ST_0 qubit. An introduction to the ST_+ and ST_- qubits is available in Ref. [54].

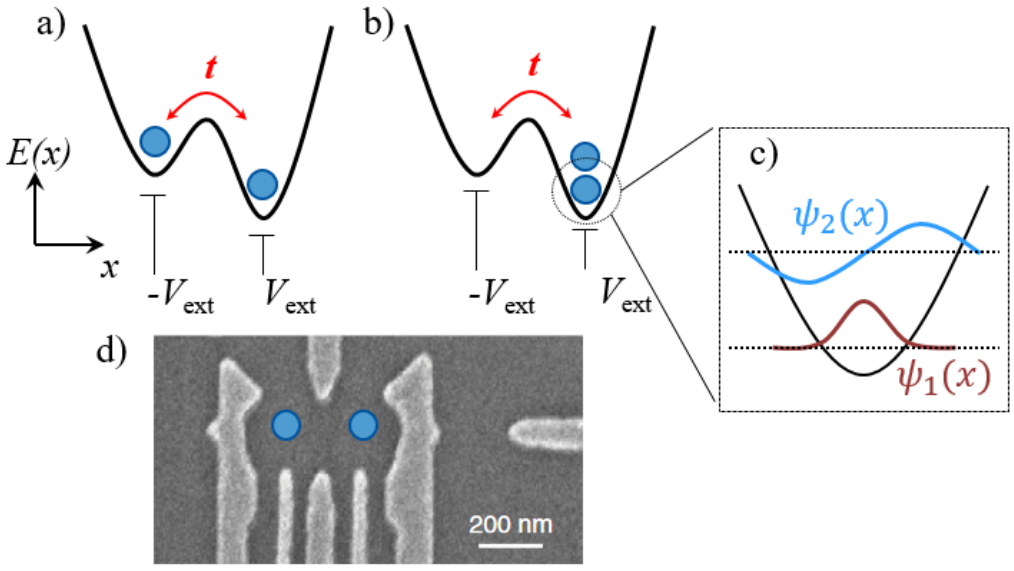

Figure 2.1: Schematic illustration of a double quantum dot hosting two electrons (blue circles). t denotes the inter-dot tunnel coupling rate. The potential of each quantum dot can be tuned by an external voltage V_{ext}. a) The (1,1) charge configuration, b) the (0,2) configuration, c) the two lowest-energy orbital wavefunctions in the right quantum dot, and d) a physical realization of a GDQD hosting two electrons on a GaAs/AlGaAs heterostructure (SEM image adapted from Ref. [10]).

To fully understand the mechanisms of ST_0 qubits, we start by considering a double quantum dot as shown in Figure 2.1. A double quantum dot consists of two adjacent quantum dots separated by a tunable potential

barrier. By varying the barrier height, the inter-dot tunneling rate t can be tuned. The potential of each quantum dot can also be adjusted by the corresponding gate voltage, denoted by V_{ext}. In Figure 2.1(a), one electron is confined in each dot, corresponding to the (1,1) charge configuration, while in (b), both electrons occupy the right dot, corresponding to the (0,2) configuration. We label charge configurations by (m, n), where m and n are the numbers of electrons in the left and right dots, respectively. In the following discussion, we focus on the (1,1) and (0,2) charge states.

According to the Pauli exclusion principle, the total two-electron wavefunction must be antisymmetric under the exchange of the two electrons. For convenience, we denote the symmetric orbital wavefunctions by $S(1,1)$ and $S(0,2)$, and the antisymmetric orbital wavefunctions by $A(1,1)$ and $A(0,2)$. Examples are

$$\begin{aligned} S(0,2) &= \psi_1(x_1)\,\psi_1(x_2), \\ A(0,2) &= \frac{1}{\sqrt{2}}\left[\psi_1(x_1)\psi_2(x_2) - \psi_1(x_2)\psi_2(x_1)\right], \end{aligned} \tag{2.2}$$

where $\psi_1(x)$ and $\psi_2(x)$ are the ground and first-excited single-electron orbital wavefunctions in the right quantum dot, as shown in Figure 2.1(c), and x_1, x_2 are the coordinates of both electrons. For $S(1,1)$ and $A(1,1)$, the construction is analogous once the single-particle orbitals of the left dot are known. In particular, the $A(1,1)$ state can be built from the lowest single-particle states of the two separate dots when inter-dot tunnel coupling is neglected, with antisymmetry arising from the exchange of the electrons between the two sites.

As a result, there are four allowed combinations of orbital and spin states consistent with the Pauli exclusion principle: $S(1,1) \otimes |S\rangle$, $A(1,1) \otimes |T_{0,\pm}\rangle$, $S(0,2) \otimes |S\rangle$, and $A(0,2) \otimes |T_{0,\pm}\rangle$. We omit the tensor product sign later for simplicity. We define the detuning energy ϵ as the energy difference between the $S(1,1)$ and the $S(0,2)$ charge states, and plot the energy diagram in Figure 2.2. The detuning energy ϵ can be tuned experimentally by adjusting the gate voltage V_{ext}, as illustrated in Figure 2.1.

In Figure 2.2(a), we first consider the case without tunnel coupling ($t = 0$). In this limit, the energies of the $S(1,1)$ and $S(0,2)$ singlet states

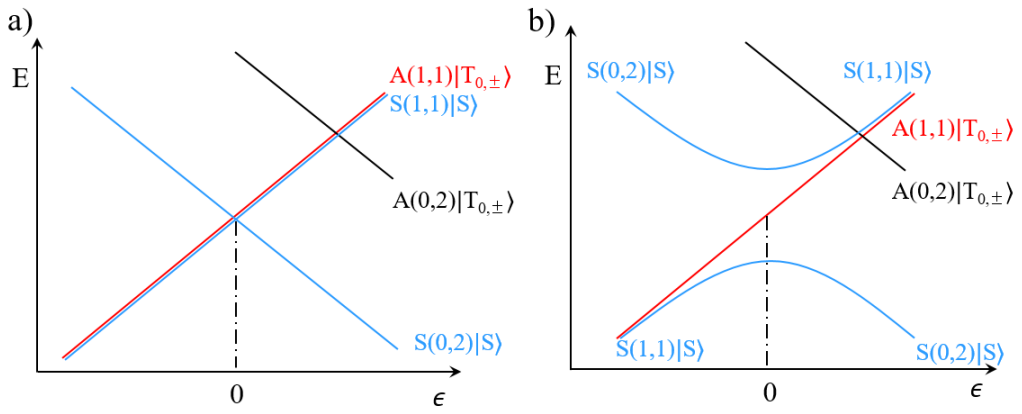

Figure 2.2: Energy diagram of the charge and spin states of two electrons in a double quantum dot. The energies of the different states are plotted as a function of detuning ϵ for (a) zero tunnel coupling ($t = 0$) and (b) finite tunnel coupling ($t > 0$).

cross at $\epsilon = 0$ by definition. The $A(0, 2)$ triplet state lies higher in energy than $S(0, 2)$ because one electron must occupy the first excited orbital $\psi_2(x)$. In contrast, the energy difference between $S(1, 1)$ and $A(1, 1)$ is negligible, since both electrons occupy the ground orbitals of spatially separated dots when the dots are sufficiently far apart [53].

In Figure 2.2(b), we include a finite tunnel coupling ($t > 0$). The $S(1, 1)$ and $S(0, 2)$ singlet states then hybridize near $\epsilon = 0$, producing an avoided crossing characteristic of tunnel-coupled systems. Triplet states can also hybridize between the $A(1, 1)$ and $A(0, 2)$ configurations, but this effect is not relevant for the present discussion and is omitted in Figure 2.2(b) for clarity.

The degeneracy between the triplet spin states $|T_{0,\pm}\rangle$ can be lifted using the Zeeman effect by applying an external magnetic field, as shown in Fig. 2.3. The $A(1, 1)\,|T_0\rangle$ state and the lower branch of the hybridized $|S\rangle$ state form the computational basis of the ST_0 qubit. We define the exchange splitting $J(\epsilon)$ as the energy difference between the triplet $A(1, 1)\,|T_0\rangle$ state and the hybridized singlet state, which is $J(\epsilon) = E_{T_0} - E_S$. The exchange splitting depends on the detuning ϵ and can therefore be electrically controlled via V_{ext}. This tunable exchange splitting plays a central role in the operation of the ST_0 qubit, as discussed in the following section.

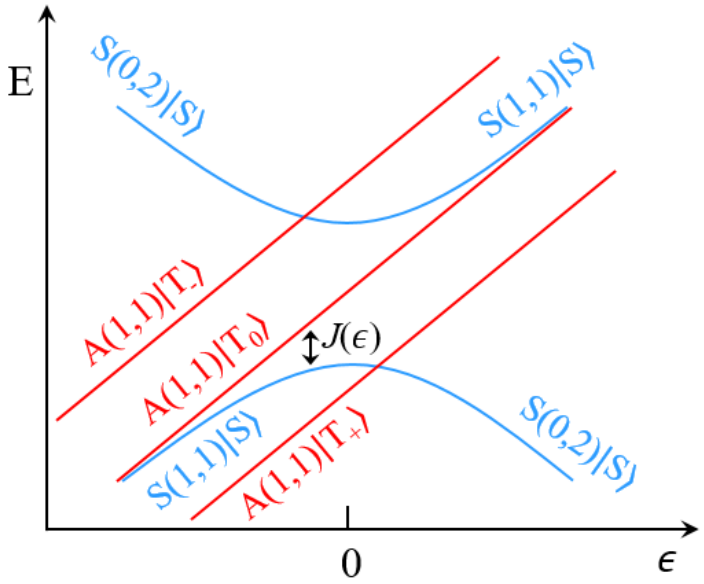

Figure 2.3: Energy diagram in the presence of an external magnetic field. The degeneracy between the three triplet spin states is lifted due to the Zeeman effect. $J(\epsilon)$ denotes the exchange splitting between the $|T_0\rangle$ state and the hybridized $|S\rangle$ state, which form the computational basis of the ST_0 qubit.

2.1.2 Initialization and control

The initialization of an ST_0 qubit consists of three steps:

1. Load two electrons into the double quantum dot from the surrounding two-dimensional electron gas (2DEG). This is achieved by tuning the gate-controlled tunnel barrier between the quantum dot and the 2DEG [10].

2. Wait until the system relaxes into the lowest-energy $|S\rangle$ state under a large positive detuning energy ϵ.

3. Adiabatically tune ϵ to the negative range to adjust the exchange splitting $J(\epsilon)$ to the desired value range.

In the two-level subspace spanned by the $|T_0\rangle$ and $|S\rangle$ states, the Hamiltonian considering only the exchange splitting is

$$\hat{H} = \begin{pmatrix} J(\epsilon) & 0 \\ 0 & 0 \end{pmatrix}. \tag{2.3}$$

To drive transitions between the $|T_0\rangle$ and $|S\rangle$ states, non-zero off-diagonal elements are required. For ST_0 qubits in GaAs, the hyperfine magnetic field B_{nuc} (the Overhauser field), resulting from the non-zero spin of surrounding nuclei, has a field strength difference ΔB_{nuc} between the left and right quantum dots. As a result, the degeneracy between the $|\uparrow\downarrow\rangle$ and $|\downarrow\uparrow\rangle$ spin states is lifted by $g\mu_B\Delta B_{\text{nuc}}$, where $g = -0.44$ is the electron g-factor in GaAs and $\mu_B = e\hbar/2m_e$ is the Bohr magneton. This energy splitting leads to a mixing between the $|T_0\rangle$ and $|S\rangle$ states. The resulting Hamiltonian becomes

$$\hat{H} = \begin{pmatrix} J(\epsilon) & \frac{1}{2}g\mu_B\Delta B_{\text{nuc}} \\ \frac{1}{2}g\mu_B\Delta B_{\text{nuc}} & 0 \end{pmatrix}. \tag{2.4}$$

The nuclear field gradient ΔB_{nuc} evolves slowly (over $10\,\mu$s), in contrast to the nanosecond-scale control of $J(\epsilon)$ [53, 10]. By employing a closed-loop control algorithm to tune $J(\epsilon)$, high-fidelity ($> 99.5\%$) gate operations and qubit manipulations can be achieved [45, 46].

2.1.3 Spin-to-charge readout

The readout of an ST_0 qubit utilizes the spin-to-charge conversion enabled by the Pauli spin blockade [53]. In combination with a sensitive charge detector, such as a quantum point contact (QPC) or single-electron transistor (SET), which are capacitively coupled to the double quantum dot, the different charge states in the double quantum dot can be discriminated by monitoring the conductance of the QPC or SET charge detector [48, 55, 56].

Figure 2.4 schematically shows the spin-to-charge conversion. The basic idea is to adiabatically change the detuning energy ϵ from the negative value regime (ϵ_1) where both electrons are localized in separate quantum dots (the $S(1,1)\,|S\rangle$ or $A(1,1)\,|T_0\rangle$ states) to a regime (ϵ_2) where they can occupy the same dot. Due to Pauli exclusion, the $S(1,1)\,|S\rangle$ state can be adiabatically transferred into the $S(0,2)\,|S\rangle$ state, while the $A(1,1)\,|T_0\rangle$ state cannot be transferred into the $A(0,2)\,|T_0\rangle$ state because it lies higher in energy, as already illustrated in Figure 2.2.

As a result, the two spin states result in different charge configurations: the singlet spin state maps to $S(0,2)$, and the triplet remains in $A(1,1)$.

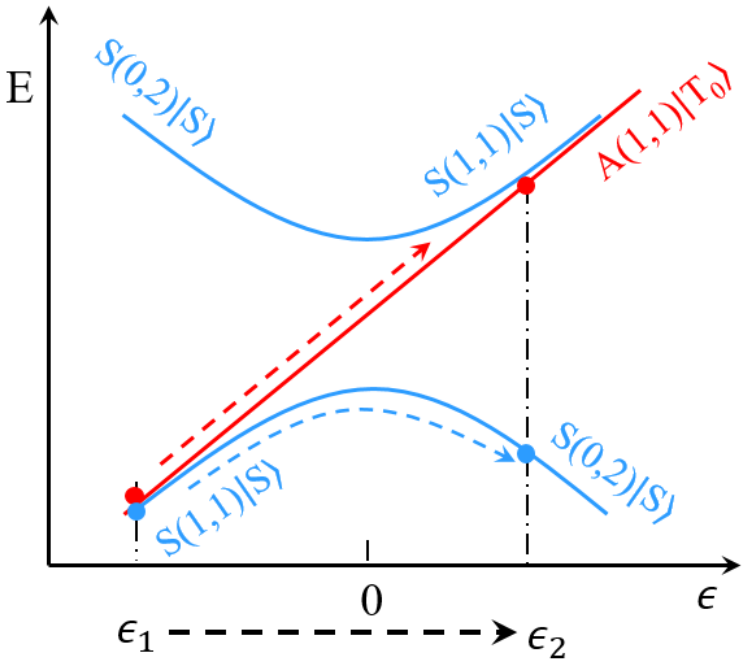

Figure 2.4: Schematic illustration of spin-to-charge conversion. When the detuning is adiabatically tuned from ϵ_1 to ϵ_2, the different spin states result in different charge configurations, which can be detected by a QPC or SET charge sensor.

This different spatial charge distribution can be detected by monitoring the current through the nearby QPC or SET, which is sensitive to the electrostatic potential created by the charge state.

Compared to charge sensors based on QPCs, SET charge sensors offer much higher sensitivities (about 30 times higher) and improved signal-to-noise ratios (about 3 times higher) [55]. However, SET charge sensors require more complex gate structures and a larger number of electrical connections to define and control the sensing area. Therefore, SETs are the preferred option for charge sensing when the experimental setup can accommodate the increased complexity of the gate design.

2.2 Coherent transfer protocol

In this section, we introduce a coherent information transfer protocol between a spin qubit defined by a GDQD and an incident photon. The content of this section is based on Ref. [35].

The main challenge for the coherent information transfer comes from the lack of hole confinement in a GDQD, since the applied gate voltage cannot trap an electron and a hole at the same time due to their opposite charges. As a result, the photo-excited electron and hole, whose spin states depend on the polarization of the incident photon and thus are entangled with each other, are separated, in which case the electron stays trapped but the hole is lost. This leads to an inevitable loss of coherence.

The solution, which is introduced in this section, is to use an optically active quantum dot (OAQD), realized either by an SAQD or a gate-defined exciton trap [52], as an intermediary between the GDQD and the photon to trap the photo-excited hole. By applying a transfer protocol, coherent quantum state transfer can be achieved. The transfer protocol consists of two steps:

1. Creation of a bound exciton in the OAQD by the absorption of the incident photon in the Voigt configuration.

2. Adiabatic transfer of the photo-excited electron into the GDQD with the photo-excited hole remaining trapped in the OAQD.

For a schematic illustration of the transfer protocol, the reader is referred to the original publication [35].

2.2.1 Creation of a bound exciton

After the absorption of an incident photon propagating perpendicular to the heterostructure (z-direction), the photo-generated electron and hole have opposite spin states: $|\downarrow\Uparrow\rangle_z$ or $|\uparrow\Downarrow\rangle_z$, or a superposition of both, depending on the polarization of the incident photon. Here, the single arrow denotes the electron spin, and the double arrow denotes the hole spin. These states are called *bright states* because they are optically active. In contrast, exciton states with parallel electron and hole spins ($|\uparrow\Uparrow\rangle_z$ and $|\downarrow\Downarrow\rangle_z$) are called *dark states*, as their total angular momentum does not match that of a photon.

In the basis $\{|\downarrow\Uparrow\rangle_z, |\uparrow\Downarrow\rangle_z, |\uparrow\Uparrow\rangle_z, |\downarrow\Downarrow\rangle_z\}$, the Hamiltonian describing the electron-hole exchange interaction, while ignoring the fine-structure splitting [57] between the bright states and between the dark states, can be written

as

$$\mathbf{H}_{0,z} = \frac{1}{2}\begin{pmatrix} \Delta_0 & 0 & 0 & 0 \\ 0 & \Delta_0 & 0 & 0 \\ 0 & 0 & -\Delta_0 & 0 \\ 0 & 0 & 0 & -\Delta_0 \end{pmatrix}, \tag{2.5}$$

where Δ_0 is the energy splitting between the dark and bright states due to the electron-hole exchange interaction.

Applying a strong in-plane magnetic field along the x-direction and expressing $\mathbf{H}_{0,z}$ in the new spin quantization axis yields

$$\mathbf{H}_{0,x} = \frac{1}{2}\begin{pmatrix} 0 & -\Delta_0 & 0 & 0 \\ -\Delta_0 & 0 & 0 & 0 \\ 0 & 0 & 0 & -\Delta_0 \\ 0 & 0 & -\Delta_0 & 0 \end{pmatrix}, \tag{2.6}$$

in the basis $\{|\downarrow\Uparrow\rangle_x, |\uparrow\Downarrow\rangle_x, |\uparrow\Uparrow\rangle_x, |\downarrow\Downarrow\rangle_x\}$. In addition to $\mathbf{H}_{0,x}$, the Zeeman splitting caused by the in-plane magnetic field is described by

$$\mathbf{H}_{\mathrm{Ze},x} = \frac{\mu_B B}{2}\begin{pmatrix} -g_e - g_h & 0 & 0 & 0 \\ 0 & g_e + g_h & 0 & 0 \\ 0 & 0 & g_e - g_h & 0 \\ 0 & 0 & 0 & -g_e + g_h \end{pmatrix}, \tag{2.7}$$

where g_e and g_h are the electron and hole g-factors, respectively. The complete Hamiltonian for the system is therefore $\mathbf{H}_{\mathrm{Ze},x} + \mathbf{H}_{0,x}$.

If the magnetic field is sufficiently strong such that the Zeeman splitting dominates over Δ_0, the $\mathbf{H}_{0,x}$ term can be neglected, and the eigenstates of the system closely match the basis states $\{|\downarrow\Uparrow\rangle_x, |\uparrow\Downarrow\rangle_x, |\uparrow\Uparrow\rangle_x, |\downarrow\Downarrow\rangle_x\}$. In this limit, all four basis states are optically active, as each has a finite overlap with one of the bright states $|\downarrow\Uparrow\rangle_z$ or $|\uparrow\Downarrow\rangle_z$. Specifically, $\{|\uparrow\Uparrow\rangle_x, |\downarrow\Downarrow\rangle_x\}$ can be excited with horizontally polarized photons, whereas $\{|\downarrow\Uparrow\rangle_x, |\uparrow\Downarrow\rangle_x\}$ require vertical polarization. Here, "horizontal (H)" and "vertical (V)" are defined relative to the orientation of the in-plane magnetic field: for a magnetic field along x, H corresponds to x-polarization, and V to y-polarization.

By matching the photon energy to the desired eigenstates (e.g., using

frequency conversion) and selecting the appropriate polarization, two of the four eigenstates can be chosen as the computational basis. A favorable choice is $\{|\uparrow\Uparrow\rangle_x, |\downarrow\Uparrow\rangle_x\}$, or equivalently $\{|\uparrow\Downarrow\rangle_x, |\downarrow\Downarrow\rangle_x\}$. The advantage of this choice is that the hole spin remains the same in both states, so the quantum information is entirely stored in the electron spin. This allows for efficient transfer of the electron's spin state to a nearby spin qubit in the GDQD, while the hole remains confined in the OAQD until it is used for spin-to-photon conversion during readout.

2.2.2 Adiabatic electron transfer

After the creation of a bound exciton, the photo-generated electron is tunnel-coupled to the GDQD by adiabatically increasing the detuning between the electron energy levels of the OAQD and the GDQD. This process can be summarized as

$$\begin{aligned} |\omega_1, \mathrm{H}\rangle &\xrightarrow{\text{P.E.}} |\circ\uparrow\Uparrow\rangle_x \xrightarrow{\text{A.T.}} |\uparrow\circ\Uparrow\rangle_x, \\ |\omega_2, \mathrm{V}\rangle &\xrightarrow{\text{P.E.}} |\circ\downarrow\Uparrow\rangle_x \xrightarrow{\text{A.T.}} |\downarrow\circ\Uparrow\rangle_x, \end{aligned} \tag{2.8}$$

where "P.E." stands for photo-excitation and "A.T." denotes adiabatic transfer. Here, ω_1 and ω_2 are the frequencies of the incident photons matching the energies of the exciton eigenstates $\{|\uparrow\Uparrow\rangle_x, |\downarrow\Uparrow\rangle_x\}$. The symbol $\circ$ indicates an empty quantum dot. For example, $|\circ\uparrow\Uparrow\rangle_x$ represents an empty GDQD and a spin-up electron-hole pair in the OAQD, while $|\uparrow\circ\Uparrow\rangle_x$ indicates that the electron is transferred to the GDQD, leaving a hole in the OAQD. By utilizing this transfer process, the quantum information encoded in the polarization and frequency of the incident photon is coherently transferred to the single-spin state of an electron trapped in a GDQD. This transfer process can be done with a fidelity of 96% [35].

To transfer the information to an ST_0 qubit, the protocol becomes more complex. Assuming that an electron with spin-up is already located in the left dot of the GDQD, the transfer steps are

$$\begin{aligned} |\uparrow\circ\rangle|\omega_1, \mathrm{V}\rangle &\xrightarrow{\text{P.E.}} |\uparrow\circ\rangle|\downarrow\Uparrow\rangle_x \xrightarrow{\text{A.T.}} |T_0\rangle|\circ\Uparrow\rangle_x, \\ |\uparrow\circ\rangle|\omega_2, \mathrm{V}\rangle &\xrightarrow{\text{P.E.}} |\uparrow\circ\rangle|\uparrow\Downarrow\rangle_x \xrightarrow{\text{Rabi+A.T.}} |S\rangle|\circ\Uparrow\rangle_x. \end{aligned} \tag{2.9}$$

The fidelity of this transfer process is 84% for ST_0 qubits. Here, a Rabi pulse is required to drive the transition to the singlet spin state in the second transition path. Notably, in this case, the quantum information of the incident photon is entirely encoded in its frequency, while the polarization remains **vertical** for both transitions. This characteristic plays a critical role in the design and modeling of the optical interface, as discussed in Chapters 3 and 4.

2.3 Photonic crystals

In solid-state physics, the electronic band structure arises from the interaction between electrons and the periodic atomic crystal lattice of the material. When the electron's de Broglie wavelength becomes comparable to the lattice constant, energy bandgaps appear, as observed in semiconductor materials, where certain electron energy ranges are forbidden.

By analogy, in the photonic domain, similar phenomena occur when the refractive index of a material is periodically modulated with a period comparable to the wavelength of light. This periodicity gives rise to the photonic band structure and the associated photonic bandgaps [58, 59, 60]. Such structures are referred to as photonic crystals (PhCs).

PhCs can be classified according to their dimensionality:

- **1D PhCs**: Periodic dielectric modulation in one dimension, with continuous translational symmetry in the other two, e.g., Bragg mirrors.
- **1D periodic dielectric waveguides**: Waveguides with a refractive index modulation along the propagation direction, e.g., fiber Bragg gratings, waveguide grating couplers.
- **2D PhCs**: Periodic dielectric structures in two dimensions, with continuous translational symmetry in the third.
- **2D planar PhCs**: A slab waveguide structure patterned with a 2D periodic lattice, enabling in-plane photonic bandgaps and vertical confinement via total internal reflection.

- **3D PhCs**: Full three-dimensional periodicity in the refractive index. The fabrication of a full 3D PhC is extremely challenging.

In this thesis, we only use structures based on 2D planar PhCs. To keep the content of this section concise, we only discuss 2D planar PhCs and the corresponding nanophotonic structures, such as photonic crystal cavities (PCCs) and photonic crystal waveguides (PhC waveguides).

2.3.1 Photonic band structure

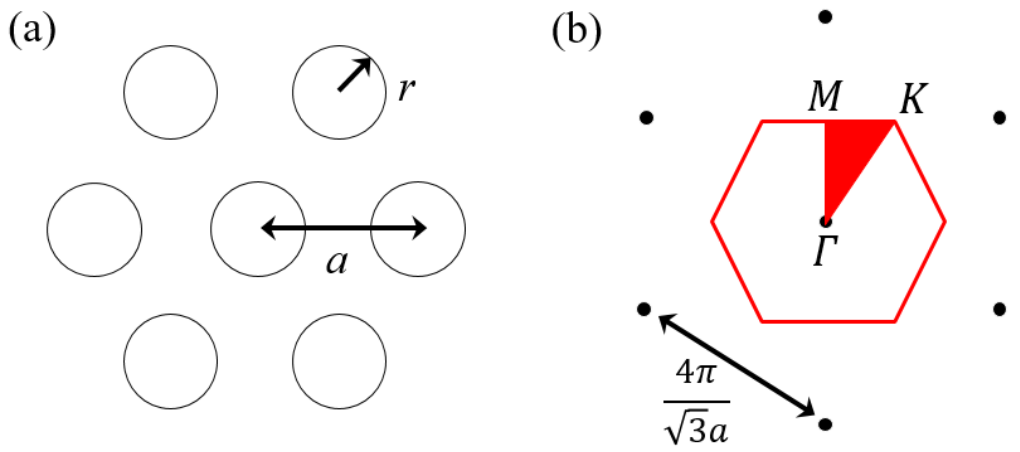

Figure 2.5: (a) A triangular lattice of circles with a lattice constant a and a hole radius r. (b) The reciprocal lattice with a lattice constant $4\pi/\sqrt{3}a$ obtained by a spatial 2D Fourier transformation. The red hexagon represents the boundary of the first Brillouin zone, and the red shaded triangle indicates the irreducible Brillouin zone. Γ, M, and K are three high-symmetry points.

Figures 2.5(a) and 2.6(a) show two types of the most frequently used lattices for 2D planar PhC: the triangular PhC and the square PhC. For 2D planar PhCs, the most important parameters are the lattice constant a, the radius r of the circles, the refractive index of the substrate material, and the slab thickness t. The circles can represent either air holes etched into a dielectric slab or dielectric rods with a height t standing in free space.

By applying a 2D spatial Fourier transformation to the lattice, we obtain the reciprocal lattice, shown in Figures 2.5(b) and 2.6(b) for the triangular and square PhC, respectively. In reciprocal space, we highlight in the figures the first Brillouin zone and the irreducible Brillouin zone, whose vertices

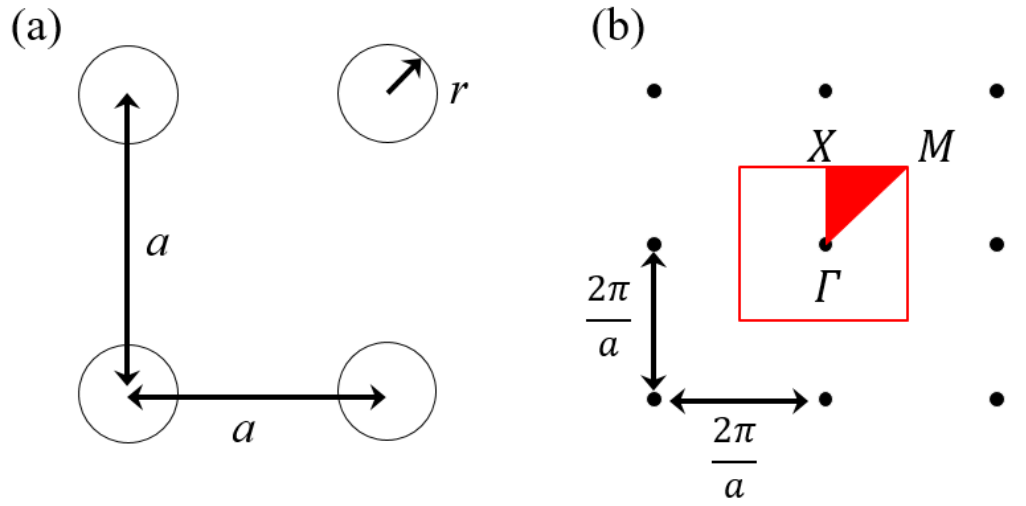

Figure 2.6: (a) A square lattice of circles with a lattice constant a and a hole radius r. (b) The reciprocal lattice with a lattice constant $2\pi/a$. The first Brillouin zone is highlighted by the red square, and the irreducible Brillouin zone by the red shaded area. High-symmetry points are Γ, X, and M on the vertices of the irreducible Brillouin zone.

correspond to the high-symmetry points. Analogous to the case of electronic band structures, the photonic band structure is calculated along the edges of the irreducible Brillouin zone, starting and ending at the Γ point after a closed path. For example, the band structure for the triangular lattice is typically plotted along the Γ–M–K–Γ path. For the square lattice, it follows the Γ–X–M–Γ path.

Figure 2.7 shows an example of a photonic band structure calculated for a triangular lattice etched into a GaAs/AlGaAs slab. Depending on the symmetry of the electromagnetic field, we distinguish between two different cases: transverse electric (TE) and transverse magnetic (TM). In the TE/TM case, the dominant electric/magnetic field lies in the plane of the photonic crystal lattice, respectively. For a PhC slab suspended in free space, the TE modes and the TM modes are orthogonal to each other due to the vertical mirror symmetry with respect to the mid-plane of the slab. However, if a substrate is used on one side of the PhC slab for mechanical support, this mirror symmetry is broken and the TE/TM modes are not well defined anymore, which causes the TE/TM mixing. If the mixing is not significant, their field patterns still closely resemble that of the unmixed

TE/TM profile.

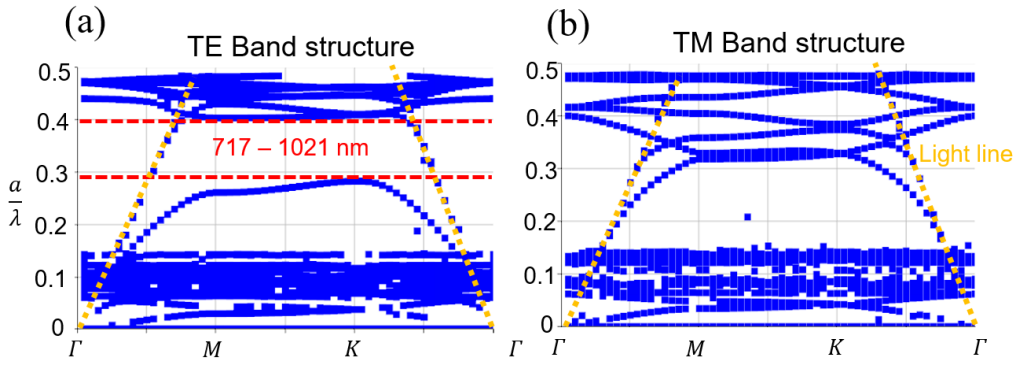

Figure 2.7: Example of a photonic band structure of a triangular lattice with a lattice constant $a = 290$ nm and a hole radius $r = 109$ nm. The lattice is etched into a GaAs/AlGaAs slab with a thickness of $t = 220$ nm. (a) The TE band structure with a TE bandgap opening from 717 to 1021 nm. (b) The TM band structure, in which a TM bandgap is absent.

In Figure 2.7, we see that a bandgap opens for the TE band structure, but such a bandgap is missing for the TM band structure. This is often the case for 2D planar PhCs formed by etching air holes into a dielectric slab. On the contrary, if the PhCs are defined by dielectric rods standing in free space, a TM bandgap is usually present while a TE bandgap is missing [60]. PhCs featuring a complete bandgap, i.e., overlapping TE and TM bandgaps for certain frequencies, are also possible by carefully choosing the parameters. For example, if we increase the hole radius of an etched PhC slab to a significantly large value (close to half of the lattice constant), the PhC formed in this manner can either be considered as a dielectric slab with large air holes or an array of free-standing triangular-shaped rods, which are the unetched regions in the center of three adjacent holes.

The triangular lattice is usually preferred for designing PhC-based devices, as it features a larger bandgap compared to the square lattice. This can be intuitively understood by considering the C_6 symmetry of the triangular lattice and the C_4 symmetry of the square lattice. For C_6 symmetry, the lattice reproduces itself under a rotation of $\pi/3$, while for C_4 symmetry, we need a larger rotation angle of $\pi/2$. This suggests that the triangular lattice is more "isotropic" compared to the square lattice, as the former is less dependent on spatial orientation. In this case, the conditions for a total

Bragg reflection are more likely to be satisfied for all spatial orientations at the same time for the triangular lattice, resulting in a broader photonic bandgap.

Figure 2.8(a) and (b) show the width of the bandgap as a function of r/a for the 2D planar triangular and square lattices, respectively. The lattice is formed by etching air holes into a GaAs slab. As we can see, the width of the bandgap is significantly larger for the triangular lattice than for the square lattice. Moreover, we observe a complete photonic bandgap, i.e., the overlap region between the TE and TM bandgap for a large radius, especially for the triangular lattice. The reason has already been discussed above.

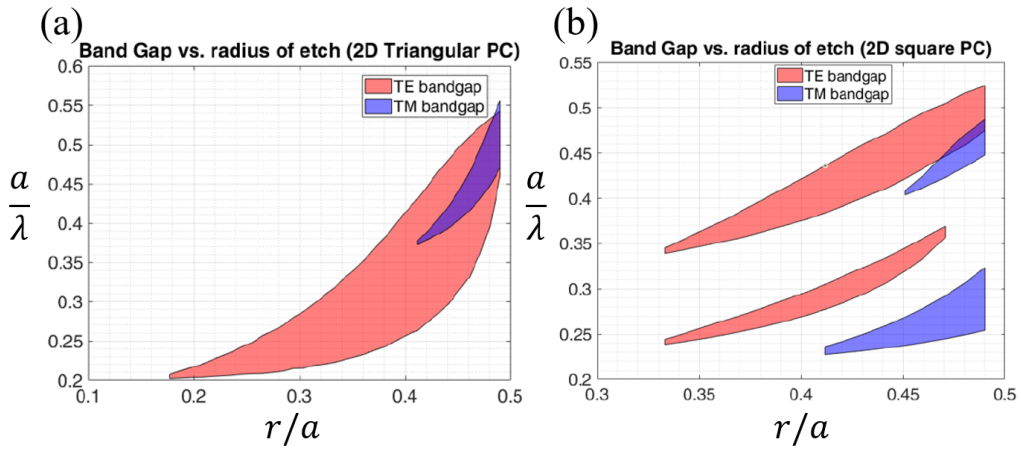

Figure 2.8: The width of the TE (red shaded area) bandgap and the TM (blue shaded area) bandgap as a function of r/a for (a) triangular lattice and (b) square lattice. The lattice is formed by etching air holes into a GaAs slab.

2.3.2 Photonic crystal cavities

PhC cavities are formed by introducing local defects into the PhC. Localized cavity modes appear at certain frequencies inside the optical bandgap. Here, we will focus on the TE bandgap and TE optical modes without specifically mentioning "TE" for compactness. In 2D planar PhC cavities, the photonic bandgap offers in-plane optical confinement, while the light is trapped by total internal reflection in the vertical direction.

The local defects can be implemented by modifying the radii, shifting the

positions, or completely removing some of the air holes from the dielectric slab. Depending on the geometries of the modified region, different names are assigned to the cavities. Figure 2.9 shows three examples of triangular PhC cavities: H1, H2, and H3, which are formed by removing holes in a hexagonal area with side lengths of a, $2a$, and $3a$, respectively. Another frequently studied cavity type is the L-type cavity created by removing a series of holes in a single row like the L1 or L3 cavities.

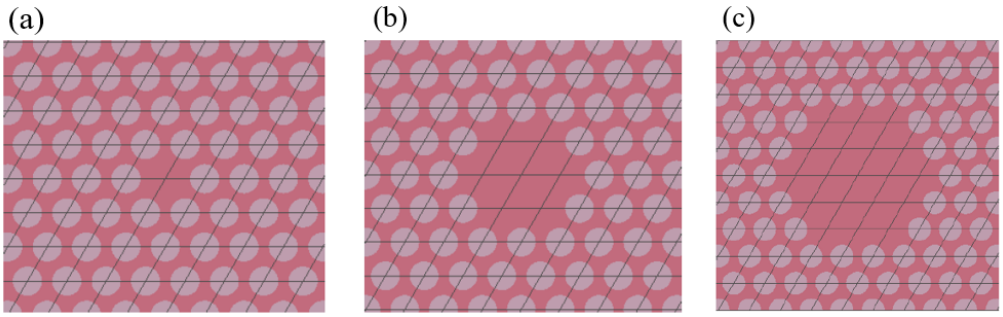

Figure 2.9: Examples of triangular PhC cavities. (a) H1 cavity, (b) H2 cavity, (c) H3 cavity. The black lines are plotted for visual clarity

Two key parameters for the PhC cavity are the quality factor (Q factor) and the modal volume V_m [24, 25]. The Q factor is defined as the ratio between the energy stored in the cavity and the energy loss per oscillation cycle. It can be expressed as

$$Q = 2\pi \frac{E_{\text{cavity}}}{P_{\text{out}}/f_0} = \omega_0 \frac{E_{\text{cavity}}}{P_{\text{out}}}, \tag{2.10}$$

where E_{cavity} is the energy stored in the cavity, P_{out} is the total power dissipated from the cavity, ω_0 is the angular frequency of the cavity mode of interest. If multiple power dissipation channels exist, the total Q factor can be expressed as a combination of partial quality factors corresponding to different channels. The mathematical expression is

$$\frac{1}{Q_{\text{total}}} = \frac{P_{\text{out}}}{\omega_0 E_{\text{cavity}}} = \frac{1}{\omega_0 E_{\text{cavity}}} \sum_i P_i = \sum_i \frac{1}{Q_i}, \tag{2.11}$$

where i denotes different loss channels.

For PhC cavities, extremely large Q factors are achieved by employing a

technique called "gentle confinement", which is realized by fine-tuning the positions and radii of carefully selected air holes close to the boundary of the PhC [61, 62]. As a result, radiation loss can be efficiently suppressed and the Q factor can be significantly improved.

The modal volume of a cavity mode is defined as [25]

$$V_m = \frac{\int_V \varepsilon(\vec{r})|\vec{E}(\vec{r})|^2 d^3\vec{r}}{\max[\varepsilon(\vec{r})|\vec{E}(\vec{r})|^2]}, \tag{2.12}$$

where $\varepsilon(\vec{r})$ is the relative permittivity of the dielectric material, and $\vec{E}(\vec{r})$ is the electric field profile of the mode. The modal volume describes the effective spatial extent of the PhC cavity mode, as seen by the electromagnetic fields.

The cavity Q factor and the modal volume V_m together determine the Purcell factor:[24]

$$F_P = \frac{3}{4\pi^2}\left(\frac{\lambda_0}{n}\right)^3 \frac{Q}{V_m}, \tag{2.13}$$

where λ_0 is the free-space wavelength of the investigated cavity mode, and n is the effective refractive index of the dielectric material at the location of the quantum emitter. The Purcell factor quantifies the enhancement or inhibition of the spontaneous emission rate of the quantum emitters inside the cavity when the coupling between the emitter and the cavity is not too strong (the weak-coupling regime).

2.4 Gaussian beams

2.4.1 Paraxial approximation

The most commonly used formula for approximating a free space Gaussian beam is

$$\vec{\boldsymbol{E}}_g(r,z) = E_0\,\vec{\mathbf{x}}\,\frac{w_0}{w(z)}\,\exp\left(-\frac{r^2}{w(z)^2}\right)\exp\left(i\left(k_0 z + k_0\frac{r^2}{2R(z)} - \psi(z)\right)\right), \tag{2.14}$$

where

z : the propagation direction,

$k_0 = 2\pi/\lambda$: the wave number in free space,

$r = \sqrt{x^2 + y^2}$: the radial distance from the center axis of the beam,
w_0 : the waist radius of the beam ($1/e^2$ intensity radius),
$w(z) = w_0\sqrt{1 + (z/z_R)^2}$: the beam radius as a function of z,
$z_R = \pi w_0^2/\lambda$: the Rayleigh length,
$R(z) = z(1 + (z_R/z)^2)$: the radius of curvature,
$\psi(z) = \arctan(z/z_R)$: the Gouy phase,
$\theta = \lambda/\pi w_0$: the divergence angle.

We assume that the Gaussian beam is polarized along the x-direction and propagating in the positive z-direction in equation 2.14. This equation is based on the paraxial approximation, where we assume a large beam waist radius $w_0 \gg \lambda$, or equivalently, a small divergence angle θ. It is worth noting that the Gaussian beam is uniquely defined by a single parameter: the waist radius w_0, or the divergence angle θ.

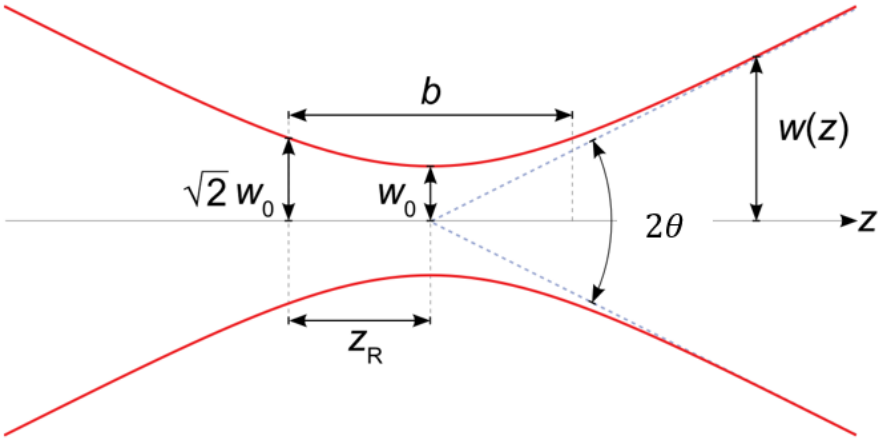

Figure 2.10: Cross-section of a Gaussian beam. The shape of a Gaussian beam is uniquely defined by a single parameter: the waist radius w_0, or the divergence angle θ.

For further discussion, it is necessary to show how the equation 2.14 is derived based on the angular spectrum method [63]. We start by constructing the Gaussian beam by superposing a series of plane waves propagating at slightly different directions:

$$\vec{\boldsymbol{E}}_g(\vec{\boldsymbol{r}}, t) = \vec{\mathbf{x}} \iint A(k_x, k_y) \exp(i(k_x x + k_y y + k_z z - \omega t))\, \mathrm{d}k_x\, \mathrm{d}k_y, \quad (2.15)$$

where

$$A = A(k_x, k_y) = A_0 \exp\left(-\frac{{k_x}^2 + {k_y}^2}{4/w_0^2}\right) \tag{2.16}$$

is the amplitude of a plane wave with a wave vector $\vec{\boldsymbol{k}}_0 = k_x\vec{\mathbf{x}} + k_y\vec{\mathbf{y}} + k_z\vec{\mathbf{z}}$. The paraxial approximation assumes that $w_0 \gg \lambda$, which is equivalent to $4/w_0^2 < 4\pi^2/w_0^2 \ll 4\pi^2/\lambda^2 = k_0^2$. In this case, $A(k_x, k_y)$ has a non-vanishing value only for $k_x^2 + k_y^2 \ll k_0^2$. Therefore, we can write

$$k_z = \sqrt{k_0^2 - k_x^2 - k_y^2} = k_0\sqrt{1 - \frac{k_x^2 + k_y^2}{k_0^2}} \approx k_0 - \frac{k_x^2 + k_y^2}{2k_0}. \tag{2.17}$$

Now, equation 2.15 can be written as

$$\begin{aligned}\vec{\boldsymbol{E}}_g(\vec{\boldsymbol{r}}, t) &= \vec{\mathbf{x}} \iint A(k_x, k_y) \exp\left(i(k_x x + k_y y + k_0 z - \frac{k_x^2 + k_y^2}{2k_0} z - \omega t)\right) \mathrm{d}k_x \mathrm{d}k_y \\ &= \vec{\mathbf{x}} \exp(ik_0 z - i\omega t) E_g(\vec{\boldsymbol{r}}),\end{aligned} \tag{2.18}$$

with $E_g(\vec{\boldsymbol{r}})$ equal to the amplitude of the Gaussian beam:

$$E_g(\vec{\boldsymbol{r}}) = \iint A(k_x, k_y) \exp\left(i(k_x x + k_y y - \frac{k_x^2 + k_y^2}{2k_0} z)\right) \mathrm{d}k_x \mathrm{d}k_y. \tag{2.19}$$

This integral (equation 2.19) can be evaluated to obtain

$$\begin{aligned}E_g(\vec{\boldsymbol{r}}) &= \frac{4\pi A_0}{w_0^2\sqrt{1 + (z/z_R)^2}} \exp\left(\frac{ik_0(x^2 + y^2)}{2(z - iz_R)} - i\psi(z)\right) \\ &= \frac{4\pi A_0}{w_0^2} \frac{w_0}{w(z)} \exp\left(-\frac{x^2 + y^2}{w(z)^2}\right) \exp\left(ik_0 \frac{r^2}{2R(z)} - i\psi(z)\right),\end{aligned} \tag{2.20}$$

which is the amplitude of $\vec{\boldsymbol{E}}_g(r, z)$ defined in equation 2.14, with $E_0 = 4\pi A_0/w_0^2$.

2.4.2 Analytical model

The Gaussian beam calculated by the paraxial approximation (equation 2.14) assumes x-polarized E-field (and thus y-polarized H-field) with zero E-field

strength in the y- and z-polarization. This cannot be true for a real Gaussian beam because of the non-zero k_x and k_y in-plane wave vectors; otherwise, the plane waves constituting the Gaussian beam are not transverse anymore. For a small diverging angle θ, this non-physical paraxial approximation yields, in general, satisfying results because orthogonally polarized field components are vanishingly small.

However, for a large θ, the paraxial approximation breaks down, and we need a more rigorous model to calculate the Gaussian beam.

Levy and Silberberg [64, 65] proposed a set of analytical expressions for a linearly polarized (x-polarization) Gaussian beam:

$$\begin{aligned}
E_x &= E_0 G e^{ik_0 z}\left[1-\theta_d^2\frac{\mu}{2}+\theta_d^4 k_0^2\mu^2\left(\frac{x^2}{2^3}+\frac{r^2}{2^4}\right)\right],\\
E_y &= E_0 G e^{ik_0 z}\theta_d^4 k_0^2\mu^2\frac{xy}{4},\\
E_z &= E_0 G e^{ik_0 z} i\theta_d^2\frac{k_0\mu x}{2}\left(-1+\theta_d^2\frac{\mu}{2}-\theta_d^4 k_0^2\mu^2\frac{r^2}{2^4}\right),\\
H_x &= \frac{E_0}{Z_0} G e^{ik_0 z}\theta_d^4 k_0^2\mu^2\frac{xy}{4},\\
H_y &= \frac{E_0}{Z_0} G e^{ik_0 z}\left[1-\theta_d^2\frac{\mu}{2}+\theta_d^4 k_0^2\mu^2\left(\frac{y^2}{2^3}+\frac{r^2}{2^4}\right)\right],\\
H_z &= \frac{E_0}{Z_0} G e^{ik_0 z} i\theta_d^2\frac{k_0\mu y}{2}\left(-1+\theta_d^2\frac{\mu}{2}-\theta_d^4 k_0^2\mu^2\frac{r^2}{2^4}\right),
\end{aligned} \tag{2.21}$$

where

$\theta_d = \tan(\theta)$: with θ the divergence angle,
$w_0 = 2/(k_0\theta_d)$: the beam waist radius,
$z_R = 2/(k_0\theta_d^2)$: the Rayleigh length,
$k_0 = 2\pi/\lambda$: the wave number,
$r = \sqrt{x^2+y^2+z^2}$: the distance to the center of the beam waist,
$Z_0 = 376.73\,\Omega$: the free space impedance,
$\mu = 1/(1+iz/z_R)$: the axial propagation function,
$G = A_0\,\mu\,\exp(-\mu k_0^2\theta_d^2(x^2+y^2)/4)$: the Gaussian beam function.

According to Levy and Silberberg, this analytical model has a reasonable

accuracy up to a divergence angle as large as 0.8 rad (37.1°). For even larger divergence angles up to 80°, this model diverges because of the θ_d^4 terms. One naive approach is neglecting the terms containing θ_d^4 for large divergence angles. As we will see in chapter 4, we need to sweep the divergence angle of a Gaussian beam from 0° to 80°, where equations 2.21 diverge. As a result, we need a more rigorous model for generating a Gaussian beam.

2.4.3 Numerical model

According to equation 2.15, which is mathematically well defined for all θ, we are able to numerically construct, or approximate, a Gaussian beam. First we assign an E- and H-field for each $A(k_x, k_y)$ satisfying $|\vec{\boldsymbol{E}}(k_x, k_y)| = Z_0\, A(k_x, k_y)$ and $|\vec{\boldsymbol{H}}| = A(k_x, k_y)$. Second, we apply three-dimensional rotations to those fields to ensure that the E- and H-fields are perpendicular to the wave vector $\vec{\boldsymbol{k}}_0 = k_x\vec{\mathbf{x}} + k_y\vec{\mathbf{y}} + k_z\vec{\mathbf{z}}$. The orientations of $\vec{\boldsymbol{E}}(k_x, k_y)$ and $\vec{\boldsymbol{H}}(k_x, k_y)$ are determined in such a way that the desired final polarization is achieved after the rotations.

In order to construct a Gaussian beam polarized in the x-direction (a similar approach applies for the y-polarization), we first define the following initial field in the momentum space

$$\begin{aligned} \vec{\boldsymbol{E}}(k_x, k_y) &= E_{k_x}\vec{\mathbf{x}} + E_{k_y}\vec{\mathbf{y}} + E_{k_z}\vec{\mathbf{z}}, \\ \vec{\boldsymbol{H}}(k_x, k_y) &= H_{k_x}\vec{\mathbf{x}} + H_{k_y}\vec{\mathbf{y}} + H_{k_z}\vec{\mathbf{z}}, \end{aligned} \tag{2.22}$$

where

$$\begin{aligned} E_{k_x} = A\, Z_0 \cos(\alpha),\ E_{k_y} = -A\, Z_0 \sin(\alpha),\ E_{k_z} = 0, \\ H_{k_x} = A \sin(\alpha),\ H_{k_y} = A \cos(\alpha),\ H_{k_z} = 0, \end{aligned} \tag{2.23}$$

with $\alpha = \arctan(k_y/k_x)$. In case we need a y-polarized Gaussian beam, what we need to do is switch the expressions between E and H in 2.23 and apply an additional minus sign to the H components because the final H-field points in the negative x-direction. In order to obtain the right orientation of the E- and H-fields in the k-space, we apply two consecutive rotations.

The first rotation is about the y-axis by an angle $\phi = \arcsin\left(\sqrt{k_x^2 + k_y^2}/k_0\right)$. As a result, we obtain

$$\begin{aligned} E'_{k_x} &= E_{k_z}\sin(\phi) + E_{k_x}\cos(\phi), \\ E'_{k_y} &= E_{k_y}, \\ E'_{k_z} &= E_{k_z}\cos(\phi) - E_{k_x}\sin(\phi), \end{aligned} \tag{2.24}$$

and

$$\begin{aligned} H'_{k_x} &= H_{k_z}\sin(\phi) + H_{k_x}\cos(\phi), \\ H'_{k_y} &= H_{k_y}, \\ H'_{k_z} &= H_{k_z}\cos(\phi) - H_{k_x}\sin(\phi). \end{aligned} \tag{2.25}$$

The second rotation is about the z-axis by an angle α, after which we get

$$\begin{aligned} E''_{k_x} &= E'_{k_x}\cos(\alpha) - E'_{k_y}\sin(\alpha), \\ E''_{k_y} &= E'_{k_x}\sin(\alpha) + E'_{k_y}\cos(\alpha), \\ E''_{k_z} &= E'_{k_z}, \end{aligned} \tag{2.26}$$

and

$$\begin{aligned} H''_{k_x} &= H'_{k_x}\cos(\alpha) - H'_{k_y}\sin(\alpha), \\ H''_{k_y} &= H'_{k_x}\sin(\alpha) + H'_{k_y}\cos(\alpha), \\ H''_{k_z} &= H'_{k_z}. \end{aligned} \tag{2.27}$$

Finally, we apply beam propagation along the z-direction and transform the field to real space by a 2D inverse Fourier transformation (iFFT2):

$$\begin{aligned} \vec{\boldsymbol{E}}(x,y,z) &= \text{iFFT2}\left(\exp(ik_z z)\left(E''_{k_x}\,\vec{\mathbf{x}} + E''_{k_y}\,\vec{\mathbf{y}} + E''_{k_z}\,\vec{\mathbf{z}}\right)\right) \\ \vec{\boldsymbol{H}}(x,y,z) &= \text{iFFT2}\left(\exp(ik_z z)\left(H''_{k_x}\,\vec{\mathbf{x}} + H''_{k_y}\,\vec{\mathbf{y}} + H''_{k_z}\,\vec{\mathbf{z}}\right)\right) \end{aligned} \tag{2.28}$$

Figure 2.11 shows the real part of the six field components of a Gaussian beam with a divergence angle of $\theta = 10°$ and a wavelength of $\lambda = 823$ nm. They are calculated based on equation 2.22 to 2.28 at a distance of $z =$ -3.3 μm relative to the center of the beam waist, assuming the beam waist

center is located at $x = y = z = 0$ and the beam is propagating in the positive z-direction.

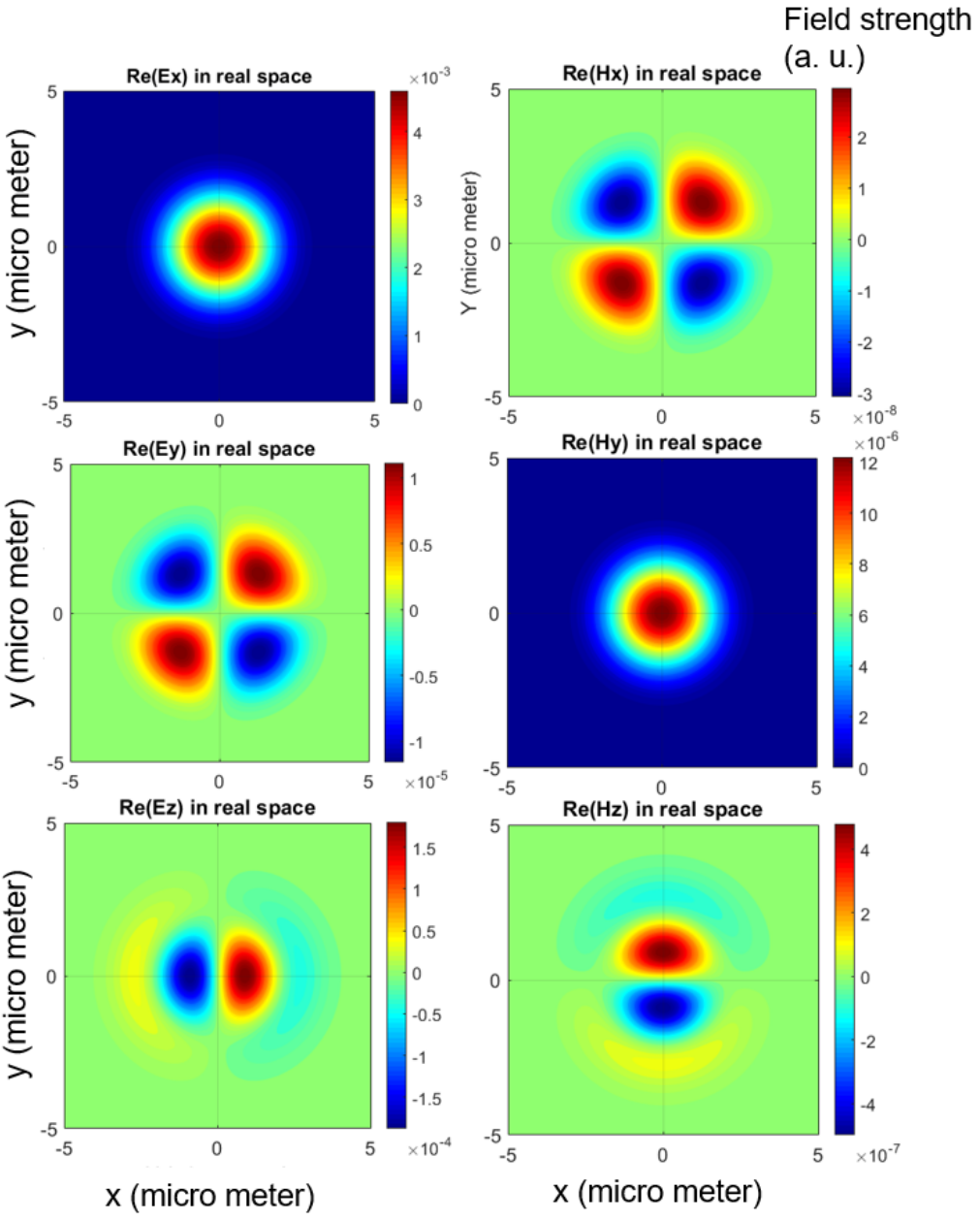

Figure 2.11: Field profile of a Gaussian beam generated by the numerical method. The divergence angle of the beam is $\theta = 10°$. The fields are sampled at a distance of -3.3 μm relative to the beam waist center.

Chapter 3

Optical Interface Assisted by a PCC

This chapter introduces the design and geometry of the optical interface, including the gate system, the photonic crystal cavity (PCC), and the cavity openings. The content of this chapter is based on an already published paper [41], whose first author is the author of this thesis.

3.1 GDQD and OAQD structure

The detailed geometry of the gate-defined double quantum dot (GDQD), optically active quantum dot (OAQD), and a quantum dot charge sensor (also known as a single-electron transistor (SET)) is depicted in Figure 3.1.

The electrodes defining these structures are deposited on a 220 nm $Al_{0.33}Ga_{0.67}As$ heterostructure membrane (Figure 3.1(a)), which consists of a 20 nm GaAs quantum well layer sandwiched by two 90 nm $Al_{0.33}Ga_{0.67}As$ layers providing the necessary potential barrier for the quantum well, and two additional 10 nm GaAs cap layers on the top and bottom sides to prevent oxidation of the Al in the barrier layer.

The electrodes are made of Au/Ti wires with a thickness of 9 nm (2 nm Ti and 7 nm Au). The wires of both the GDQD and sensor have a width of 30 nm. The OAQD consists of round guard gates (outer diameter of 400 nm) and a central trap gate (central diameter of 116 nm), as shown in Figure 3.1(b).

Electrical voltages are applied to the gates to create local potential minima in the 2DEG in the 20 nm GaAs quantum well, which confine the singlet-triplet spin qubit in the GDQD and the exciton under the trap gate of the OAQD. The wires defining the GDQD and the sensor are only patterned on the top side of the membrane following a validated geometry, while those defining the OAQD are deposited symmetrically on both sides of the membrane to ensure a strongly localized electric field and independent tuning of the exciton trap via the quantum confined Stark effect (QCSE) [52].

In this thesis, we assume that the OAQD is working at a **target wavelength** of 823 nm, which is the result of electrically tuning the bandgap wavelength of GaAs under 4 K.

The protocol for coherent information transfer between a photonic qubit and the ST_0 qubit is already discussed in section 2.2. This protocol was estimated to be compatible with a fidelity of 84% for a singlet-triplet spin qubit [35], assuming that the capture of the incident photon is successful and a bound exciton is created in the OAQD. In the remaining part of this thesis, we focus on increasing the conversion efficiency between the photon and the bound exciton. The details regarding the physical realization of the information transfer between the ST_0 qubit and the bound exciton are outside the scope of this thesis.

In the original protocol, an InAs self-assembled quantum dot (SAQD) plays the role of the OAQD. To fully exploit fabrication scalability, a gate-defined exciton trap is used in our design instead. As a result, the entire gate system can be fully lithographically defined at any location of the heterostructure membrane, without the need to search for a suitable SAQD candidate, around which the gate system is aligned and defined. Moreover, the electrically controllable exciton energy and tunnel coupling strength between the OAQD and the GDQD provide us with more flexibility to operate the device with optimal transfer fidelity. On the other hand, however, the additional metal gate required for the OAQD introduces extra optical absorption. The overall photon extraction efficiency is reduced by 30% relative to what would otherwise be achievable with the remaining electrode system.

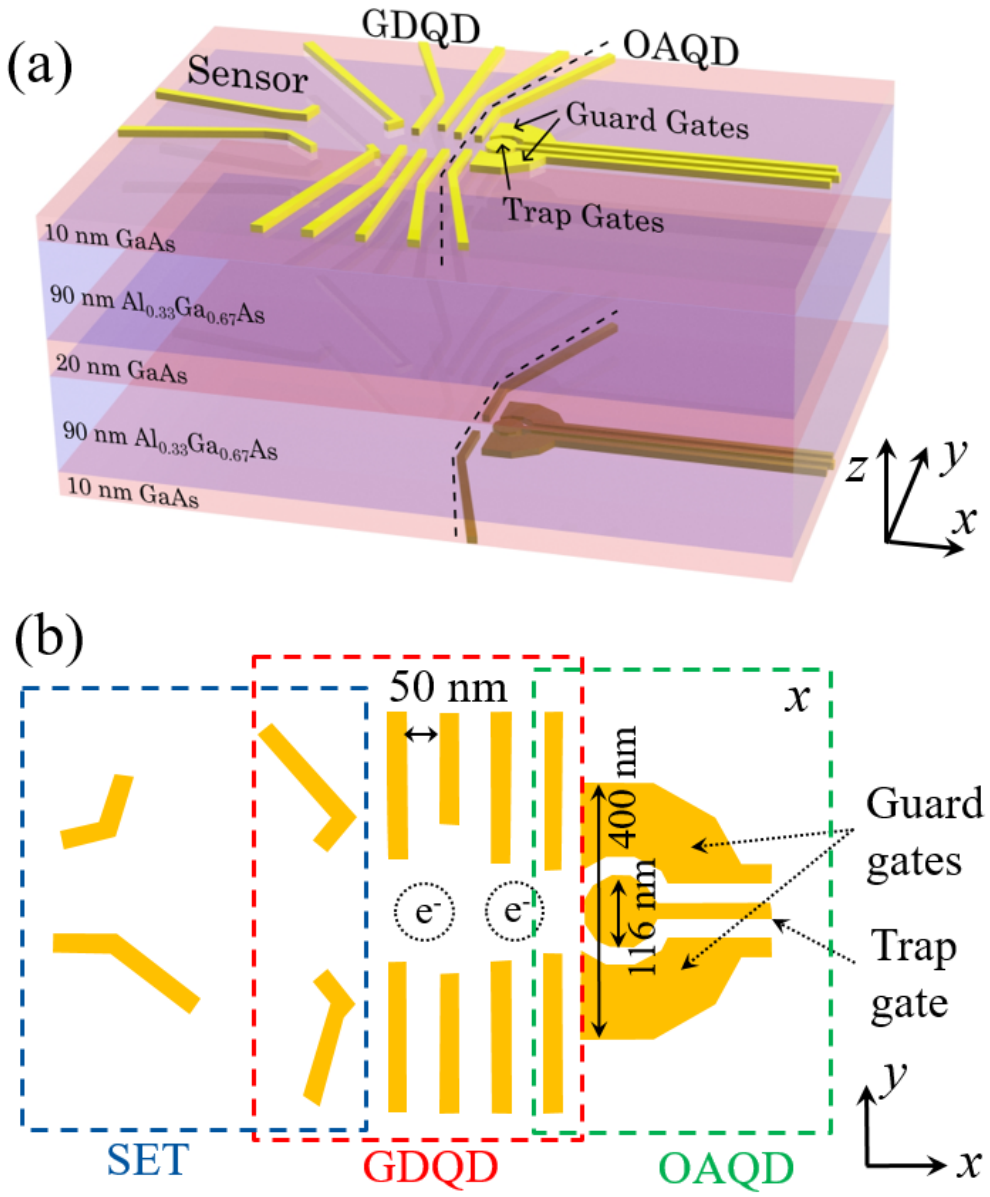

Figure 3.1: (a) Schematic view of the GDQD, the OAQD, and the quantum dot charge sensor defined on the 220 nm $Al_{0.33}Ga_{0.67}As$ heterostructure membrane. The electrodes defining the OAQD are deposited on both sides of the membrane to ensure a strongly localized electric field. On the other hand, the GDQD and the quantum dot charge sensor only require top side electrodes. (b) Detailed dimensions of the gate system. SET stands for single electron transistor, which is equivalent to a quantum dot charge sensor.

Since the OAQD is located in the center of the GaAs layer, only around 2% of the emitted photons from the OAQD are able to escape the membrane due to the high refractive index contrast between the semiconductor material and the free space in the absence of in-plane optical confinement. In this chapter, a comprehensive design of a photonic crystal cavity is introduced, which confines light inside the cavity and couples it to a free space Gaussian beam, which can be easily coupled into a single mode fiber. With an additional back reflector located below the membrane to recycle photons emitted downwards, the collection efficiency is further increased.

Moreover, four cavity openings are integrated into the cavity to enable electrical transport in the quantum well layer, which is required for the functionality of the single electron transistor and the GDQD. The underlying reason is that the surface charges on the sidewalls of the etched holes deplete the 2DEG in its vicinity, and thus block any current from transporting through the photonic crystal without any opening. On the other hand, optical confinement is not influenced thanks to the carefully engineered mini-stopband of those cavity openings.

3.2 Optical interface overview

A complete overview of the gate system and the PCC is depicted in Figure 3.2. The gate system (Figure 3.1) is placed in the center of the cavity with the trap gate of the OAQD in alignment with the cavity center. The triangular lattice of holes is etched through the heterostructure membrane. Four cavity openings are integrated in the four diagonal directions, in which electrical current is supported and thus charge sensing is possible using the quantum dot charge sensor. The Ti/Au wires required to access the gate system need to be routed through the photonic crystal with an alignment accuracy of < 15 nm between the photonic crystal and the metallic wires in an electron beam lithography process, considering the width of the wires and the distance between adjacent holes. As will be demonstrated in chapter 5, the desired alignment accuracy can be achieved.

A 200 nm thick gold reflector (not shown in Figure 3.2) is positioned 305 nm below the GaAs quantum well layer to recycle photons emitted down-

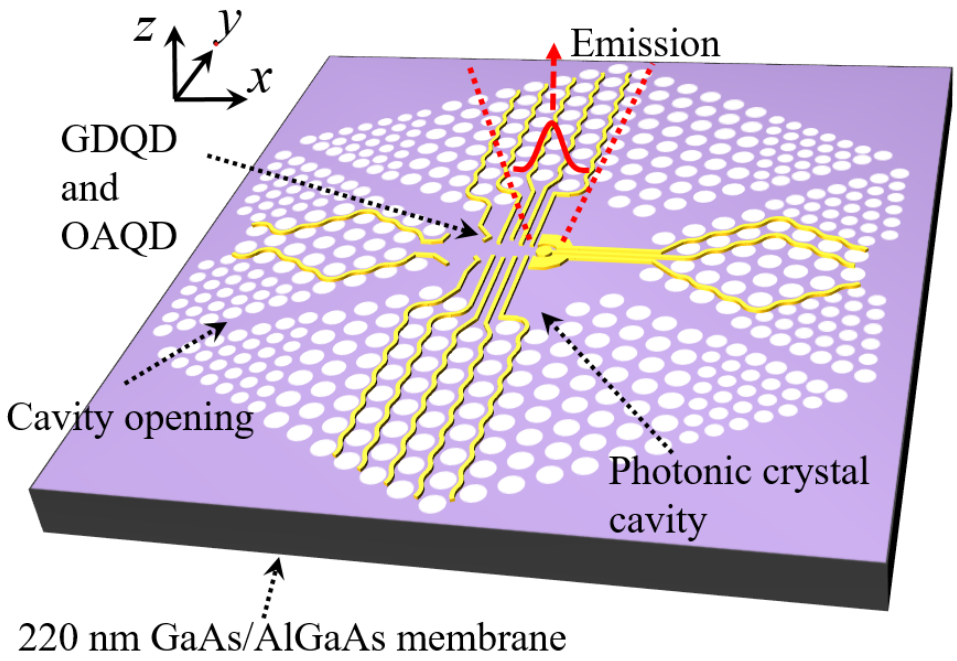

Figure 3.2: Schematic overview of the optical interface including the PCC, the electrode system, and the cavity openings forming unwanted photonic crystal waveguides in which light propagation is blocked by a mini-stopband. A 200 nm thick gold reflector (not shown) is attached to the membrane via an SiO_2 interlayer, whose thickness is optimized to coherently recycle photons emitted downwards.

wards. The space between the gold reflector and the GaAs/$Al_{0.33}Ga_{0.67}As$ membrane is filled with an SiO_2 interlayer. The reflector position is optimized to maximize the extraction efficiency and ensure a high optical overlap of the far-field emission pattern with an ideal Gaussian beam propagating perpendicularly to the membrane in the positive z-direction. In addition to enhancing the center lobe of the far-field emission of the PCC, the reflector also suppresses side lobes, increasing the purity of the emitted Gaussian beam [41, 42].

The hole radii, the lattice pitches of the PCC, and the cavity opening are designed in such a way that the wavelength of the cavity mode with a concentrated Gaussian far-field profile overlaps with the target wavelength of 823 nm. In the following sections, the detailed designs of the PCC, the cavity opening, and the back reflector will be introduced.

3.2.1 Photonic crystal cavity

The PCC is designed by modifying a hexagonal H4 cavity shown in Figure 3.3, where holes are removed from the center of a complete hexagonal shaped lattice to form a hexagon with a side length of 4 times the lattice constant. The lattice constant is $a_1 = 290$ nm, and the hole radius is $r_1 = 109$ nm. The detailed TE (transverse electric) and TM (transverse magnetic) band structures for this planar photonic crystal are calculated using the Lumerical FDTD package, assuming an infinite lattice of holes is etched on a free-standing GaAs/$Al_{0.33}Ga_{0.67}As$ membrane described in Figure 3.1. The detailed TE and TM band structures are plotted in Figure 3.4. As we can see, a TE bandgap opens from 717 nm to 1021 nm, while such a bandgap is absent in the TM band structure.

Since the optical emission of the OAQD is primarily the result of the recombination between an electron and a heavy hole, the polarization of the emitted photon is primarily parallel to the membrane (in-plane). Moreover, the Purcell effect for the TE polarization further enhances this recombination process and thus the in-plane emission. In contrast, such an enhancement does not exist for the TM polarization due to the absence of an optical TM bandgap.

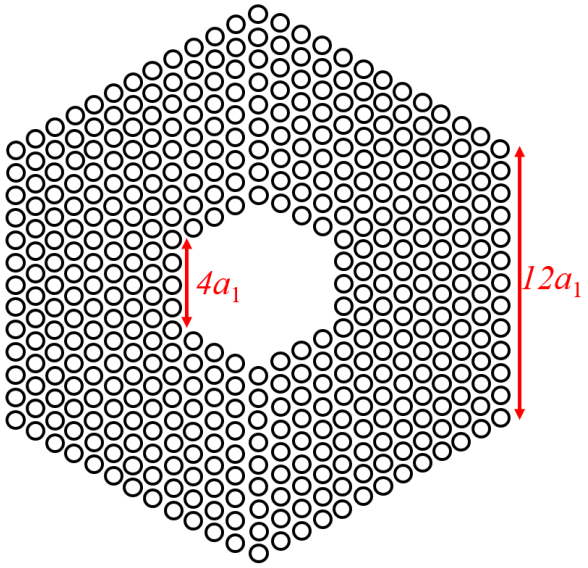

Figure 3.3: Schematic view of a complete triangular H4 cavity. The lattice constant is $a_1 = 290$ nm, and the hole radius is $r_1 = 109$ nm.

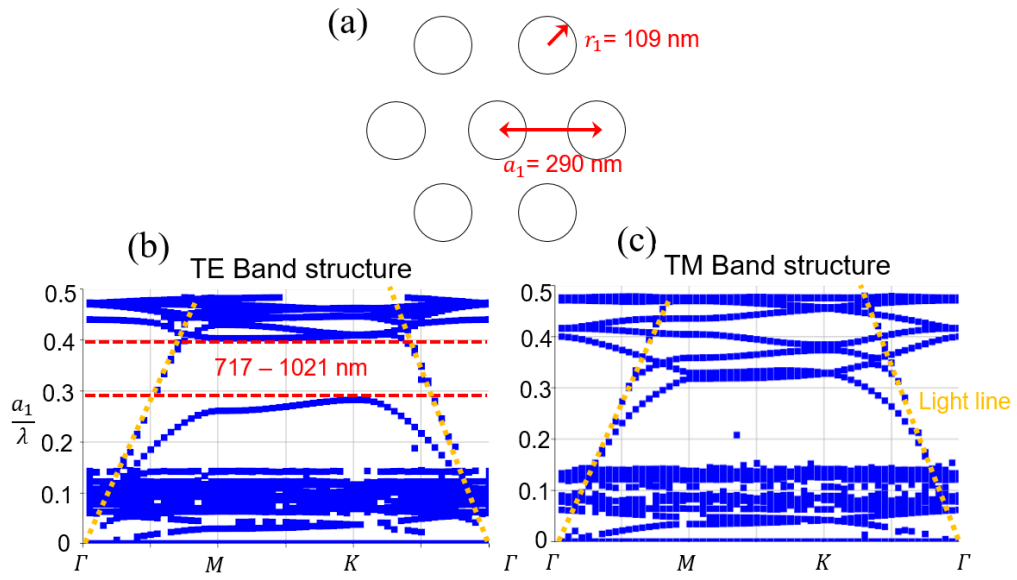

Figure 3.4: (a) Triangular photonic crystal with a lattice constant a_1 and hole radius r_1, (b) TE band structure, assuming an infinite lattice is etched on a free standing GaAs/$Al_{0.33}Ga_{0.67}As$ membrane described in Figure 3.1. A TE bandgap opens from 717 nm to 1021 nm as indicated by the red dashed lines, (c) TM band structure for the same lattice. The orange dashed lines represent the light lines, below which the light is confined to the membrane due to total internal reflection.

3.2.2 Cavity openings

In order to realize the four cavity openings, as required by the quantum dot charge sensor, we modify the complete H4 cavity by removing holes to create the openings. As it is shown in Figure 3.5(a), four rows of holes in the four diagonal directions are removed (marked in red). In addition, we also remove 12 other holes (also marked in red) to simplify the routing of metal wires and to optimize the wire position to minimize their optical absorption.

The cavity openings formed by simply removing the holes support undesired photonic crystal waveguide modes, which destroy the optical confinement of the PCC. We calculate the TE band structure of this so-formed photonic crystal waveguide along the direction of the opening, as this is the only direction preserving the translational symmetry required for calculating any band structure. As we can see in Figure 3.6, multiple waveguide modes are clearly visible. Three modes are highlighted with different colors. Red stands for the even mode while green stands for the odd mode. The two highlighted odd modes anti-cross each other from $k = 0.3 \times 2\pi/a_1$ to $k = 0.4 \times 2\pi/a_1$ due to the same symmetry and result in a mini-stopband [66] from 1030 to 1058 nm with a spectral width of 28 nm. Inside this mini-stopband, no waveguide mode exists for all k-vectors.

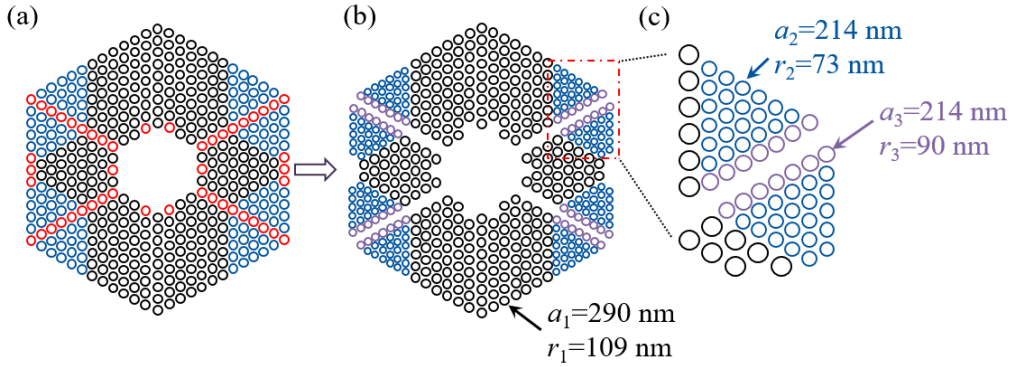

Figure 3.5: (a) The complete triangular H4 cavity. The holes marked by red circles are removed, while the holes shown in blue are downscaled to move the mini-stopbands to the target wavelength. (c) Final cavity structure after the modification. (d) Detailed view of the lattice around the openings. The holes immediately adjacent to the openings have an enlarged radius in order to achieve a wider mini-stopband

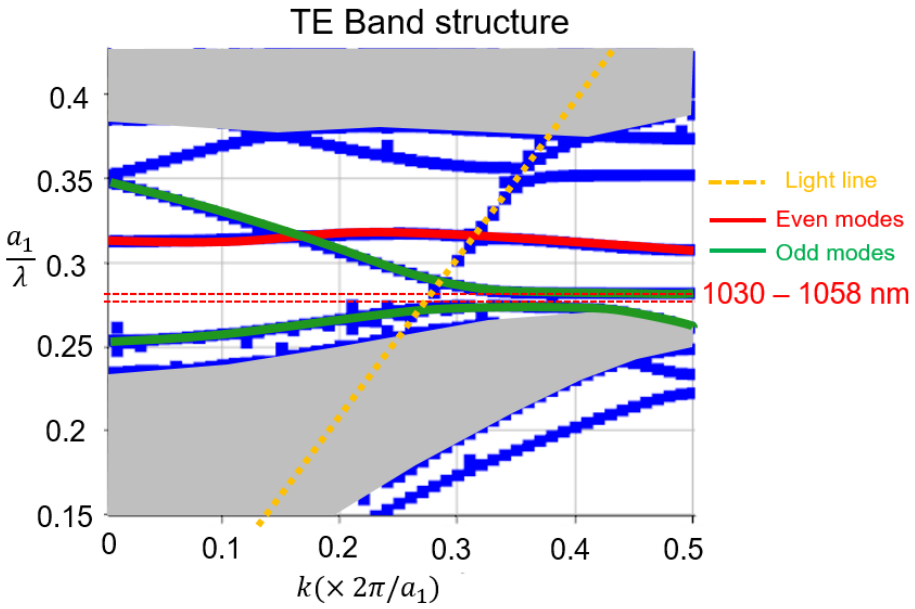

Figure 3.6: TE band structure of the so-formed photonic crystal waveguide (a_1 = 290 nm, r_1 = 109 nm) by removing the holes marked in red in Fig 3.5 (a). The shaded area represents the extended photonic crystal mode. A mini-stopband is visible from 1030 nm to 1058 nm.

The mini-stopband is utilized to achieve optical confinement at the target wavelength of 823 nm. In order to shift the mini-stopband to the desired wavelength, the holes marked in blue are downscaled to have a smaller lattice pitch and hole radius, as shown in Figure 3.5(b) and (c). The down-scaled lattice pitch is a_2 = 214 nm, and the down-scaled hole radius is r_2 = 73 nm. Figure 3.7 depicts the TE band structure of this down-scaled photonic crystal waveguide.

As we can see, after down-scaling the lattice constant from a_1 = 290 nm to a_2 = 214 nm and the hole radius from r_1 = 109 nm to r_2 = 73 nm, the mini-stopband has shifted to the wavelength range from 835 nm to 865 nm, with a spectral width of 30 nm. We notice that the spectral width has already increased from 28 nm to 30 nm after the down-scaling. A wider mini-stopband is favorable because the electromagnetic field decays faster along the waveguide and thus offers better optical confinement, assuming the target mode lies in the center of the mini-stopband. Moreover, a wider mini-stopband allows for more tolerance to fabrication imperfections, which

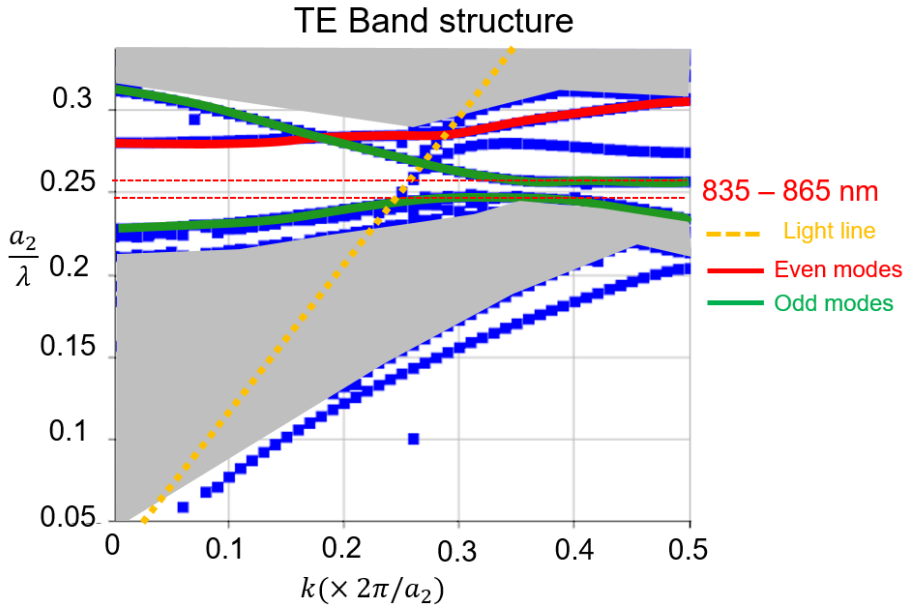

Figure 3.7: TE band structure of down-scaled lattice ($a_2 = 214$ nm, $r_2 = 73$ nm) without increasing the hole radius next to the opening. The mini-stopband is now from 835 nm to 865 nm

might cause undesired wavelength shifts.

In order to further increase the spectral width of the mini-stopband, we increase the hole radius closest to the openings from $r_2 = 73$ nm to $r_3 = 90$ nm, while keeping the lattice pitch unchanged ($a_3 = a_2 = 214$ nm). This modification is indicated in Figure 3.5(c), where the purple holes have a radius $r_3 = 90$ nm. Further increasing r_3 to a value greater than 90 nm would increase the spectral width of the mini-stopband even further. However, this would also further burden the fabrication process, as the holes would be closer to each other. As a trade-off, we choose $r_3 = 90$ nm as the final geometry.

Figure 3.8 shows the final TE band structure of the cavity openings after the down-scaling and the subsequent increase of the hole radius right next to the openings. As we can see, the mini-stopband is now in the wavelength range from 793 to 845 nm. The target wavelength lies in the center of the mini-stopband as a result of engineering. In the meantime, the spectral width of the mini-stopband is increased to 52 nm. In combination with the TE bandgap of the original photonic crystal (a_1 and r_1), which spans

from 717 to 1021 nm, in-plane optical confinement is achieved within the mini-stopband (793 nm to 845 nm).

The underlying reason for the increased spectral width of the mini-stopband can be understood in the following way. The mini-stopband is a result of the interaction/coupling between two waveguide modes with the same symmetry (here, two modes with the same odd symmetry), which is represented by the anti-crossing in Figure 3.6. After the down-scaling of the lattice pitch and the subsequent increase of the hole radius closest to the opening, the width of the opening, or the width of the photonic crystal waveguide, is decreased. As a result, the spatial confinement becomes stronger and the interacting waveguide modes have stronger field strengths due to the decreased cross-section area of the waveguide, over which they interact with each other. Thus, the interaction/coupling becomes stronger and results in a wider mini-stopband.

3.3 Conclusion

In this chapter, we introduced the detailed geometry of the GDQD, the OAQD, a quantum dot charge sensor, the GaAs/$Al_{0.33}Ga_{0.67}As$ membrane, and the PCC with cavity openings. The entire structure can be fully lithographically defined and deterministically fabricated, which greatly increases the scalability of on-chip integration. All the parameters presented in this chapter serve as a baseline for the following chapters of this thesis.

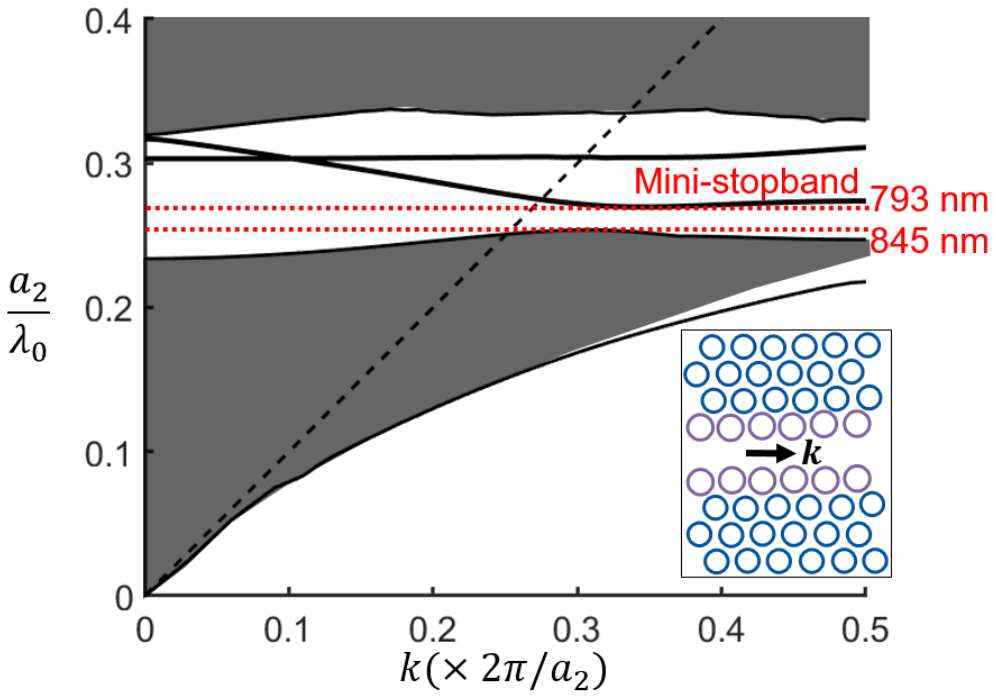

Figure 3.8: The calculated TE band structure of the cavity opening. Inset shows the direction, along which the k vector is varied from 0 to π/a_2. A mini-stopband opens from 793 nm to 845 nm. The shaded area represents the extended photonic crystal mode in the down-scaled crystal. The dashed black line represents the light line.

Chapter 4

Modeling Results

This chapter focuses on modeling the performance of the optical interface introduced in chapter 3. The content of this chapter is based on an already published paper [41], whose first author is the author of this thesis. Some of the data, figures, tables, and texts from the paper are transferred to this chapter.

4.1 FDTD environment

We perform three-dimensional finite-difference time-domain (3D FDTD) simulations to evaluate the performance of our optical interface. The complete structure (Fig 3.2) is modeled using a commercially available software package (Lumerical FDTD). The GaAs/$Al_{0.33}Ga_{0.67}As$ membrane, the metal gates, the photonic crystal cavity with cavity openings, the gold back reflector, and the SiO_2 interlayer can be clearly defined and constructed in the software according to the designed geometry.

Figure 4.1 depicts the xy-view and yz-view of the complete structure in Lumerical FDTD. Here, PML stands for perfectly matched layer, which absorbs all incident light. In order to avoid numerical instabilities, we use stabilized PML [67] in all six spatial directions.

The exciton under the trap gate of the OAQD is modeled by an in-plane y-dipole according to the dipole approximation [68] because the size of the quantum dot, in which the exciton is trapped, is much smaller than the target wavelength of 823 nm. In the xy-plane, the size of the quantum dot

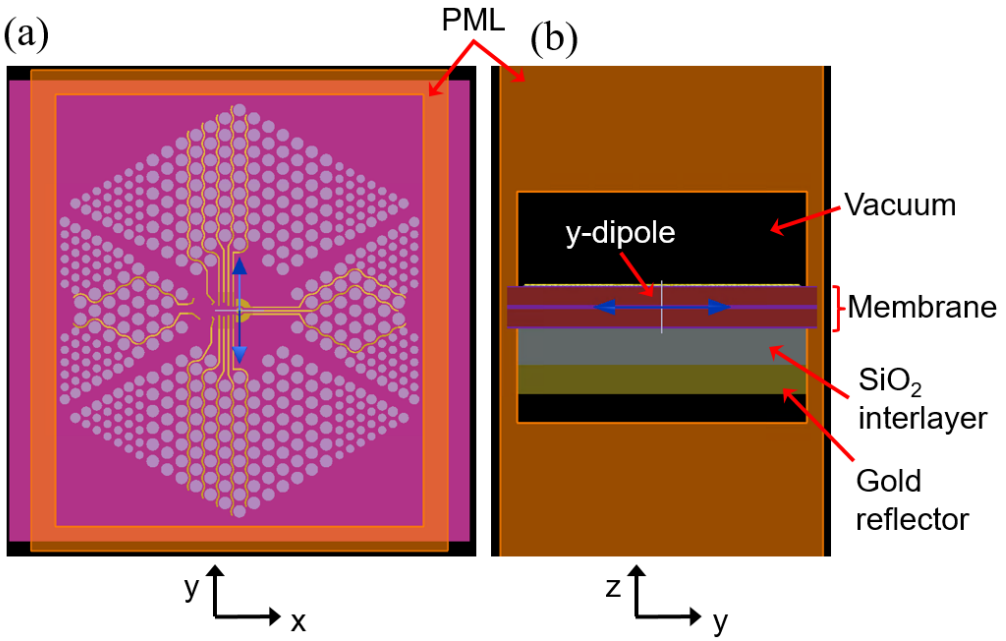

Figure 4.1: Simulation overview in Lumerical FDTD, where PML stands for perfectly matched layer. (a) xy-view, (b) yz-view.

is determined by the size of the trap gate (116 nm in diameter) and by the thickness of the GaAs quantum well (20 nm) in the z-direction. Those values are significantly smaller than the target wavelength, and the dipole approximation is thus justified.

In the meantime, we set the orientation of the dipole to be parallel to the membrane (in-plane). The underlying reason for the in-plane polarization is that the exciton hole is predominantly of heavy-hole type for the lowest energy valence sub-band. Although some level of heavy-hole to light-hole mixing can result in an off-plane polarization component, we do not expect it to play a significant role. Since the PCC only supports a TE bandgap, as we can see in Figure 3.4, the in-plane emission experiences Purcell enhancement at the wavelengths of existing TE cavity modes. In contrast, this is not the case for TM emission due to the absence of a TM bandgap. As a result, potential heavy-hole light-hole mixing is not expected to play a significant role here. Thus, the modeling of the exciton by an in-plane dipole is reasonable.

As discussed in the section 2.2, the transfer protocol between the singlet-

triplet qubit and the flying qubit (photon) requires a strong in-plane magnetic field in the Voigt configuration. This in-plane magnetic field splits the exciton energy for different in-plane polarizations. Only the polarization perpendicular to the direction of the external magnetic field plays a role in the transfer protocol. Without losing generality, we model the OAQD by an electric dipole oriented in the y-direction, assuming that the in-plane magnetic field is oriented along the x-direction.

Cryogenic temperature (4 K) is required for the functionality of the GDQD, the exciton trap, and the quantum dot charge sensor. We therefore assume that the temperature of the simulation environment is 4 K. However, the default material properties available in Lumerical FDTD are those measured under room temperature (RT, or 300 K). Since the refractive indices and the bandgap energies of GaAs and $Al_{0.33}Ga_{0.67}As$ are temperature dependent, it is necessary to adjust the material properties to account for the temperature change.

The bandgap energies of GaAs and $Al_{0.33}Ga_{0.67}As$ under 4 K are $E_{4K,\ GaAs}$ = 1.52 eV and $E_{4K,\ AlGaAs}$ = 1.90 eV [69], corresponding to optical transition wavelengths of 816 nm and 652 nm, respectively. Consequently, $Al_{0.33}Ga_{0.67}As$ is fully transparent at 823 nm, while GaAs exhibits weak absorption at this wavelength due to the Urbach tail [70] and exciton absorption near the band edge. However, as our 220 nm membrane structure has a small GaAs fraction (two 10 nm cap layers and one 20 nm quantum well layer), we model the GaAs layers as lossless for simplicity.

In order to estimate the refractive indices of GaAs and $Al_{0.33}Ga_{0.67}As$ under 4 K ($n_{4K,\ GaAs}$, and $n_{4K,\ AlGaAs}$), the RT values ($n_{300K,\ GaAs}$, and $n_{300K,\ AlGaAs}$) are linearly extrapolated by considering the temperature dependence. According to Talghader and Smith [71], in the wavelength range of 960 nm to 1030 nm and in the temperature range between 25 °C and 150 °C, the temperature dependence of the refractive indices of GaAs and AlAs is measured to be

$$\left(\frac{dn}{dT}\right)_{GaAs} = (2.67 \pm 0.07) \times 10^{-4}/°C, \tag{4.1}$$

$$\left(\frac{dn}{dT}\right)_{\text{AlAs}} = (1.43 \pm 0.07) \times 10^{-4}/^{\circ}\text{C}. \tag{4.2}$$

For $Al_{0.33}Ga_{0.67}As$, we estimate its temperature dependence by linearly combining equation 4.1 and 4.2 according to the stoichiometric fraction of Ga and Al:

$$\left(\frac{dn}{dT}\right)_{\text{AlGaAs}} = (2.26 \pm 0.07) \times 10^{-4}/^{\circ}\text{C}. \tag{4.3}$$

We estimate the refractive indices under 4 K according to

$$n_{\text{4K, GaAs}} = n_{\text{300K, GaAs}} - \Delta T \left(\frac{dn}{dT}\right)_{\text{GaAs}}, \tag{4.4}$$

$$n_{\text{4K, AlGaAs}} = n_{\text{300K, AlGaAs}} - \Delta T \left(\frac{dn}{dT}\right)_{\text{AlGaAs}}, \tag{4.5}$$

where $\Delta T = 296$ K is the temperature difference. At the target wavelength of 823 nm, we have $n_{\text{300K, GaAs}} = 3.67$ and $n_{\text{300K, GaAs}} = 3.44$. According to equation 4.4 and 4.5, we obtain $n_{\text{4K, GaAs}} = 3.59$ and $n_{\text{4K, GaAs}} = 3.38$. In case that we need to simulate the structure at a different wavelength than 823 nm, we apply the same method to the RT values to estimate the 4 K values at that specific wavelength.

The calculated refractive indices are not entirely accurate and therefore only rough estimations. One reason for the inaccuracy is that the temperature dependence of refractive indices is not linear, especially under low temperature [72]. Moreover, the temperature range and wavelength range in which the values in equation 4.1 and 4.2 are measured do not include 4 K or 823 nm. This inaccuracy in the assumed refractive indices will be addressed by future experimental iterations. For the SiO_2 interlayer, we used an index of $n_{SiO_2} = 1.45$ (SiO_2 (Glass) - Palik) from the default material database of Lumerical FDTD. For the gold back reflector, we use the Au (gold) - Johnson and Christy from the same database.

4.2 Figure of merit

In the following sections, we focus on evaluating the performance of the optical interface. As discussed in section 3.1, we only focus on evaluating the

coupling efficiency between the exciton, which is modeled by a y-dipole, and the incident photon, which is assumed to be transmitted by a single-mode fiber. We assume that the subsequent information transfer between the exciton and the ST-qubit is always successful.

In the original transfer protocol, the information is transferred from the incident photon to the bound exciton. However, due to reciprocity, the coupling efficiency between the exciton and the photon can also be evaluated in a reversed process, in which a photon is emitted by the exciton and coupled to a free space Gaussian mode (fundamental mode of a single mode fiber). This reversed scheme could be more straightforwardly simulated with the available numerical tools, but conclusions apply to both processes. We will thus focus on this reversed scheme.

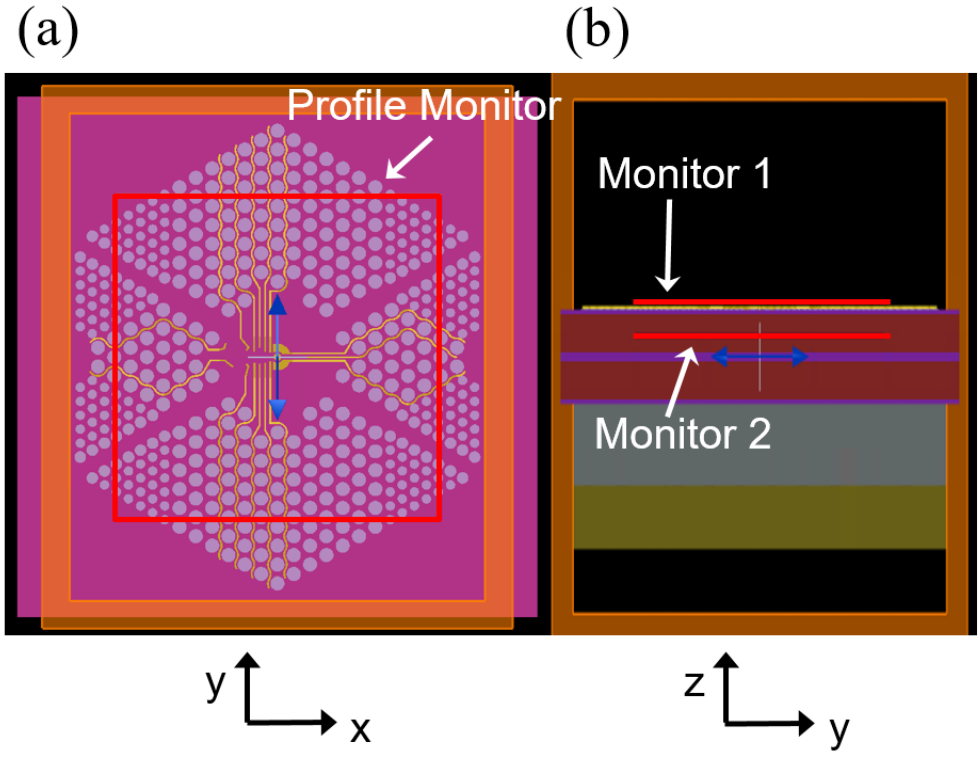

Figure 4.2: Simulation overview showing the position and dimension of the profile monitors. The two square monitors are placed in the xy-plane with their centers overlapping with the cavity center. The side length is 5 μm. Monitor 1 is placed 20 nm above the top surface of the membrane, and Monitor 2 is placed inside the membrane 50 nm above the dipole.

Figure 4.2 displays the location and dimension of the monitors (high-

lighted in red) used to record the electromagnetic field. Monitor 1 is located 20 nm above the top surface of the GaAs/$Al_{0.33}Ga_{0.67}As$ membrane to record the emitted near-field, while Monitor 2 is placed 50 nm above the dipole inside the membrane to record the cavity mode profile. Both monitors have a side length of 5 μm in the x- and y-direction. The size of the monitors is sufficiently large to record the entire electromagnetic field, since the cavity mode at the target wavelength decays rapidly (see section 4.3.1 for more detail) inside the photonic crystal and the waveguide opening thanks to the wide mini-stopband.

To calculate the probability of photons emitted by the OAQD to couple into a single mode fiber, we apply the following method. First, the electromagnetic field outside of the PCC is recorded by Monitor 1. The electromagnetic power P_r is calculated by integrating the normal component of the Poynting vector over the entire surface of Monitor 1:

$$P_r = \frac{1}{2}\int_{\text{Monitor 1}} \text{Re}(\vec{\boldsymbol{E}}_m \times \vec{\boldsymbol{H}}_m^*) \cdot d\vec{\boldsymbol{S}}, \tag{4.6}$$

where $\vec{\boldsymbol{E}}_m$ and $\vec{\boldsymbol{H}}_m$ denote the recorded electric and magnetic fields at a certain wavelength, and $\vec{\boldsymbol{S}}$ stands for the normal vector of the monitor surface. We define the **radiation efficiency**

$$\eta_r = \frac{P_r}{P_{\text{dipole}}} \tag{4.7}$$

as the fraction of dipole power P_{dipole} that is transmitted through the monitor surface P_r. This radiation efficiency η_r corresponds to the probability that the photons emitted by the OAQD escape the membrane via the top surface and propagate into free space.

Next, we calculate the **optical overlap** (OV) between the electromagnetic field recorded by the monitor and an ideal Gaussian beam using the formula [73]:

$$OV(\theta) = \frac{\left|\iint(\vec{\boldsymbol{E}}_m \times \vec{\boldsymbol{H}}_g^*(\theta) + \vec{\boldsymbol{E}}_g^*(\theta) \times \vec{\boldsymbol{H}}_m) \cdot d\vec{\boldsymbol{S}}\right|^2}{4\iint \text{Re}(\vec{\boldsymbol{E}}_m \times \vec{\boldsymbol{H}}_m^*) \cdot d\vec{\boldsymbol{S}} \iint \text{Re}(\vec{\boldsymbol{E}}_g(\theta) \times \vec{\boldsymbol{H}}_g^*(\theta)) \cdot d\vec{\boldsymbol{S}}}. \tag{4.8}$$

Here, $\vec{\boldsymbol{E}}_g(\theta)$ and $\vec{\boldsymbol{H}}_g(\theta)$ represent the electric and magnetic fields of a linearly polarized Gaussian beam with an $1/e^2$ intensity half angle θ. The Gaussian beam is numerically calculated according to equations 2.22 to 2.28. Alternatively, we can also analytically generate the Gaussian beam according to the equation 2.21. However, the θ^4 terms in this equation become divergent for large θ. Neglecting those θ^4 terms would give us a similar OV(θ) as the numerical approach. Considering that this analytical approach only has a reasonable accuracy up to a divergence angle of 37.1° according to the original paper [64, 65], we will only use the numerical method based on equations 2.22 to 2.28 in the following sections of this thesis.

For different θ values, the spatial position of the Gaussian beam is optimized separately to maximize the OV(θ). This optimization process is equivalent to optimizing the position of the single mode fiber to achieve maximum coupling. In the meantime, varying the divergence angle θ of the Gaussian beam can be realized by using different coupling lenses or collimators with different focal lengths. As a result, the maximum value $\mathrm{OV}_{\mathrm{max}}$ of OV(θ) is always realistic and achievable by selecting an appropriate lens system and by aligning the lens system to the optical interface.

Finally, we define the **overall efficiency** of our optical interface as:

$$\eta(\theta) = \eta_r \times OV(\theta) \tag{4.9}$$

which is equal to the probability that the emitted photons couple into a free space Gaussian beam with a divergence angle θ, which can be straightforwardly coupled to the fundamental mode of a single-mode fiber with the help of a lens system.

4.3 Modeling results

In this section, the core modeling results and the performance of the optical interface are presented. We first analyze the cavity spectrum of the PCC and the far-field emission patterns of the cavity modes. Then, we quantitatively evaluate and optimize the OVs and the overall efficiencies of the target

mode. Finally, we show that the performance can be further improved by undercutting the SiO_2 interlayer beneath the $GaAs/Al_{0.33}As_{0.67}As$ membrane. However, this improvement comes at the cost of increasing the complexity and difficulty of the fabrication process.

4.3.1 PCC spectrum

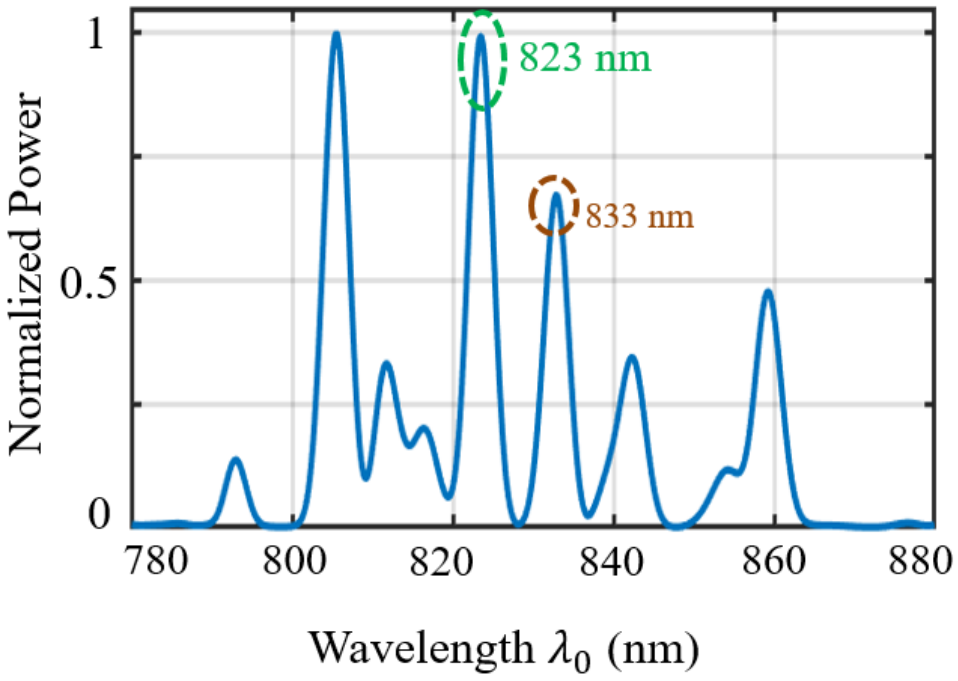

Figure 4.3: Normalized cavity power spectrum from 780 nm to 880 nm obtained from a cavity ring-down simulation. The target mode, which has a high extraction efficiency, is marked by a green dashed circle at 823 nm. As a comparison to the target mode, another cavity mode at 833 nm is also highlighted by a brown circle.

In order to obtain the cavity spectrum of the PCC, we excite the cavity by a broadband y-dipole source located at the position of the OAQD (the blue double arrow in Fig 4.1 and 4.2). The field ringing down inside the PCC is recorded as a function of time and Fourier transformed to obtain the cavity spectrum, which is presented in Figure 4.3. Due to the large size of the cavity, chosen to minimize electrostatic interaction between the quantum dots and surface charges at the etched holes, multiple resonant peaks are observed. We highlighted two cavity modes at 823 nm (the target mode)

and at 833 nm with a green and brown circle respectively. The parameters of the PCC, including the lattice constants and hole radii, are carefully engineered to ensure that the wavelength of this target mode coincides with the OAQD's working wavelength at 823 nm. As we will see later, this target mode features a concentrated Gaussian far-field pattern, with a high radiation and overall efficiency. The other mode at 833 nm is also highlighted for comparison.

The calculated Purcell factor for the target mode is $F = 2.18$. The relatively low Purcell enhancement is the result of the large cavity modal volume and the relatively low quality factor of the cavity mode, which is 232. Since we are focusing on enhancing the extraction efficiency of the photon and coupling it to a free space Gaussian mode, increasing the Purcell enhancement is not our primary goal. Moreover, the low quality factor and thus the large linewidth of the cavity mode would facilitate the transfer protocol between the Singlet-Triplet qubit and the photon, as the quantum information is encoded in the frequency/wavelength of the photon. A linewidth much larger than the frequency difference between the utilized frequency states would actually help to erase the which-path information and thus increase the tunability and fidelity of the information transfer process.

The real space field profiles of the two highlighted modes at 823 and 833 nm are depicted in Figure 4.4(a) and (b), respectively. The presented E-field intensity is recorded by the Monitor 2 (Figure 4.2) inside the membrane. We also plot the photonic crystal by dashed circles to show its relative position. It is evident that the optical confinement is well maintained, thanks to the presence of the mini-stopband. This feature is essential for guiding the emitted photons upwards. Since 823 nm and 833 nm are located inside the mini-stopband (793 nm to 845 nm), the electromagnetic fields decay exponentially for both modes as they propagate along the openings. Notice that the target mode decays faster inside the cavity opening than the other mode because the target mode lies deep in the center of the mini-stopband as a result of engineering, while the 833 nm mode is closer to the edge of the mini-stopband.

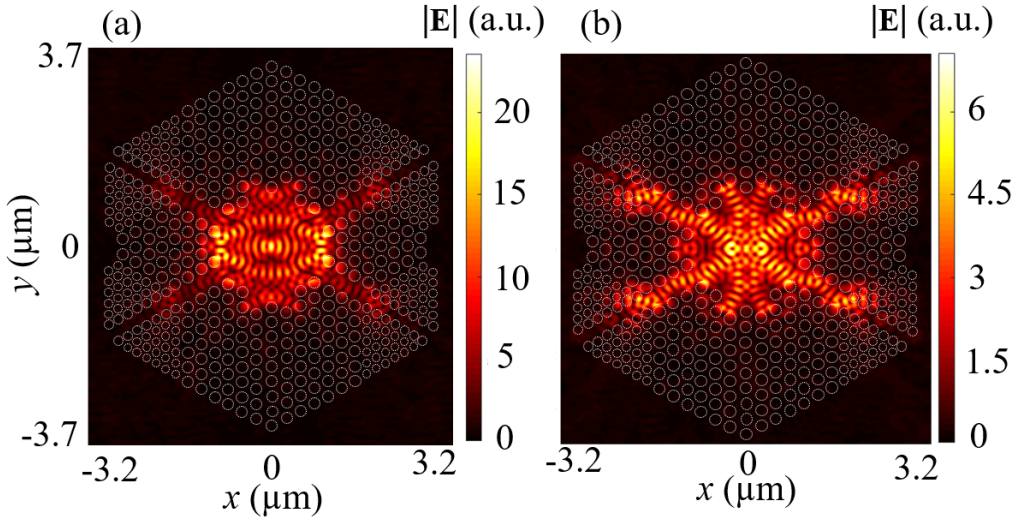

Figure 4.4: Real space cavity mode profile of the (a) 823 nm target mode and the (b) 833 nm mode excited by a y-dipole. An exponentially decaying electric field is observed along the cavity openings for both wavelengths as a consequence of the mini-stopband.

4.3.2 Far-field analysis

In order to obtain the far-field patterns for the different cavity modes, we first record the near-field by the Monitor 1 (Figure 4.2), which is located 20 nm above the top surface of the membrane. By decomposing the recorded near-field into a series of plane waves and applying a far-field transform (the 'farfieldexact3d' command in Lumerical FDTD), we are able to calculate the far-field patterns at arbitrary distances. The far-field patterns for both cavity modes at 823 nm and 833 nm are calculated on a plane parallel to the membrane surface. The plane has a size of 2 m by 2 m in the x- and y-directions and is located at a distance $z = 1$ m away from the OAQD ($x = 0$, $y = 0$, $z = 0$).

Figure 4.5 shows the calculated far-field electric field intensity. It is clear that pronounced vertical radiation is achieved for the target mode at 823 nm, as indicated by the intensity peak at $x = 0$ and $y = 0$. The 200 nm thick gold reflector is positioned 305 nm below the OAQD, which corresponds to a 195 nm thick SiO_2 interlayer. The reflector position is optimized to facilitate constructive interference and enhance the central emission peak, while simultaneously suppressing the side lobes. On the other hand, the

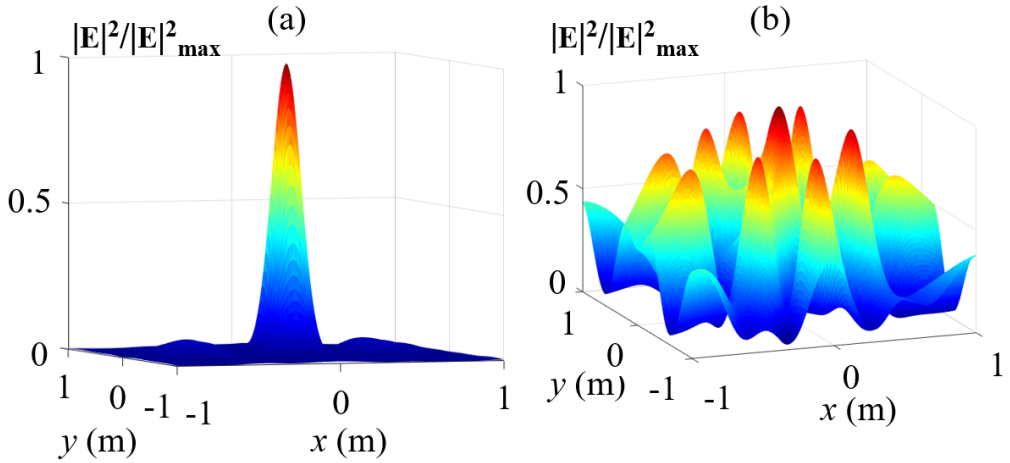

Figure 4.5: (a) Far-field pattern at 823 nm calculated on a plane parallel to the membrane surface and located at a distance $z = 1\ m$ away from the OAQD. Vertical emission with a pronounced Gaussian shape is observed. (b) Far-field pattern at 833 nm for comparison. The complex pattern is very different from a Gaussian beam profile. The far-field patterns are independently normalized in (a) and (b).

far-field pattern is complex for the 833 nm mode and shows a non-preferred emission direction for all reflector positions.

Figure 4.6(a) displays the far-field pattern of the target mode in the xy-view, where two lines (the red solid line and the green dashed line) are drawn through the intensity peak in the vertical and horizontal directions. The E-field intensity along those two lines is plotted in Figure 4.6(b). It is obvious that the central lobe at $x = y = 0$ has the shape of a Gaussian beam along both the vertical and horizontal directions. The $1/e^2$ intensity radius of the central lobe is 0.163 m and 0.177 m in the horizontal and vertical directions, respectively. This suggests that the shape of the central lobe is slightly elliptic, with a relative asymmetry of $0.014/0.177 = 7.9\%$. One possible reason for this asymmetry might be the cavity openings, as they break the C_6 symmetry of the hexagonal H4 cavity and reduce it to two slightly different reflection symmetries in the x- and y-directions.

Besides the central lobe, side lobes are also visible as shown in Figure 4.6(b). The relative peak intensities for the side lobes are 5.5% and 1.9% in the horizontal and vertical directions, respectively. The intensities of the side lobes are strongly influenced by the position of the bottom reflector,

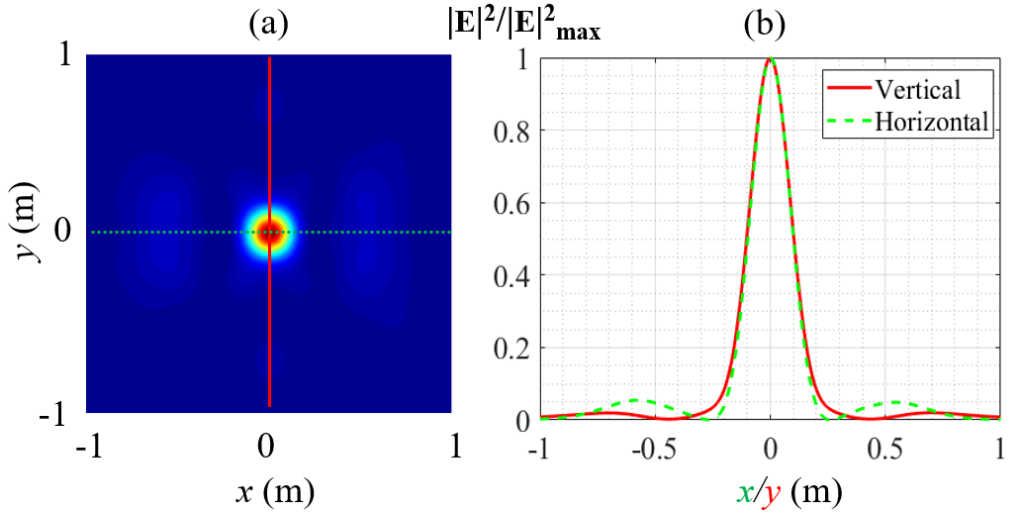

Figure 4.6: (a) xy-view of the far-field pattern (target mode) at a distance $z = 1$ m away from the membrane. (b) Normalized E-field intensity along the horizontal (x) and vertical (y) lines drawn through the intensity peak.

which is already optimized to be 305 nm below the OAQD. Increasing or decreasing this distance results in a stronger side lobe, as the destructive interference becomes weaker for the side lobes.

In order to fully understand the underlying mechanism for the pronounced vertical emission, we apply Fourier transformation to the recorded real space cavity modes at 823 and 833 nm, displayed in Figure 4.7(a) and (b), respectively. In the meantime, we also calculate and plot the primitive reciprocal lattice vectors of the photonic crystal ($a_1 = 290$ nm)

$$\begin{aligned} \vec{\boldsymbol{V}}_1 &= \frac{2\pi}{a_1}\vec{\boldsymbol{e}}_y + \frac{2\pi}{\sqrt{3}a_1}\vec{\boldsymbol{e}}_x, \\ \vec{\boldsymbol{V}}_2 &= \frac{2\pi}{a_1}\vec{\boldsymbol{e}}_y - \frac{2\pi}{\sqrt{3}a_1}\vec{\boldsymbol{e}}_x. \end{aligned} \tag{4.10}$$

As we can see in Figure 4.7, it is clear that the pronounced vertical emission of the target mode is a result of Bragg-scattering caused by the periodic lattice of the photonic crystal. The target mode exhibits dominant k-space components around the reciprocal lattice point at $\pm(\vec{\boldsymbol{V}}_1 - \vec{\boldsymbol{V}}_2)$, which form a standing wave along the x-direction. Enhanced vertical emission is therefore achieved through Bragg-scattering of these dominant k-space components to the Γ-point ($k_x = k_y = 0$). Additionally, standing waves

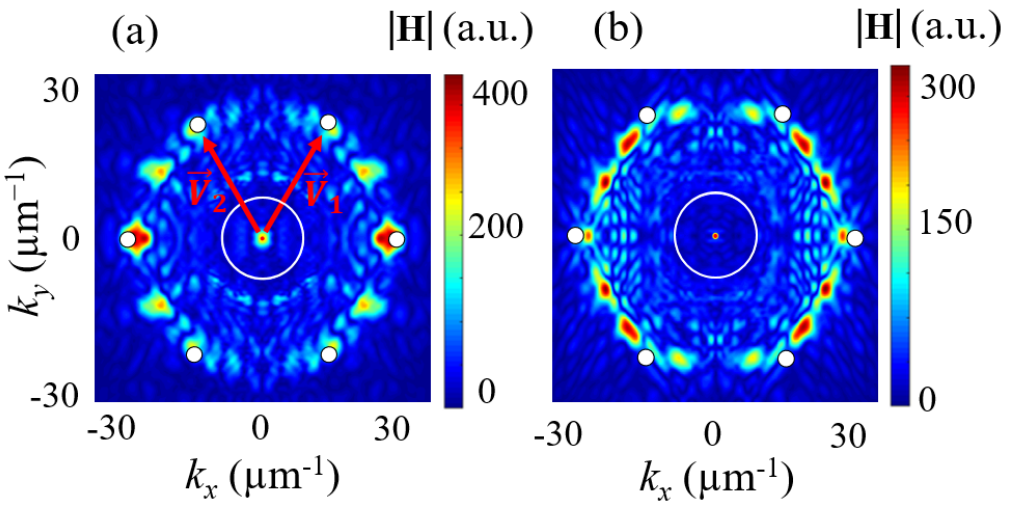

Figure 4.7: (a) Fourier space distribution of the target mode. The red arrows indicate the primitive reciprocal lattice vectors and the white circle represents the light line in free space. The dominant k-space components are located around the reciprocal lattice points. (b) Fourier space distribution of the mode at 833 nm. The dominant field components do not coincide with the reciprocal lattice points.

along the directions of the cavity openings are clearly visible in Figure 4.7(a). On the other hand, we can clearly see that the dominant field components of the 833 nm mode are not at the reciprocal lattice points and thus cannot be efficiently coupled to the Γ-point. This results in the complex far-field emission pattern observed in Figure 4.5(b), which would couple poorly to a single-mode fiber.

4.3.3 Overlap with Gaussian beams

In order to quantitatively evaluate the far-field emission pattern, we calculate the optical overlap (OV(θ)) between the near-field, which is recorded by Monitor 1, and an ideal Gaussian beam with varying divergence angles θ and spatial positions according to equation 4.8. The Gaussian beam is numerically generated based on equations 2.22 to 2.28. Alternatively, the OV can also be evaluated by using the projected far-field pattern shown in Figure 4.6, instead of the near-field. But this approach is more computationally demanding because of the spatial size of the far-field pattern (2 m by 2 m) and the required high spatial resolution ($\lambda/2 = 412$ nm) to

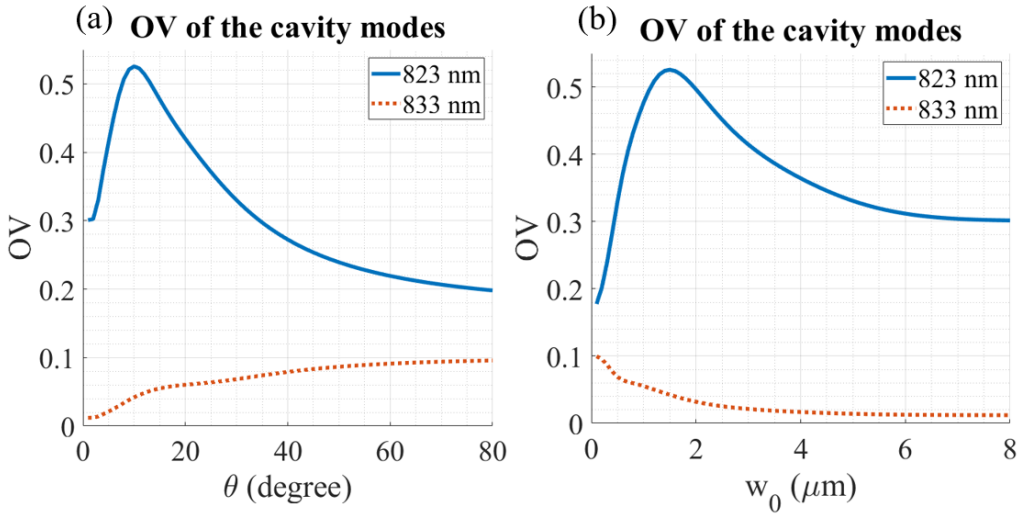

Figure 4.8: OV of the 823 nm target mode and the 833 nm mode as a function of (a) divergence angle θ and (b) beam waist radius w_0. The maximum OV of the target mode is $\mathrm{OV}_{\mathrm{max}} = 0.525$ for $\theta = 10°$ or $w_0 = 1.5\ \mu$m with $\Delta x = 0$, $\Delta y = 0$, $\Delta z = -3.3\,\mu$m. For the 833 nm mode, the OV stays below 0.1 for all θ or w_0 with $\Delta x = 0$, $\Delta y = 0$, $\Delta z = -1.5\,\mu$m.

avoid aliasing the frequency domain, which would result in a data matrix with a size of 4854400 by 4854400. On the other hand, using the near-field is much easier, as the size of the near-field is 5 μm by 5 μm, and we are using a spatial resolution of 10 nm. The size of this data matrix (501 by 501) can be handled easily.

The Gaussian beam is determined by several parameters: the wavelength, the divergence angle θ (or, equivalently, the beam waist radius w_0), the polarization, the propagation direction, and the location of the center of the beam waist $(x_g,\ y_g,\ z_g)$. The wavelength of the Gaussian beam is set to be the same as the investigated cavity mode. The polarization is assumed to be parallel to the orientation of the dipole exciting the PCC. The propagation direction is determined to be the positive z-direction because the GaAs/$\mathrm{Al}_{0.33}\mathrm{Ga}_{0.67}$As membrane spans in the xy-plane and we are collecting the photon emitted in the positive z-direction. The divergence angle θ and the spatial position $(x_g,\ y_g,\ z_g)$ are the parameters to be optimized in order to maximize the OV. Since we are evaluating the integrals in equation 4.8 over the surface of Monitor 1, the Gaussian beam is also sampled on the same surface regardless of θ or $(x_g,\ y_g,\ z_g)$. For convenience, we define

$\Delta x = x_m - x_g$, $\Delta y = y_m - y_g$, and $\Delta z = z_m - z_g$ to be the coordinate distance between the center of the Gaussian beam waist and the center of Monitor 1 ($x_m = 0$, $y_m = 0$, $z_m = 130$ nm).

Figure 4.8 shows the OV as a function of (a) θ and (b) w_0 for the 823 nm target mode and the 833 nm mode. For the target mode, the spatial position of the Gaussian beam is $\Delta x = 0$, $\Delta y = 0$, $\Delta z = -3.3\,\mu$m as a result of optimization. The peak value of OV is $\mathrm{OV}_{\mathrm{max}} = 0.525$ for $\theta = 10°$ or $w_0 = 1.5\ \mu$m with $w_0\theta = \lambda/\pi$. The result suggests that the near-field and thus the far-field emission pattern behaves mostly like a Gaussian beam with $\theta = 10°$. According to Figure 4.6(b), the far-field pattern has a radius of 0.163 m and 0.177 m in the x and y-direction, which results in a divergence angle of arctan(0.163/1) = 9.3° and arctan(0.177/1) = 10.0° in both directions, respectively. The result is in good agreement with the OV calculation. In comparison to the target mode, the OV of the 833 nm mode stays below 0.1 for all investigated θ with an independently optimized spatial position $\Delta x = 0$, $\Delta y = 0$, $\Delta z = -1.5\,\mu$m.

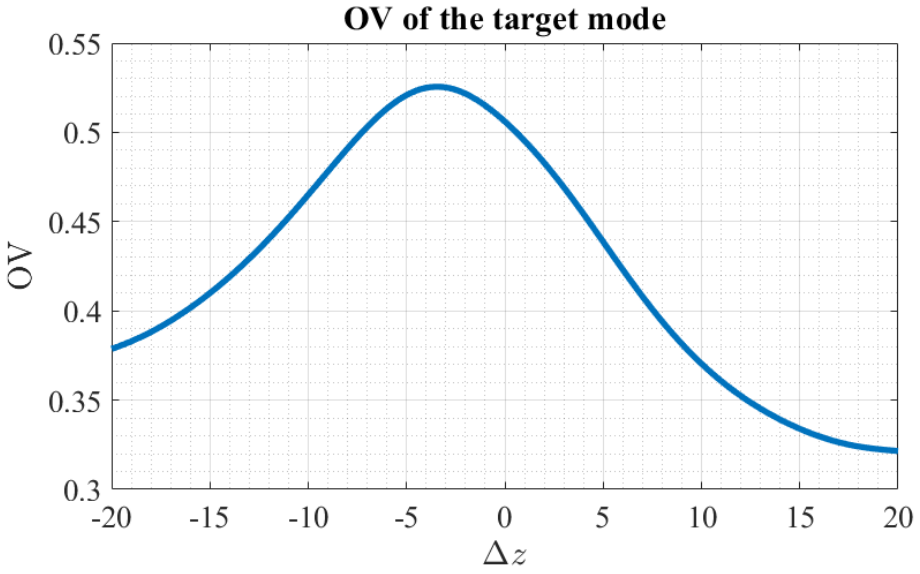

Figure 4.9: OV of the target mode as a function of Δz for $\theta = 10°$ and $\Delta x = \Delta y = 0$. The $\mathrm{OV}_{\mathrm{max}} = 0.525$ is achieved for $\Delta z = -3.3\,\mu$m.

The spatial coordinates of the Gaussian beam are separately optimized to maximize $\mathrm{OV}_{\mathrm{max}}$. Figure 4.9 shows the OV of the target mode as a function of Δz for a fixed $\Delta x = \Delta y = 0$ and $\theta = 10°$. The $\mathrm{OV}_{\mathrm{max}} = 0.525$ is

achieved for $\Delta z = -3.3\,\mu$m. We notice that the optimal Δz has a negative value, which indicates that, on the surface of Monitor 1, the Gaussian beam is still converging towards its beam waist located 3.3 μm above the monitor surface.

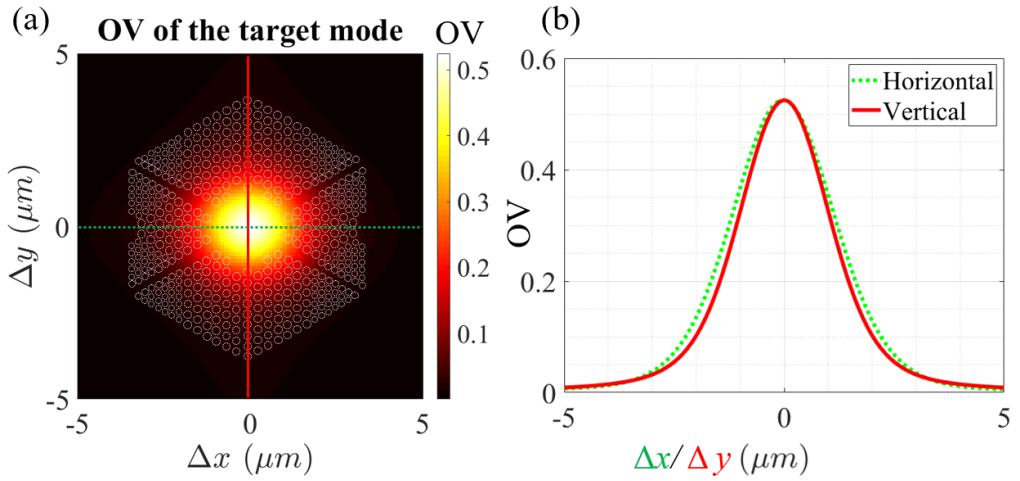

Figure 4.10: (a) OV of the target mode as a function of Δx and Δy for $\theta = 10°$ and $\Delta z = -3.3\,\mu$m. The $\mathrm{OV_{max}} = 0.525$ is located at $\Delta x = \Delta y = 0$. (b) OV along the horizontal (green, dashed) and vertical (red, solid) lines drawn through the central point with $\mathrm{OV_{max}}$.

Figure 4.10(a) depicts the OV as a function of Δx and Δy with a fixed $\Delta z = -3.3\,\mu$m and $\theta = 10°$. The PCC is also shown by white dashed circles. A horizontal green dashed line and a vertical red solid line are drawn through the central point ($\Delta x = \Delta y = 0$), where $\mathrm{OV_{max}} = 0.525$ is achieved. The OVs along the two lines are plotted in Figure 4.10(b). We observe that the alignment needs to be more precise in the xy-plane than in the z-direction. In order to maintain an OV > 0.5, the alignment tolerance is around 7 μm in the z-direction according to Figure 4.9. On the other hand, however, the alignment tolerance is limited to around 0.7 μm in the x and y-direction.

The position of the gold reflector is another factor that influences the OV. The reflector should enhance the central lobe by constructive interference while suppressing the side lobes by destructive interference at its optimal position. Figure 4.11(a) shows the OV of the target mode as a function of θ for different reflector positions, which are defined as the distance between the dipole and the top surface of the gold reflector. The thickness of the

SiO_2 interlayer is also changed accordingly to completely fill the gap between the bottom surface of the GaAs/AlGaAs membrane and the reflector. As we can see in Figure 4.11(b), the optimal distance between the reflector and the dipole is 305 nm with $OV_{max} = 0.525$. Increasing or decreasing this distance results in a reduced OV_{max}.

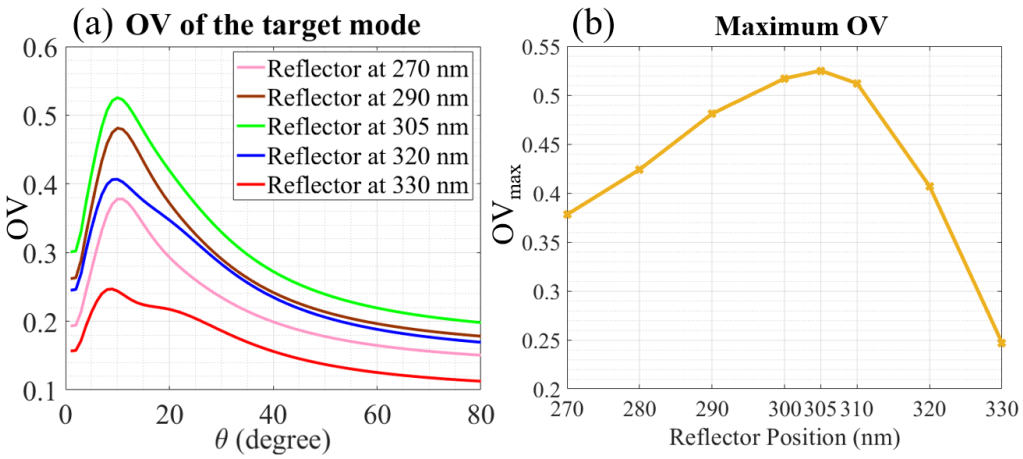

Figure 4.11: (a) OV of the target mode as a function of θ for different mirror positions. (b) OV_{max} for different mirror positions.

In this section, we quantitatively evaluated the OV for the target mode and concluded that its maximum value is $OV_{max} = 0.525$. The divergence angle, the spatial position of the Gaussian beam, and the position of the gold reflector (d) are optimized to be: $\theta = 10°$, $\Delta x = 0$, $\Delta y = 0$, $\Delta z = -3.3\,\mu$m and $d = 305$ nm.

4.3.4 Overall efficiency

In the next step, we are able to calculate the overall efficiencies η of the cavity modes according to equation 4.9. The radiation efficiency η_r can be straightforwardly calculated based on the recorded electromagnetic field recorded by Monitor 1. For the target mode, we obtain $\eta_r = 54.6\%$. As a result, the maximum overall efficiency (η_{max}) is calculated to be $\eta_{max} = \eta_r \times OV_{max} = 28.7\%$ with $\theta = 10°$ assuming optimized positions of the Gaussian beam and the reflector. On the other hand, the radiation efficiency of the 833 nm mode is $\eta_r = 37.2\%$, which results in $\eta_{max} = 3.6\%$ even for large divergence angles. The poor overall efficiency of the 833 nm mode

is obviously a result of the irregular far-field pattern. This observation highlights the importance of careful cavity design.

Figure 4.12 shows the overall efficiencies η for the target mode and the 833 nm mode. Since the radiation efficiency η_r is a fixed value and thus independent of the divergence angle, the curves for η have the same shape as the OVs in Figure 4.8. To demonstrate the effectiveness of the PCC, we also calculated the η without the PCC, which means an un-etched GaAs/$Al_{0.33}Ga_{0.67}$As membrane with the same gate structure, the same SiO_2 interlayer, and the gold reflector at the same distance as the optimal case for the target mode. In this case, we obtain $OV_{max} = 0.600$ for a divergence angle of 54°. The OV_{max} without the PCC is even surprisingly slightly higher than the target mode. However, due to the absence of the in-plane optical confinement, the radiation efficiency drastically reduces to $\eta_r = 7.8\%$. As a result, the maximum overall efficiency is only $\eta_{max} = 4.6\%$ for $\theta = 54°$.

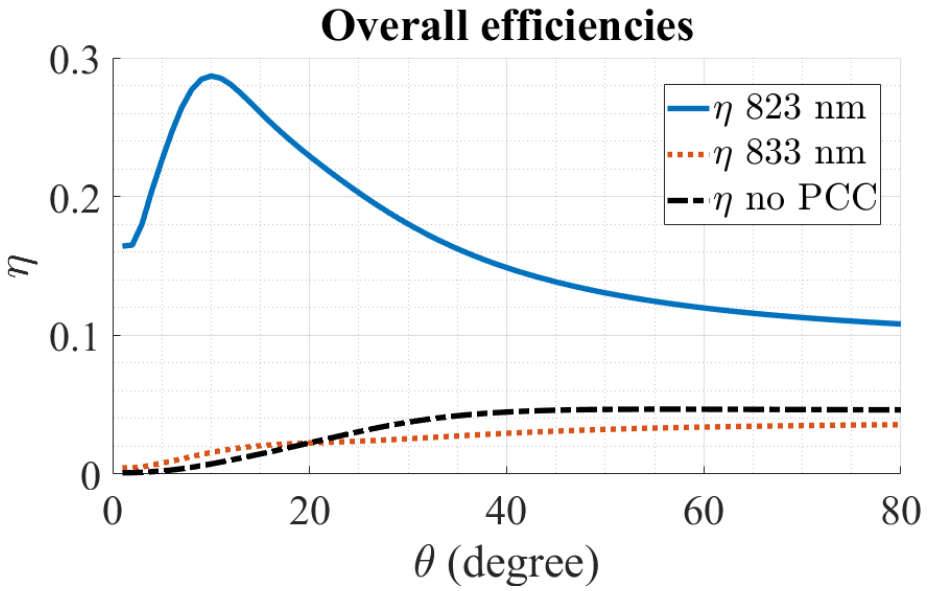

Figure 4.12: Calculated overall efficiencies as a function of θ for the target mode and the 833 nm mode. As a comparison, the overall efficiency without the PCC is also plotted.

The function of the PCC can thus be summarized as enhancing the radiation efficiency while at the same time maintaining a Gaussian emission profile. Moreover, since the PCC significantly reduces the divergence angle

of the emitted Gaussian beam, an objective with a lower numerical aperture and thus with a longer working distance can be used to couple the beam into a single-mode fiber.

4.3.5 Suspended PCC

The main purpose of the SiO_2 interlayer between the membrane and the gold reflector is physically supporting the membrane structure during a membrane transfer process and thus preventing the membrane from breaking or deforming. After the final step of etching the PCC in a dry etching process, it is possible to undercut the SiO_2 interlayer with an additional wet etching process, leaving a suspended membrane structure. In this case, the membrane is free-standing in free space at a certain distance above the bottom reflector.

We evaluated the performance of this suspended PCC structure and noticed that both the radiation efficiency and the OV are increased compared to the case with the SiO_2 interlayer.

Figure 4.13 shows the calculated OV and η of the target mode for the supported (with the SiO_2 interlayer) and the suspended (without the interlayer) PCC structure. The dashed curves represent the OV and η for the suspended structure. As we can see, the OV_{max} is increased from 0.525 to 0.839 at the same divergence angle $\theta = 10°$, when the SiO_2 interlayer is removed. We should notice that the position of the reflector and the Gaussian beam need to be optimized again for the suspended case, which results in $\Delta x = \Delta y = 0$, $\Delta z = -3.5\,\mu$m, and an optimal reflector position at 410 nm. Moreover, the wavelength of the target mode shifts by 2 nm, from 823 nm to 821 nm, due to the increased optical confinement in the z-direction and thus a smaller modal volume. All those adjustments have been considered when calculating the OV_{max} for the suspended PCC structure.

Figure 4.14 shows the far-field pattern of the target mode of the suspended PCC structure. Compared to the far-field of the supported PCC structure (Figure 4.6), we can clearly see that the relative peak intensity of the side lobes reduces from 5.5% to 2.8% in the horizontal cut and from 1.9% to 1.3% in the vertical cut. In addition, the $1/e^2$ intensity radius of

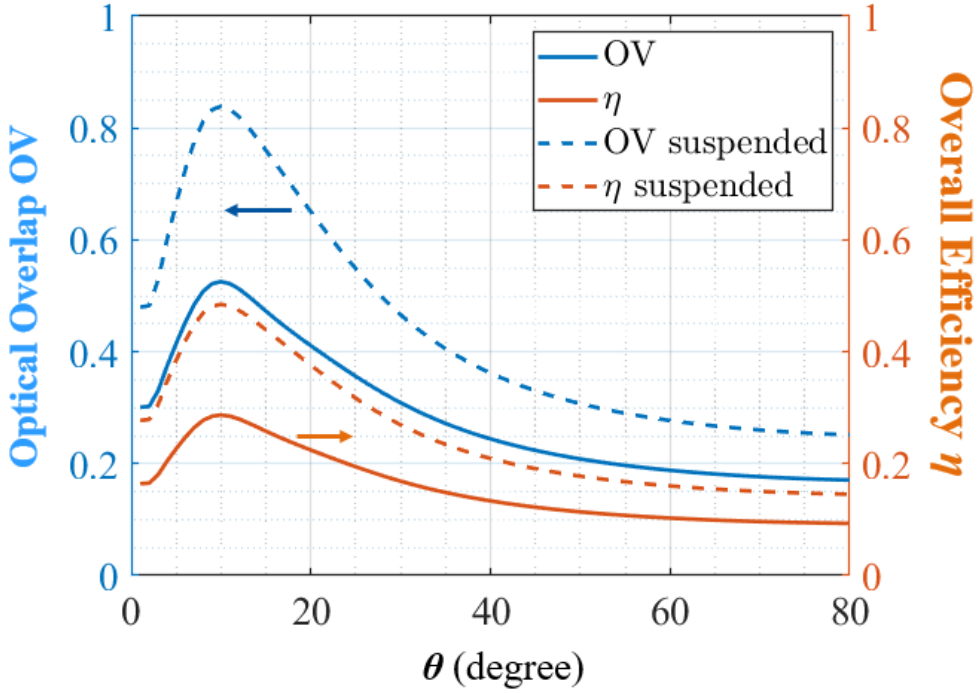

Figure 4.13: OV and η as a function of θ of the target mode for the supported and suspended PCC structure. The reflector position is independently optimized for each case. In the absence of the SiO_2 interlayer, the OV_{max} increases from 0.525 to 0.839 and the η_{max} from 28.7% to 48.5% at $\theta = 10°$.

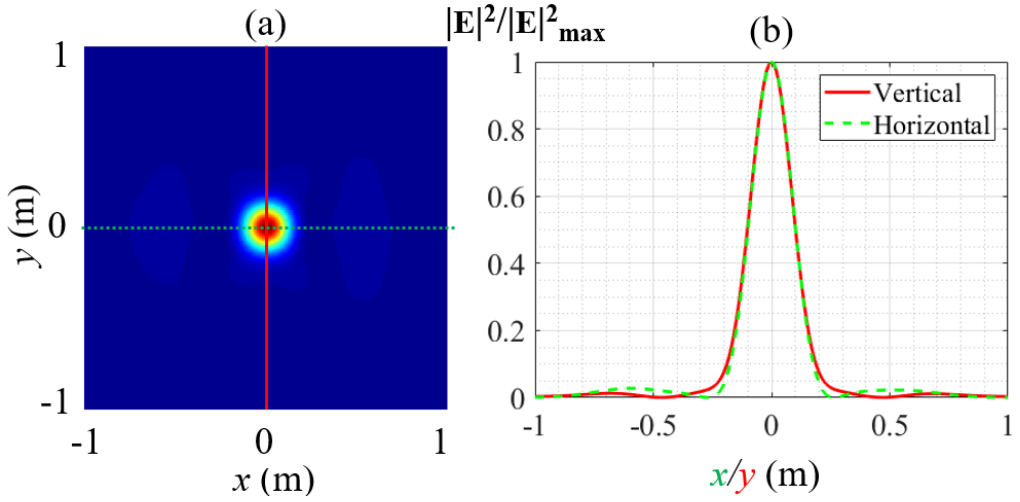

Figure 4.14: Far-field pattern of the target mode for suspended PCC structure. (a) xy-view of the far-field pattern (target mode) at a distance $z = 1$ m away from the membrane. (b) Normalized E-field intensity along the horizontal (x) and vertical (y) lines drawn through the intensity peak.

the central lobe is 0.166 m (9.3° in divergence angle) and 0.175 m (9.9°) in the horizontal and vertical direction, respectively. As a result, the relative asymmetry in this case is 0.009/0.175 = 5.1%, which is smaller than the asymmetry of the supported PCC structure (7.9%). The reduced side lobe intensity and reduced central lobe asymmetry reflect the increased $\mathrm{OV}_{\mathrm{max}}$ of the suspended structure.

The radiation efficiency η_r is also increased from 54.6% to 57.8% by removing the interlayer. The increased η_r can be explained by the increased refractive index contrast at the bottom surface of the membrane, which leads to reduced emission towards the negative z-direction. As a result, the radiation loss at non-perpendicular angles to the reflector's surface also reduces.

The maximum overall efficiency η_{max} for the suspended structure is thus drastically boosted from 28.5% to 48.7%, compared to the supported structure. This comparison highlights the influence of the SiO_2 interlayer on the device's performance. The interlayer inhibits the overall efficiency by, on the one hand, introducing more radiation loss towards the reflector (at non-perpendicular angles). On the other hand, it breaks the reflection symmetry of the structure along the z-direction and induces coupling between the quasi-transverse-electric (quasi-TE) and quasi-transverse-magnetic (quasi-TM) modes [74]. Since the bandgap is open for the TE fields only, this contributes further to the reduction of the overall emission efficiency. A detailed discussion on the mechanisms limiting the device's performance is the main focus of the next section.

4.4 Mechanisms limiting the performance

In this section, we focus on analyzing the mechanisms limiting the overall efficiency of the optical interface. There are in total three loss channels that reduce the radiation efficiency and the optical overlap:

1. The coupling between the quasi-TE and the quasi-TM modes, which is a result of the broken reflection symmetry along the z-direction. We call it **TE-TM coupling loss** for simplicity.

2. The radiation loss via the bottom interface towards the reflector at non-perpendicular angles. We call it **downward radiation loss**.

3. The optical absorption of the Au/Ti gates due to the surface plasmon polaritons (SPP) at the metal/vacuum, metal/GaAs, and metal/SiO_2 interfaces excited by the evanescent electromagnetic fields. We call it **metal absorption loss**.

4.4.1 TE-TM loss

As already explained in Figure 3.4(b) in Section 3.2.1, the PCC (with lattice constant $a_1 = 290$ nm, hole radius $r_1 = 109$ nm) supports a TE bandgap from 717 nm to 1021 nm. In cooperation with the four cavity openings, which have a TE mini-stopband from 793 nm to 845 nm (Figure 3.8), no TE mode propagating out of the cavity exists in the wavelength range from 793 nm to 845 nm. However, for the TM modes, such a bandgap does not exist as illustrated in Figure 3.4(b).

In order to clearly define the TE and TM modes, a reflection symmetry is always necessary. In this case, the symmetric and anti-symmetric eigenmodes are orthogonal to each other, and we can define the symmetric modes as the TE modes and the anti-symmetric modes as the TM modes. This reflection symmetry is assumed when calculating the band structures of the PCC and the cavity openings.

In section 4.1, we have justified the approximation of the OAQD by an in-plane dipole located in the central quantum well layer of the membrane. When the reflection symmetry along the z-direction is preserved, only TE mode can be excited, as the electric field of TM modes has a node at the central plane and thus cannot be excited by the dipole. However, when the reflection symmetry is broken in the z-direction by the asymmetric SiO_2 interlayer and by the asymmetric gate system (see Figure 3.1), the original TE and TM modes mix with each other and the orthogonality is destroyed. In this case, the original "pure" TE modes become the "quasi"-TE mode and so do the TM modes. We call them "quasi" because the electromagnetic fields of those modes resemble the shape of the "pure" modes, with perturbations caused by the mode mixing.

Since the TM modes are leaky due to the absence of a TM bandgap, the quasi-TE modes are also lossy and result in the TE-TM coupling loss. Figure 4.15 shows the k-space profile of the target cavity mode together with the equifrequency contours of the quasi-TM photonic crystal modes at the same wavelength, represented by the red dotted contours. The presence of field components on the equifrequency contours of the quasi-TM photonic crystal modes suggests the presence of the in-plane TE-TM coupling loss.

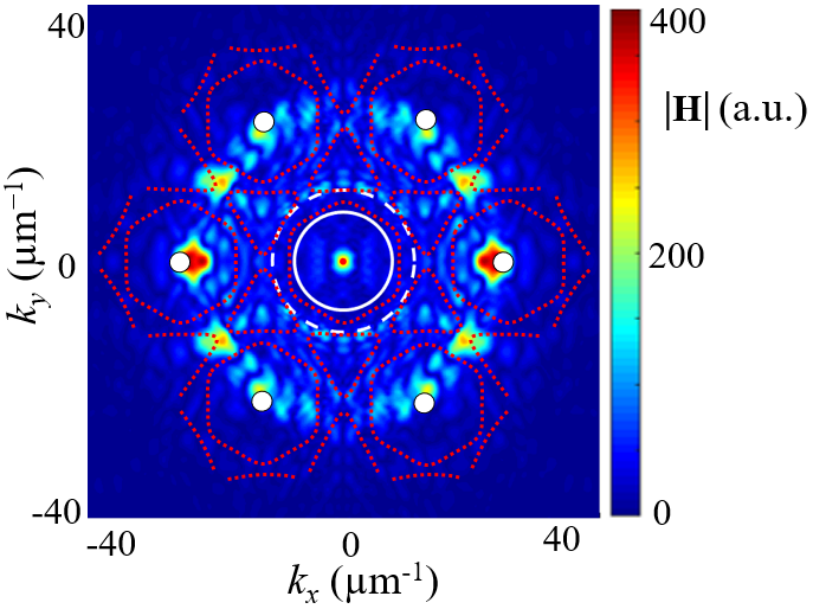

Figure 4.15: Fourier space distribution of the target quasi-TE cavity mode at 823 nm overlaid with the equifrequency contours of the leaky quasi-TM photonic crystal modes at the same wavelength. The light line of vacuum (SiO_2) is depicted by the white solid (dashed) circle, and the k-vectors of the quasi-TM photonic crystal modes are indicated by the red dotted contour. An overlap between the quasi-TE cavity mode field components and the quasi-TM photonic crystal modes is observed.

By depositing an additional SiO_2 layer on top of the membrane, we would be able to restore the mirror symmetry in the z-direction and thus suppress the TE-TM coupling. However, this also compromises the optical confinement by closing the optical bandgap of the photonic crystal and the mini-stopband of the cavity openings, which results in reduced radiation efficiency and a lower optical overlap according to our simulations.

4.4.2 Downward radiation loss

Downward radiation loss also limits the performance of our optical interface. The bottom reflector reflects light traveling in the negative z-direction and enhances the Gaussian emission towards the top, which is emitted perpendicular to the GaAs/$Al_{0.33}Ga_{0.67}As$ membrane surface. However, photons that are emitted at non-perpendicular angles to the reflector's surface might experience multiple reflections that guide them along the 2D slab formed by the bottom reflector and the membrane in the xy-plane. There is a chance that these photons are guided away from the device and thus cannot be detected by Monitor 1, resulting in reduced radiation efficiency.

The white dashed circle and white solid circle in Figure 4.15 represent the light cone of SiO_2 and the light cone of vacuum, respectively. The light inside the SiO_2 light cone but outside the vacuum light cone stays guided and thus is eventually lost in the interlayer. As a result, undercutting the SiO_2 interlayer reduces the downward radiation loss and improves the radiation efficiency, as shown in section 4.3.5. The light within the vacuum light cone might still escape the slab and be detected by the monitor. However, due to the non-perpendicular radiation angle, this leads to a distortion of the emitted field profile and reduces the OV. Undercutting the interlayer reduces this distortion due to the increased refractive index contrast. In this case, less light escapes the bottom interface at non-perpendicular angles.

4.4.3 Metal absorption loss

The optical absorption of the Au/Ti gates introduces another loss mechanism due to the presence of SPPs at the metal/vacuum and metal/SiO_2 interfaces excited by the evanescent electromagnetic field of the target cavity mode. To reduce the SPP absorption, the gates/wires are predominantly routed along the y-direction to ensure that the metal/vacuum and metal/SiO_2 interfaces are mostly parallel to the dominant electric field component inside the cavity, which is E_y. This orientation is chosen because the dominant electric field component of SPP modes is perpendicular to the metal/dielectric interface [68]. By routing the gates/wires in this manner, the interaction between

the SPPs and the cavity mode can be reduced, leading to decreased optical absorption.

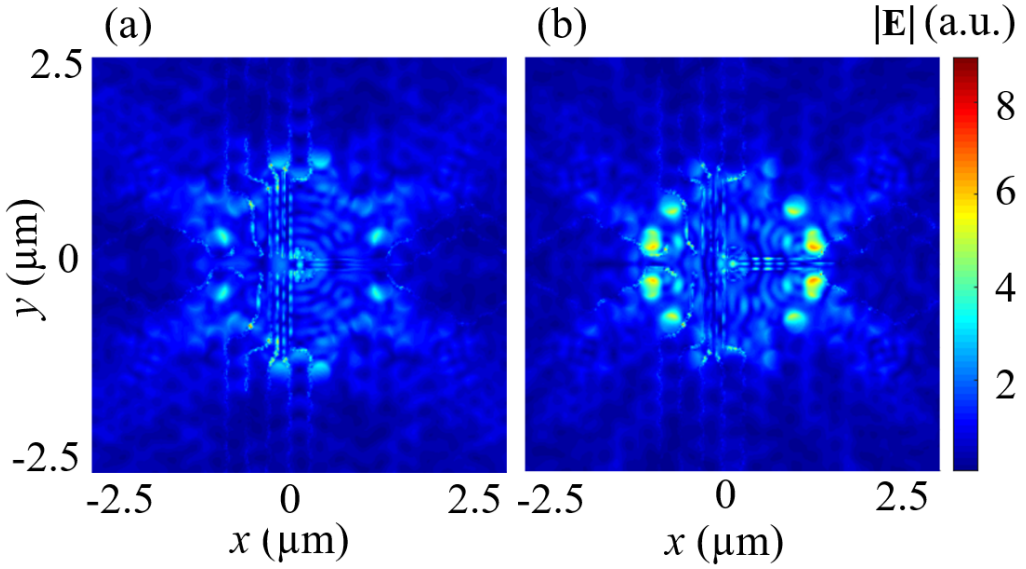

Figure 4.16: Near-field electrical field intensity of the target mode recorded by the Monitor 1. The PCC is excited by (a) x-dipole at 826 nm (b) y-dipole at 823 nm. The SPPs are clearly visible at the location of metal gates. We notice that the intensities of the SPPs are relatively stronger in the case of x-dipole excitation, compared to the intensity of the anti-nodes of the cavity mode.

Figure 4.16 displays the electrical field amplitude of the target mode recorded by Monitor 1. The target mode of the PCC is excited by an x-dipole in (a) and a y-dipole in (b). Since the target mode is characterized by dominant k-space components at the location of the reciprocal lattice points of the PCC, an x-dipole is also able to excite the target mode. In this case, the dominant k-space component is not located at the lattice points $\pm(\vec{\boldsymbol{V}}_1 - \vec{\boldsymbol{V}}_2)$, which is true for y-dipole excitation (see Figure 4.7), but at the lattice points $\pm\vec{\boldsymbol{V}}_1$ and $\pm\vec{\boldsymbol{V}}_2$. Moreover, due to the broken C_6 symmetry of the H4 cavity by the cavity openings and by the metal gates, the wavelength of the target mode is slightly different for both cases, with 823 nm for y-dipole and 826 nm for x-dipole excitation.

We can clearly see the presence of the SPPs at the locations of the metal gates for both excitation schemes. In order to compare the relative intensities of the SPPs for both cases, we use the same color bar scale to plot the electrical field amplitudes. For the x-dipole case, we see that the field

amplitude is relatively weak inside the PCC, but strong SPPs exist at the edges and corners of the metal gates. On the other hand, for the y-dipole case, the field amplitude is relatively strong inside the PCC compared to the SPPs at similar locations, which indicates weaker interaction between the cavity mode and the SPPs. These observations confirm our assumption that routing the gates/wires parallel to the dominant electric field component inside the cavity does reduce the excitation of SPPs and improve the overall performance of the device.

4.4.4 Analysis on partial quality factors

In this section, we quantitatively evaluate the influence of the three different loss mechanisms (TE-TM loss, downward radiation loss, and metal absorption loss) on the overall performance of the optical interface by calculating their partial quality factors (Q). Four different schemes are investigated: x/y-dipole excitation with/without the SiO_2 interlayer.

The results are summarized in Table 4.1. The overall Q_{total} is evaluated by fitting the resonance peak with a Lorentzian curve and calculating the full-width-half-maximum (FWHM). In order to obtain the partial quality factors, we first calculate the ratio of the lost power to the total power emitted by the dipole Γ for the different loss channels. Then, those power ratios are converted into the corresponding partial quality factors by:

$$\Gamma_{\text{partial}} = \frac{P_{\text{partial}}}{P_{\text{dipole}}}, \quad Q_{\text{partial}} = \frac{Q_{\text{total}}}{\Gamma_{\text{partial}}}, \tag{4.11}$$

where 'partial' stands for 'gates', 'TE-TM', 'bottom' and 'top'. P_{dipole} is the power emitted by the dipole source. P_{gate} is the power absorbed by the metal gates, and $P_{\text{TE-TM/bottom/top}}$ is the power radiated to the side, bottom and top of the cavity. In addition to the already mentioned three loss channels, we include 'top' to account for the desired upward emission and use the radiation efficiency η_r to replace the notation Γ_{top}. A high η_r is obtained if Q_{top} is substantially lower than all the other partial Q-factors.

The power monitors used to record P_{top} are the Monitor 1 introduced in Figure 4.2. In order to record P_{bottom}, another identical monitor is placed below the bottom surface of the membrane at the same distance (130 nm) to

	SiO_2, y-dipole	SiO_2, x-dipole	Suspended y-dipole	Suspended x-dipole
Q_{total}	232	161	293	236
$\Gamma_{\text{gates}}/Q_{\text{gates}}$	25.8% / 899	30.9% / 521	34.4% / 851	42.5% / 555
$\Gamma_{\text{TE-TM}}/Q_{\text{TE-TM}}$	3.5% / 6620	6.6% / 2426	1.4% / 20285	2.3% / 10301
$\Gamma_{\text{bottom}}/Q_{\text{bottom}}$	15.9% / 1456	22.5% / 716	5.9% / 4996	7.8% / 3026
η_r/Q_{top}	54.7% / 424	39.4% / 409	57.8% / 507	46.3% / 510
OV_{max}	0.526	0.347	0.839	0.719
η_{max}	28.7%	13.7%	48.5%	33.3%

Table 4.1: Calculated power ratio Γ and partial quality factors for each loss channel. The spatial position and the divergence angle of the Gaussian beam, and the reflector's position are optimized independently for all 4 cases to obtain the OV_{max}. The polarization of the Gaussian beam is always in the direction of the dipole moment.

the dipole source as Monitor 1. Considering that the size of the two monitors is 5 μm by 5 μm in the xy-plane, and they are placed very closely to the surfaces of the membrane with a distance of 20 nm, the recorded powers are closely equal to the real P_{top} and P_{bottom} with negligible differences.

A monitor box is constructed by placing four additional monitors connecting the edges of the two already existing monitors. The summation of the powers recorded by those four side monitors corresponds to $P_{\text{TE-TM}}$, which is the power escaping the PCC within the membrane.

Finally, P_{gate} is recorded by placing monitors sandwiching the metal gates in the z-direction and calculating the power difference between them. For example, an additional monitor identical to Monitor 1 is placed 5 nm below the top surface of the membrane. The difference between the recorded powers of this monitor and Monitor 1 corresponds to the absorbed power by the gates on the membrane's top surface. The same method is applied to the bottom gates. P_{gate} is equal to the summation of both calculated values.

We see from Table 4.1 that the partial quality factor of the metal gates (Q_{gates}) is highly dependent on the dipole orientation. For an x-dipole, the

Q_{gates} is 521 and 555 with and without the SiO_2 interlayer, respectively. In contrast, the same Q_{gates} increases to 899 and 851 for a y-dipole due to reduced SPP absorption. This confirms our assumption that routing the wires parallel to the dominant electrical field component E_y reduces the corresponding absorption losses. This was further verified by evaluating one by one the absorption losses for each electrode. We found that the sensor and OAQD trap/guard electrodes, that had to be routed along the x-direction, induce most of the absorption losses.

The $Q_{\text{TE-TM}}$ is significantly correlated to the presence or absence of the interlayer as expected. When the SiO_2 interlayer is present, the $Q_{\text{TE-TM}}$ is reduced by one order of magnitude due to the increased TE-TM coupling loss. Interestingly, even for a suspended PCC structure, there is still a slight but non-negligible TE-TM coupling loss (with a power ratio of 1.4% for the y-dipole and 2.3% for the x-dipole excitation), which is possible since the gates also break the symmetry in the z-direction, as the GDQD is only patterned on the top interface of the $GaAs/Al_{0.33}Ga_{0.67}As$ membrane.

Similar to the $Q_{\text{TE-TM}}$, the Q_{bottom} is also closely related to the SiO_2 interlayer. When the interlayer is present, the Q_{bottom} is reduced by around 4 times, because the reduced refractive index contrast enhances the downward emission as already explained in section 4.4.2.

We notice that the Q_{top} is around 500 for suspended structures and around 400 for supported structures. The drop of the Q_{top} when the interlayer is present is also expected due to the increased downward emission, since the part of the downward radiation which is reflected back up and escapes through the top surface contributes to the upward radiation and thus reduces the Q_{top}. This reduction of Q_{top} in the presence of the interlayer is helpful as it makes the upward radiation compete more favorably with the other ones. However, the drop in Q_{top} is not sufficient to compensate for the drop of the other partial Q-factors, as seen in the reduced radiation efficiency. The dipole orientation has minimal influence on Q_{top} as expected.

Table 1 also includes the calculation results for the OV_{max} in all four scenarios, in which the spatial position and the divergence angle of the Gaussian beam, and the reflector's position are independently optimized to maximize the OV_{max}. We notice a pronounced correlation between OV_{max}

and Q_{bottom}, which may be explained by multiple reflections and partial guiding experienced by the downward emission in the interlayer. When it eventually escapes the structure through the top, it distorts the emission profile and reduces the OV_{max}. Based on these observations, undercutting the SiO_2 interlayer would be desirable from a performance perspective, even though it increases the complexity of the fabrication process.

4.4.5 Best performing scheme

Since we already know which loss mechanisms influence the overall performance of our optical interface, it would be interesting to know what would be the highest possible efficiency without those loss mechanisms.

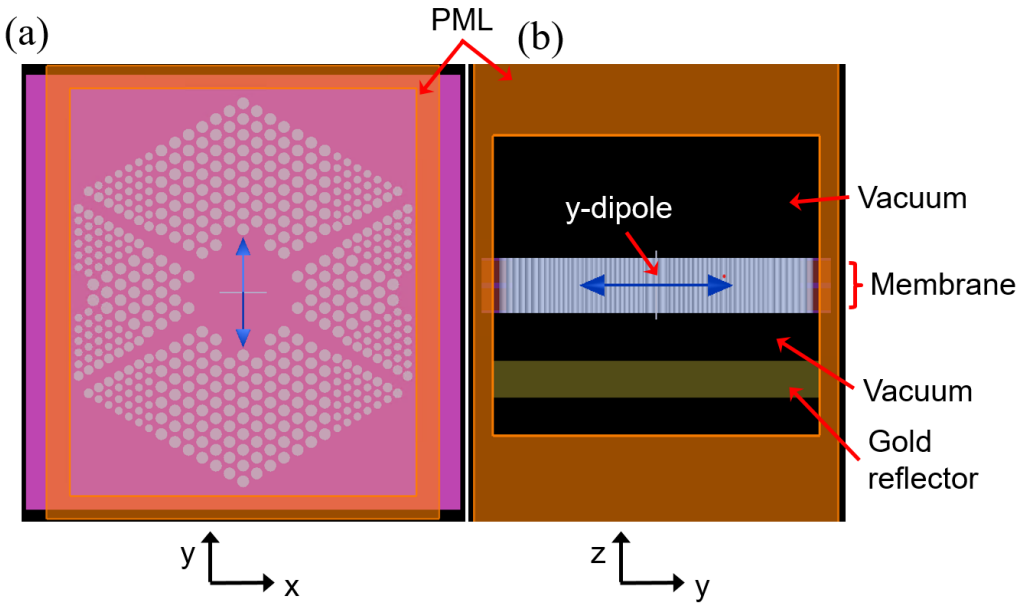

Figure 4.17: The optical interface without the gate system or the SiO_2 interlayer. (a) the xy-view, (b) the yz-view

By undercutting the SiO_2 interlayer, the downward radiation loss and the TE-TM coupling loss are significantly reduced as seen in Table 4.1. Further removing all the metal gates would remove the metal absorption loss and also the residual TE-TM coupling loss. Although the singlet-triplet qubit and the OAQD would not exist anymore after the removal of the gate system, an analysis on such a device would still provide useful insight for researchers who focus on increasing the extraction efficiencies of single

photon sources based on self-assembled quantum dots (SAQD) or other quantum emitters that do not require a gate system.

Figure 4.17 shows the device without the interlayer or the gate system. We are still using a y-dipole to represent the light source. The bottom reflector is placed at an optimized distance of 420 nm to the dipole. The calculated OV of the target mode as a function of θ is plotted in Figure 4.18. The $\mathrm{OV}_{\mathrm{max}}$ is 0.998 at $\theta = 13°$. The maximum overall efficiency is $\eta_{\mathrm{max}} = 92.3\%$ with a radiation efficiency of $\eta_r = 92.5\%$. Those results are similar to one of our publications [42], where a complete H4 cavity is used with transparent ITO gates defining the OAQD.

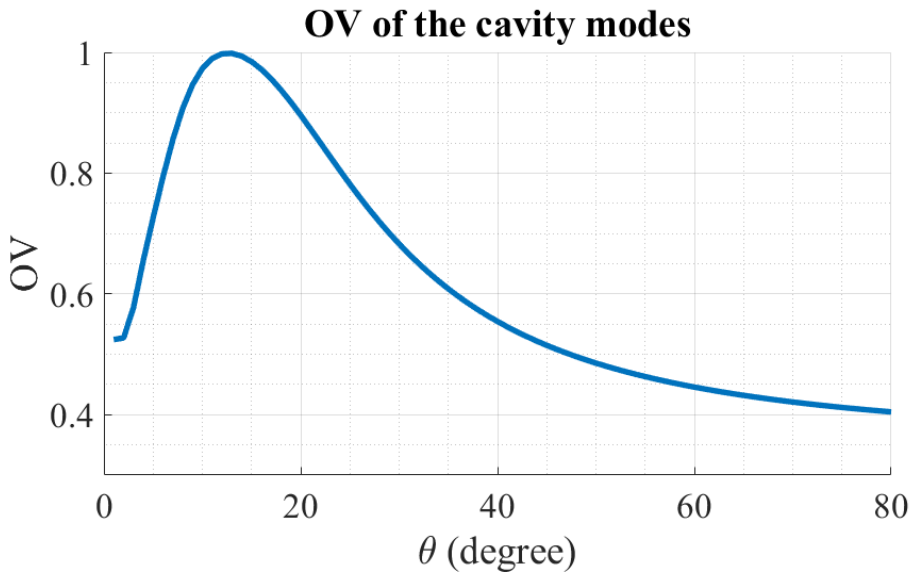

Figure 4.18: OV of the target mode for the optical interface without the interlayer or the gate system. The $\mathrm{OV}_{\mathrm{max}}$ is 0.998 at $\theta = 13°$. The maximum overall efficiency is $\eta_{\mathrm{max}} = 92.3\%$ with a radiation efficiency of $\eta_r = 92.5\%$.

By comparing those results to that of a suspended membrane with the gate system, we notice that the metal absorption loss and the TE-TM coupling loss due to the asymmetric gate reduce the $\mathrm{OV}_{\mathrm{max}}$ from 0.998 to 0.839, the η_r from 92.5% to 57.8%, and thus the overall efficiency η_{max} from 92.3% to 48.5%. The significant reduction of the efficiency highlights the influence of the gate system on the performance. The optimization of the gate systems to reduce the optical loss is thus of great importance in future research.

4.5 Fabrication tolerance analysis

In order to provide a guideline to the device fabrication, we investigate the influence of the variation of the size and the sidewall angle of the etched holes. The main results are summarized in Table 4.2 and Table 4.3. The reflector is placed 305 nm under the dipole for all simulations and is separated from the membrane by an SiO_2 interlayer.

Δr	λ_{target}	η_r	OV_{max}	η_{max}
+10 nm	813 nm	40.9%	0.297	12.1%
+5 nm	818 nm	49.9%	0.451	22.5%
0 nm	823 nm	54.6%	0.526	28.7%
-5 nm	829 nm	42.7%	0.361	15.4%
-10 nm	834 nm	23.5%	0.171	4.0%

Table 4.2: Influence of hole radius deviation on performance. The same radius deviation is applied to all holes, including that of the cavity opening.

As we can see in Table 4.2, a hole radius deviation of ±5 nm already has a significant influence on the η_{max}. A DOE (design of experiment) including a sweep on the hole radius is thus necessary considering the fabrication uncertainties. Such a sweep would increase the chance of finding a device with the optimal parameters.

Table 4.3 summarizes the results with varying side wall angles. Variations of sidewall angles primarily impact the properties of the structure due to the change in the effective (averaged) radius of the holes. To remove this effect and investigate the primary effect of sidewall angle, the nominal radius at the top side of the structure was adapted to maintain the radius at the center of the membrane constant, which can be realized by a DOE. We notice that the η_{max} stays above 20% up to a sidewall angle of ±10°.

Sidewall angle	Δr	λ_{target}	η_r	OV_{max}	η_{max}
+11°	+23 nm	824 nm	41.5%	0.417	17.3%
+9°	+19 nm	823 nm	46.8%	0.458	21.4%
+7°	+13 nm	825 nm	44.4%	0.466	20.7%
+5°	+10 nm	823 nm	44.8%	0.492	22.0%
+3°	+6 nm	823 nm	52.5%	0.520	27.3%
+2°	+3 nm	824 nm	51.7%	0.505	26.1%
+1°	+1 nm	824 nm	52.0%	0.509	26.5%
0°	0 nm	823 nm	54.6%	0.526	28.7%
-1°	0 nm	821 nm	54.1%	0.536	29.0%
-2°	-3 nm	822 nm	54.2%	0.545	29.5%
-3°	-5 nm	822 nm	54.3%	0.540	29.3%
-5°	-10 nm	823 nm	52.2%	0.525	27.4%
-7°	-13 nm	823 nm	50.2%	0.559	28.1%
-9°	-16 nm	822 nm	47.0%	0.519	24.4%
-11°	-19 nm	821 nm	44.2%	0.476	21.0%
-13°	-22 nm	820 nm	40.9%	0.416	17.0%

Table 4.3: Influence of hole sidewall angle on performance. Positive sidewall angles indicate increasing hole radii along the positive z-direction, towards the top surface of the structure at which the nominal radius is defined. For different sidewall angles, we also adapted the hole radius to keep the wavelength of the target mode within the tunable wavelength range of the gate-defined exciton trap, which is from 820 nm to 825 nm. The hole radius deviation is the difference between the design value and the actual hole radius at the top surface of the membrane. In these cases, the radius at the quantum well plane stays constant around 109 nm.

4.6 Conclusion

In this chapter, we systematically modeled and analyzed the performance of our optical interface by performing 3D FDTD simulations. The PCC is designed in such a way that the dominating Fourier components of the cavity mode at the target wavelength coincide with the reciprocal lattice vectors of the photonic crystal. As a result of strong Bragg scattering, we obtain enhanced vertical emission with a pronounced central lobe, which has a high OV with a narrow Gaussian beam compatible with low numerical aperture collection optics. According to our simulations, the interface provides an overall efficiency of $\eta_{\max} = 28.7\%$ with $\mathrm{OV}_{\max} = 0.525$ and $\eta_r = 54.7\%$, assuming an SiO_2 interlayer filling the space between the reflector and the membrane. The performance can be further increased by undercutting this SiO_2 interlayer below the PCC. In this case, the overall efficiency is calculated to be $\eta_{\max} = 48.5\%$ with $\mathrm{OV}_{\max} = 0.839$ and $\eta_r = 57.8\%$. We also analyzed the mechanisms limiting the performance of the interface and noticed that optimizing the gate system to reduce metal absorption loss would be a possible future research direction.

Chapter 5

Device Fabrication

In this chapter, the fabrication process and the fabricated samples are introduced.

The fabrication of the optical interface is done by Sebastian Kindel[1] and Dr. Thomas Descamps[2] under the supervision of Prof. Hendrik Bluhm[3] at the JARA-FIT Institute for Quantum Information, Forschungszentrum Jülich GmbH, and RWTH Aachen University.

5.1 Fabrication methods

The fabrication process of the optical interface was created by Dr. Thomas Descamps based on a modified Epoxy-Bond-And-Stop-Etch (EBASE) technique. Only a brief introduction will be given in this section. For more details, please refer to the original publications [75, 52] as well as our previous conference paper [76].

The process starts with an MBE-grown heterostructure GaAs/AlGaAs wafer, where sacrificial layers and the GaAs/AlGaAs membrane are grown on top of a GaAs substrate. Figure 5.1 illustrates the entire process, which can be described by eight consecutive steps:

1. Metallic markers are deposited on the as-grown surface in a lift-off process after patterning a resist with electron beam lithography (EBL).

[1]sebastian.kindel@rwth-aachen.de
[2]descamps@physik.rwth-aachen.de
[3]bluhm@physik.rwth-aachen.de

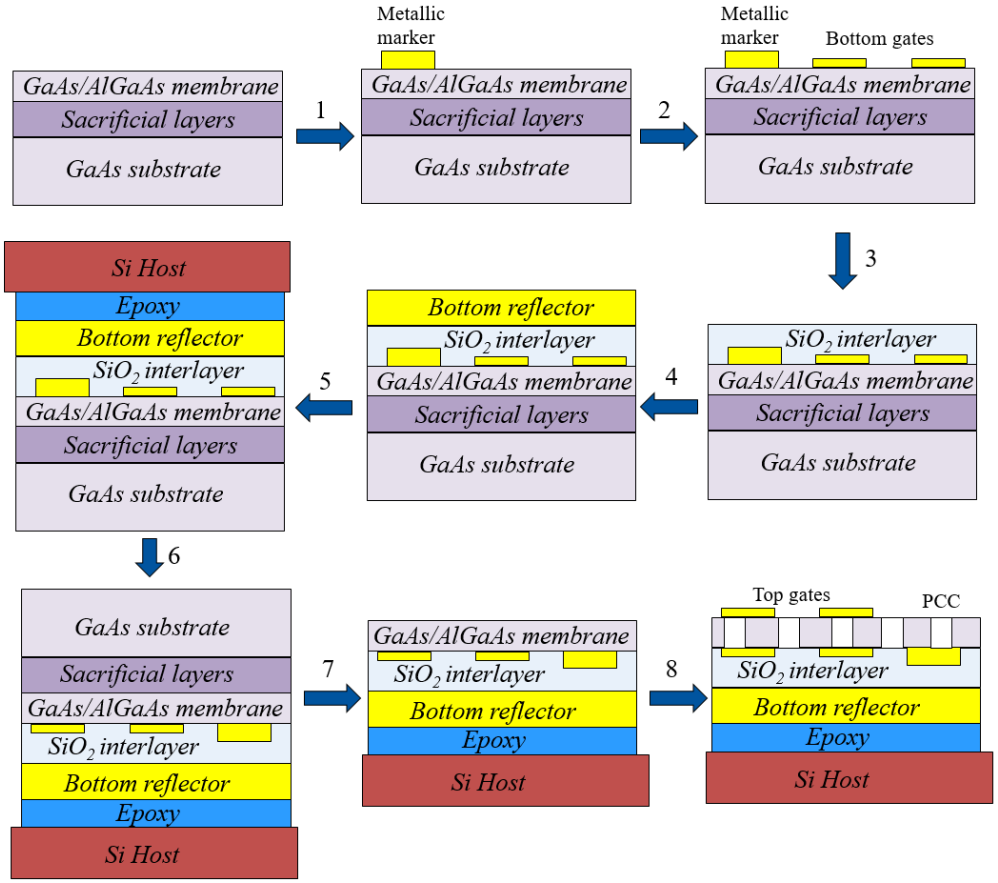

Figure 5.1: Fabrication process of the optical interface. The thicknesses of the layers are only an illustration and are not to scale. An additional chemical etching process can be applied to undercut the SiO_2 interlayer after the final step.

These markers are used to accurately align the metal gates and the photonic crystal cavity (PCC) in the following steps.

2. Bottom gates are deposited using the same method as the metallic markers.

3. The SiO_2 interlayer is deposited using chemical vapor deposition (CVD).

4. The bottom reflector is deposited.

5. The entire layer stack is permanently bonded to a Si host substrate via epoxy.

6. The chip is flipped in order to process the other side.

7. The GaAs substrate and the sacrificial layers are removed by chemical etching, exposing the other side of the membrane for further processing.

8. Top gates are deposited in the same manner as the bottom gate. The holes of the PCC are patterned by e-beam resist and transferred to the membrane by inductively-coupled reactive ion etching. Thanks to the small thickness of the heterostructure membrane, the metallic marker on the other side is visible and used to align the top gate and the PCC.

In order to fabricate a suspended membrane structure, an additional chemical etching process can be applied after the final step to undercut the SiO_2 interlayer, which is not shown in Figure 5.1.

5.2 Fabricated samples

Until the date of thesis writing (Sep. 2025), the fabrication of the complete optical interface is not entirely successful due to the difficulties of process optimization and the lack of BCl_3 gas, which is required to reduce the oxidation of the aluminum during the etching of the PCC holes [77]. However, preliminary test samples are available which show the potential of the fabrication method.

The two most difficult and important steps are the deposition of the metal gates and the etching of the PCC. In order to fabricate the metal gates on both sides of the membrane and to route the metal wires between the holes of the PCC, a high alignment accuracy is necessary. In section 5.2.1, membranes with PCCs and metal gates are presented, which show that the required high alignment accuracy down to ±15 nm can be achieved.

On the other hand, a well-functioning PCC requires that the etched holes have a high quality (low side wall roughness, well-defined radius, small side wall angles, etc.). Due to unpredictable fabrication uncertainties, a design of experiments (DOE) is necessary, where parameter sweeps are included, to find the optimal PCC by means of quick turnaround experiments.

In section 5.2.2, membranes with PCCs but without the metal gates are presented. In this section, we primarily discuss the DOE and other practical considerations for the experimental characterization of the PCCs. Metal gates are not incorporated in this case as individual adjustments and alignments are required for every single PCC with different parameters.

5.2.1 PCC with metal gates

Figure 5.2 shows three scanning electron microscope (SEM) images of a complete H4 cavity fabricated on a 220 nm GaAs/AlGaAs membrane with a lattice constant of $a = 282$ nm and a hole radius of $r = 96$ nm. Metal gates are patterned on both the top and the bottom surfaces of the membrane (Figure 5.2(a)). The gates on the top surface have a thickness of 9 nm (2 nm Ti + 7 nm Au), while the bottom gates (Figure 5.2(b)) have an increased thickness of 25 nm (5 nm Ti + 20 nm Au) for better visibility seen from the top side. The wires have a width of 30 nm on both sides and are carefully routed between the etched air holes (Figure 5.2(c)). The PCC and the gate geometry are different from the simulation model, as this is an early-stage test sample. The membrane is directly epoxy bonded to a Si substrate without the implementation of an SiO_2 interlayer or a gold reflector.

A high alignment accuracy is necessary to route the top and bottom gates through the PCC. In order to achieve this accuracy, metallic markers (not shown in Figure 5.2) are fabricated on the bottom surface by deposition

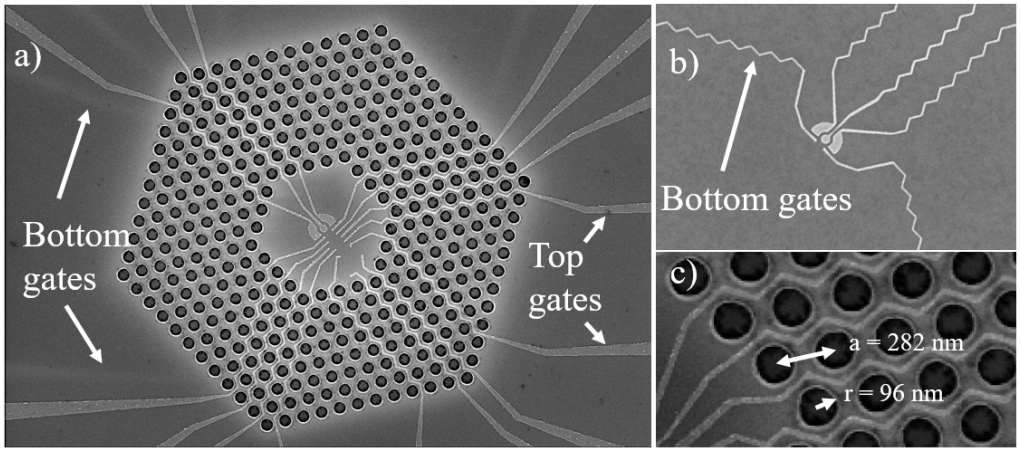

Figure 5.2: SEM images of a 220 nm GaAs/AlGaAs membrane with a complete H4 PCC and top and bottom metal gates. (a) The top surface of the membrane. The top gates are clearly visible. The bottom gates are also visible through the thin membrane. (b) The bottom surface with the bottom gates before the membrane is flipped and epoxy bonded to an Si substrate. (c) Enlarged image showing the routing of the metal wires through the holes. The hole radius is 96 nm with a spacing of 282 nm. The sample is fabricated by Dr. Thomas Descamps. Theses images are already published in one of our conference papers [76].

of Ti (5 nm) and Au (80 nm) in a lift-off process after patterning of a 200 nm thick resist (AR-P 6200) with EBL. These high-definition markers are used to accurately overlay the wires and the PCC in three consecutive EBL steps.

First, the wires for the bottom gates are fabricated using the same method as the markers, with EBL applied to an 80 nm thick resist and a lift-off process. After the sample is flipped and epoxy bonded to a Si substrate, the GaAs substrate and sacrificial layers are etched away to access the other side of the membrane. Although the metallic markers are now underneath the 220 nm membrane, they can still be recognized by the electron beam writer. Second, the top gates are fabricated in the same manner as the bottom gates. Finally, the holes are patterned on a 600 nm thick resist by a last EBL step and transferred to the sample by inductively coupled plasma reactive ion etching with a mixture of Cl_2 and Ar. As we can see from Figure 5.2(c), an alignment accuracy down to 15 nm is achieved between the wires and the holes. Detailed fabrication methodology and chemical recipes are available in the PhD thesis of Dr. Thomas Descamps

[75].

To improve the sample quality, BCl_3 or N_2 can be added to the etching gases to reduce the oxidation of aluminum [77]. Unfortunately, due to the lack of such passivation gases at the time of fabrication, the side walls of the etched holes (mainly $Al_{0.33}Ga_{0.67}As$) have a large surface roughness, which inhibits the functionality of the PCC. For this reason, this sample is not appropriate for experimental characterization.

As a further example, Figure 5.3 depicts another test structure (fabricated by Sebastian Kindel) with the metal gates and the PCC fabricated on a pure 220 nm GaAs membrane. The gate geometry and the PCC, including four cavity openings, are the same as the simulation model (Figure 3.2) with an increased lattice pitch of $a = 306$ nm and reduced hole radius of $r = 99$ nm to ease the alignment process. Metal gates (5 nm Ti + 20 nm Au) are patterned on both sides of the membrane. Due to the view angle, the gates on the bottom side are not visible. An SiO_2 interlayer or a gold reflector is not implemented, and the membrane is directly epoxy bonded to a Si host.

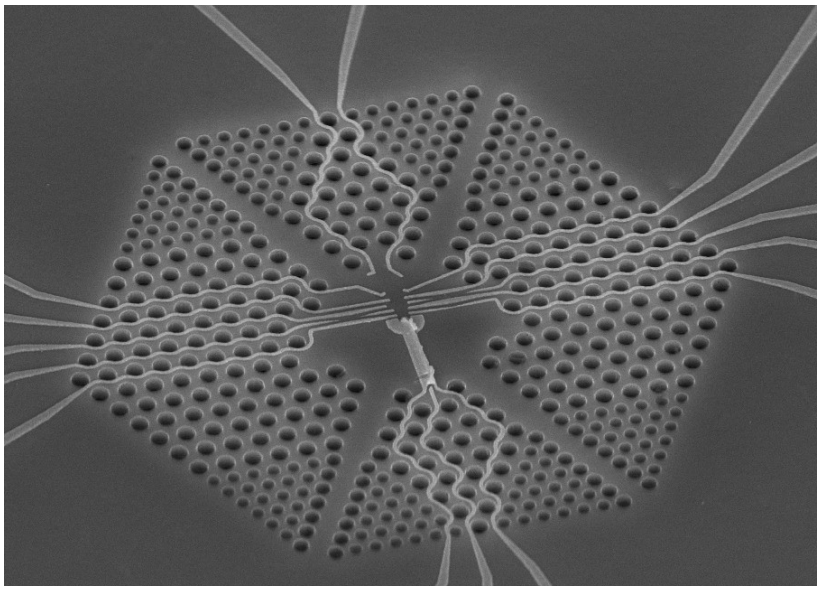

Figure 5.3: A pure 220 nm GaAs membrane with gates and the PCC including four cavity openings. The routing of the wires is successful despite of the cavity openings. Gates are also patterned on the bottom side of the membrane. Due to the view angle, the gates on the other side is not visible. This sample is fabricated by Sebastian Kindel.

As we can see, the metal wires with a width of 30 nm are successfully routed between the air holes with enough alignment accuracy. The cavity openings do not inhibit the wiring of the OAQD and the quantum dot charge sensor despite the reduced lattice pitch and hole radius. Resist residue is observed on the wires connected to the trap gate and the guard gate in the cavity center. The gates for the GDQD also show imperfections close to the cavity center. The fabrication flow is currently under optimization, and we expect that these imperfections will be fixed in the near future.

5.2.2 PCC without metal gates

In this section, we introduce the DOE of the PCCs, in which the E-beam dose, the lattice constant, and the hole radius are systematically scanned.

Figure 5.4 shows the overview of the DOE, which consists of four different fields marked by a), b), c) and d). Field a), which is not lithographically printed on the membrane, illustrates the different geometries of the PCCs in the same column of fields b) and c). Fields b) and c) both contain three 10 by 10 matrices. Each element in the matrices is a PCC with different lattice constants or hole radii. The sweep directions of a and r are indicated by the arrows. Field d), printed on the membrane, shows the E-beam dose (with the unit $\mu\mathrm{C/cm^2}$) of all PCCs in fields b) and c). Different E-beam doses (with identical parameter sweeps) are applied on the same membrane sample.

In the field c), the lattice pitches, from top to bottom, are determined according to

$$\begin{aligned} a_1 &= 270 : 4 : 306\,\mathrm{nm}, \\ a_2 &= 199 : 3 : 226\,\mathrm{nm}, \\ a_3 &= 199 : 3 : 226\,\mathrm{nm}. \end{aligned} \tag{5.1}$$

In the meantime, the hole radii, from left to right, are described by

$$\begin{aligned} r_1 &= 99 : 2 : 117\,\mathrm{nm}, \\ r_2 &= 68 : 1 : 77\,\mathrm{nm}, \\ r_3 &= 85 : 1 : 94\,\mathrm{nm}. \end{aligned} \tag{5.2}$$

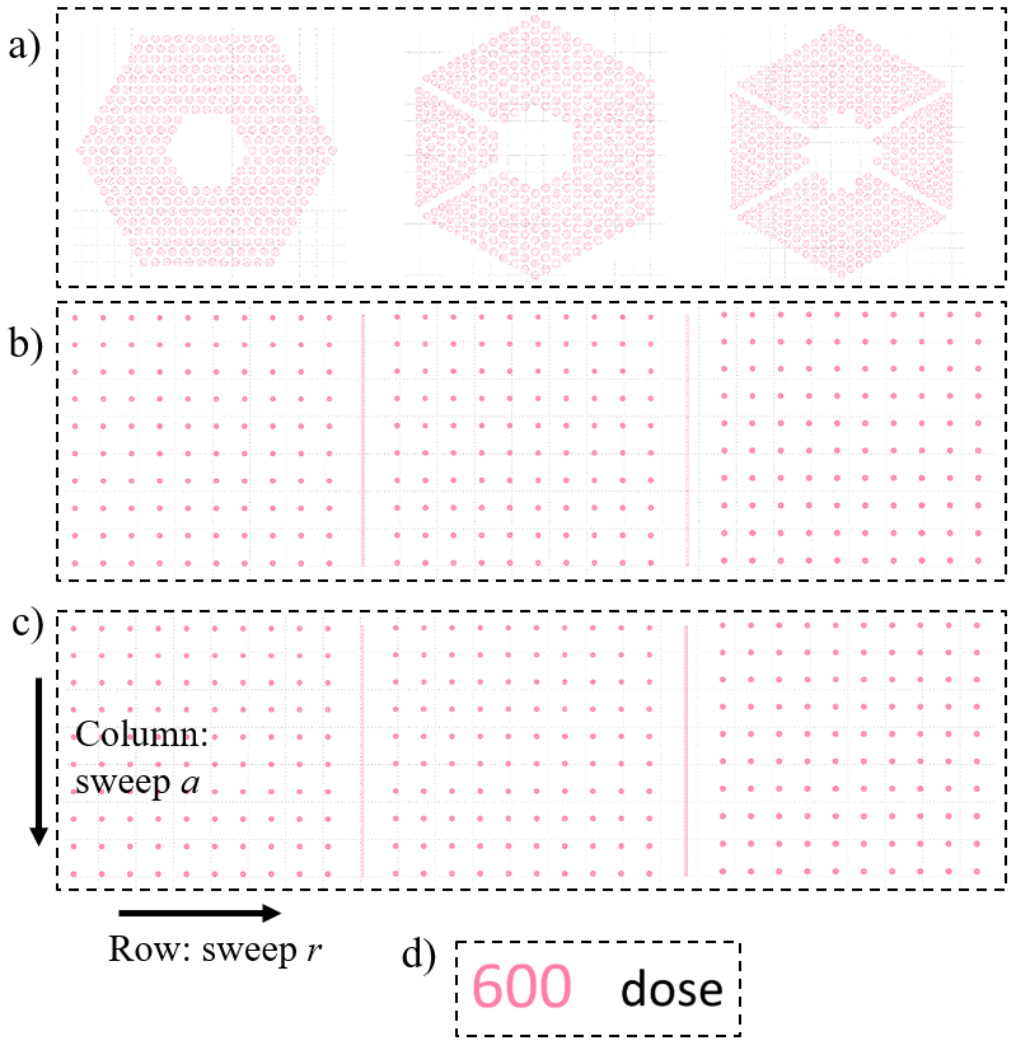

Figure 5.4: The DOE of PCC. Designed in collaboration with Sebastian Kindel. a) Geometries of the PCC in the corresponding column. It is not printed on the membrane sample. b) PCC matrices with parameter sweeps on lattice constant and hole radius. c) The same as b), but with different sweep ranges. d) E-beam dose mark, printed on the membrane.

The definition of the lattice constants and the hole radii is explained in Figure 3.5. The parameter sweeps are determined in such a way that the desired values are in the middle of the sweep. This increases the possibility of finding an optimal device under the influence of fabrication imperfections.

In field b), the parameters are swept in a similar manner but with different up-scaled ranges:

$$\begin{aligned} a_1 &= 304 : 4 : 340\,\text{nm}, \\ a_2 &= 225 : 3 : 252\,\text{nm}, \\ a_3 &= 225 : 3 : 252\,\text{nm}, \end{aligned} \tag{5.3}$$

and

$$\begin{aligned} r_1 &= 112 : 2 : 130\,\text{nm}, \\ r_2 &= 78 : 1 : 87\,\text{nm}, \\ r_3 &= 94 : 1.4 : 107\,\text{nm}. \end{aligned} \tag{5.4}$$

The up-scaled PCCs in this field are used for quick-turnaround measurements under room temperature (RT), which are presented in the next chapter. These measurements allow for a fast characterization of the quality and functionality of the PCCs without the need to cool down the devices to cryogenic temperatures.

Due to the temperature dependence, the bandgap energy of GaAs shifts from 1.52 eV (816 nm) to 1.42 eV (872 nm) when the temperature is increased from 4 K to 300 K. As a result, GaAs is not transparent at 823 nm under RT. For this reason, the PCCs in the field c) are not appropriate for those quick turnaround measurements. By upscaling the PCCs in the field b), we are able to shift the target mode from 823 nm to longer wavelengths up to 980 nm, in which GaAs is fully transparent, and thus RT measurement is possible.

Figure 5.5 shows one example PCC on a GaAs/$Al_{0.33}Ga_{0.67}As$ membrane without metal gates or a back reflector fabricated by Sebastian Kindel. As we can see, the air holes have good quality with small side wall roughness. This membrane sample (U14) is used for RT characterization in the next chapter.

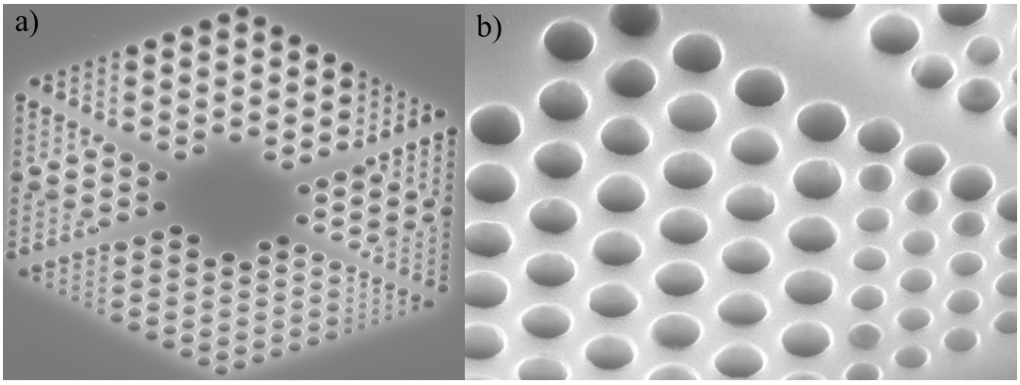

Figure 5.5: A PCC etched on a GaAs/$Al_{0.33}Ga_{0.67}As$ membrane (U14) without metal gates or back reflector fabricated by Sebastian Kindel. a) Overview of the PCC, b) zoomed-in image showing good air hole quality.

5.3 Conclusion

In this chapter, we have introduced the fabrication method and shown some preliminary samples of our optical interface. A complete optical interface containing the PCC, the metal gates, and the back reflector is not available yet, because the fabrication process needs further optimization. However, we have made significant progress by showing that the required alignment accuracy better than ± 15 nm between the PCC and the metal gates can be achieved, which plays a central role in the entire process. The DOE of the PCCs is also introduced, which includes parameter sweeps to compensate for the fabrication imperfections and also contains up-scaled PCCs for fast RT measurements, which is the main topic of the next chapter.

Chapter 6

Cross-polarized Room Temperature Reflection Measurements

In this chapter, we discuss the cross-polarized room temperature (RT) reflection measurement, which was carried out in the visible-wavelength lab of IPH by the author of this thesis. Those quick-turnaround measurements allow for a fast characterization of the quality and the functionality of the photonic crystal cavities (PCCs) without the need to use a liquid helium cryostat.

6.1 Experimental design

6.1.1 Measurement setup

Figure 6.1 shows the schematic figure for the cross-polarized setup for RT reflection measurement. Two continuous-wave (CW) tunable lasers are used in our measurements: A Toptica CTL 950 diode laser (CTL) with a tuning range from 910 nm to 980 nm and a linewidth of 10 kHz, and a NKT Photonics supercontinuum laser (NKT) which consists of a white light source (SuperK EVO) and a tunable high-contrast filter (SuperK LLTF Contrast VIS HP8), which supports a tuning range between 400 nm and 1000 nm and a linewidth < 2.5 nm.

The CTL laser has a smaller tuning range but a higher optical power and a smaller linewidth, which allows for precise measurements on the reflection spectra and clear visualizations of the far-field patterns. On the other hand, the NKT laser has a substantially wider tuning range, in which 800 nm to 1000 nm is utilized in our measurements, but a large linewidth and a relatively low optical power, especially at wavelengths longer than 900 nm. For this reason, we mainly use the NKT laser to compensate for the insufficient tuning range of the CTL laser and to obtain broader reflection spectra. For the concrete analysis regarding the far-field patterns, we use the more precise CTL laser.

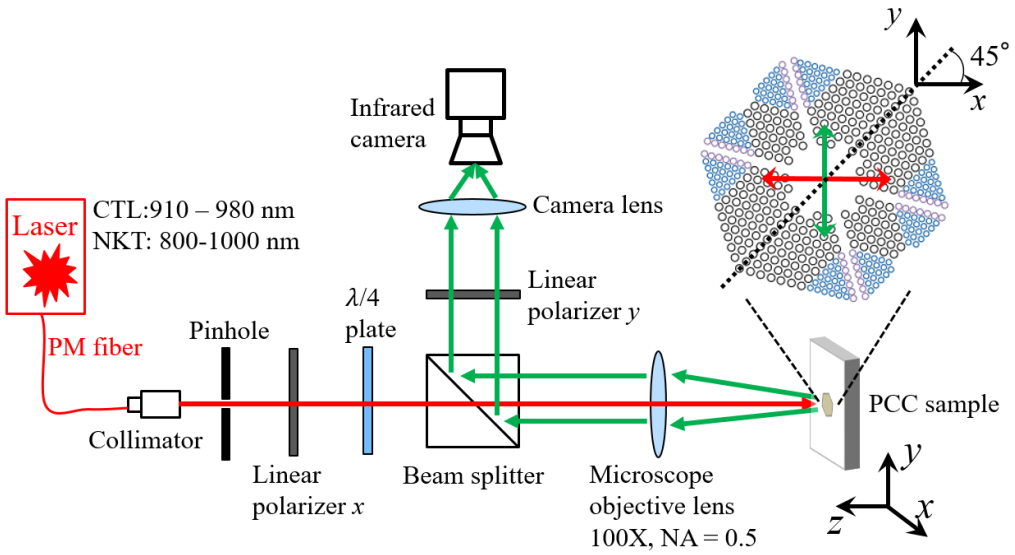

Figure 6.1: Schematic figure of the cross-polarized setup for the RT reflection measurement. The red arrow represents the excitation beam with an x-polarization, while the green arrows show the detection beam with a y-polarization.

The light emitted from the laser is guided by a polarization maintaining (PM) single mode fiber to a collimator (Thorlabs F220 APC-850), which couples the light from the fiber to a free space Gaussian beam with a waist diameter of around 1.7 mm, as indicated by the red arrow. A pinhole plate is used to spatially filter the beam, and thus allows for better control over the position and the size of the focal spot. A smaller pinhole results in a larger, but less bright, focal spot. In the following experiments, unless otherwise mentioned, we use a pinhole with a diameter of 500 μm (Thorlabs P500K).

A linear x-polarizer (Thorlabs LPVIS050-MP2) defines the polarization of the excitation beam. An achromatic quarter wave plate (Thorlabs AQWP05M-980) is mounted on a high-precision rotation mount (Thorlabs CRM1PT/M) and placed right after the x-polarizer to compensate for any ellipticity that might be introduced by the other optical components [78]. The excitation beam is focused on the PCCs by a microscope objective lens (Mitutoyo Plan Apo NIR Infinity Corrected Objective, magnification = 100X, NA = 0.5, working distance = 12 mm).

The GaAs/AlGaAs membrane, epoxy bonded to a Si host, is mounted on a two axes tiltable stage (Thorlabs POLARIS-K1M4/M), which is further fixed on an XYZ-translation stage (Thorlabs NanoMax Stage MAX313D/M). In order to facilitate the cross-polarized measurement, the membrane is rotated about the z-axis by 45°, as depicted in the inset in Figure 6.1.

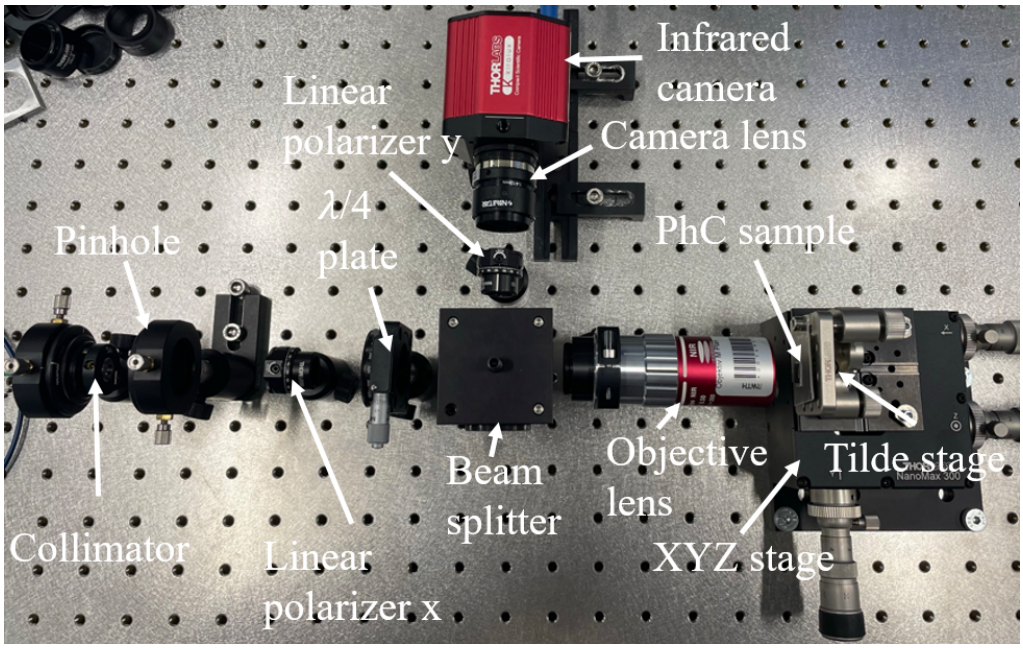

Figure 6.2: Picture of the setup for the RT reflection measurement. The entire setup is covered by a black box to block ambient light.

The reflected light from the PCCs is collected by the same objective lens and reflected to the detection arm by a beam splitter (Thorlabs BS014, 50:50 non-polarizing beam splitter). A second linear polarizer (Thorlabs LPVIS050-MP2) oriented in the y-direction defines the polarization of the detection beam (green arrows). A camera lens (Thorlabs MVL12WA,

effective focal length = 12 mm) is used to focus the detection beam to the CMOS sensor of an infrared camera (Thorlabs Kiralux CS135MUN).

Figure 6.2 shows a real picture of the setup. Since we are working in the NIR infrared range and the camera also registers visible light, it is necessary to cover the entire setup with a black box (not shown in Figure 6.2) that blocks the ambient light. For the alignment of the setup, a NIR detector card (Thorlabs VRC4) is utilized to visualize the infrared beam. An LED lamp is used to illuminate the GaAs/AlGaAs membrane surface in order to observe the PCCs etched through the membrane. The high spatial resolution (pixel size: 4.8 μm by 4.8 μm) of the infrared camera and the high magnification (100x) of the objective lens allow for a clear identification of the PCCs in the camera view.

6.1.2 Cross-polarized configuration

We designed the cross-polarized measurement setup (Figure 6.1) based on the publication by W. C. Stumpf [79], in which the reflection of a photonic crystal L3 cavity is measured. In a cross-polarized configuration, the excitation and detection beams have orthogonal polarizations, in our case the x-polarization for the excitation and the y-polarization for the detection, which allows for an optimal rejection of the excitation beam in the detection arm. Similar cross-polarized setups are used for resonance photoluminescence of quantum dots [78].

Figure 6.3 illustrates the cross-polarized configuration. The axes of reflection symmetry of the PCC are represented by the dashed lines labeled by x' and y', while the excitation and detection polarizations are shown by the red and green arrows labeled by x and y, respectively. The angle between x' and x (or between y' and y) is 45°. Due to the presence of the four cavity openings, the C_6 symmetry of a complete H4 cavity is reduced to two different reflection symmetries with symmetry axes x' and y' (Figure 6.3(a)). As a result, the cavity modes with different polarizations (x' or y') become non-degenerate and can be independently excited by the excitation beam with an x-polarization. In this case, the PCC is similar to a rectangular Fabry-Pérot cavity made of metallic mirrors with different

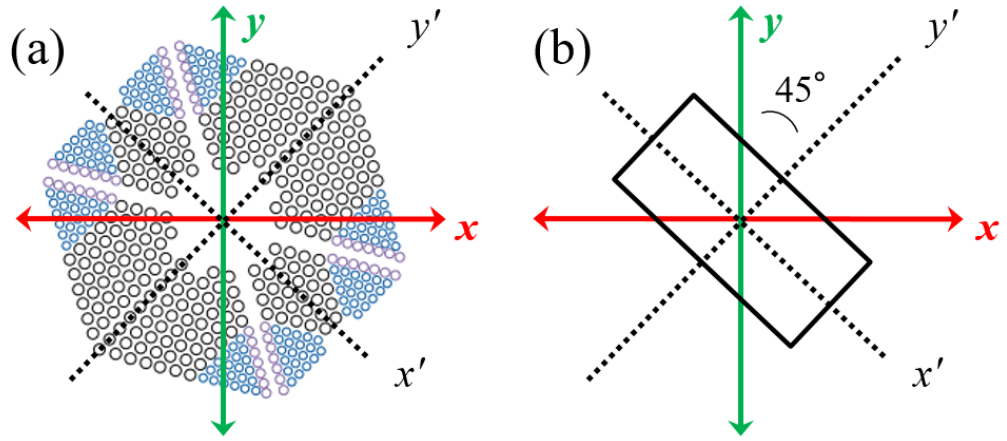

Figure 6.3: Schematic illustration of the cross-polarized configuration. The symmetry axes of the cavity are indicated by dashed lines labeled by x' and y'. The excitation and detection polarization are shown by the red and green arrows labeled by x and y. (a) The PCC rotated by 45°, (b) As a heuristic example, a Fabry-Pérot cavity with the same orientation.

side lengths (Figure 6.3(b)). When the y'/x'-polarized cavity modes are excited, their far-field emission patterns are projected onto the detection polarization y and recorded by the IR camera with the camera lens removed. Since both the excitation and detection polarization have a finite overlap with the main E-field component of the cavity mode, it can be efficiently excited and recorded.

In a cross-polarized setup, it is important to fully reject any remaining excitation light, as it distorts the far-field patterns recorded by the camera. However, the birefringence of the other optical components (the semiconductor chip, the beam splitter, the objective lens, etc.) causes small but inevitable linear to elliptical polarization distortions [78]. This results in a non-zero y-polarized component in the excitation beam, which interferes with the detection beam and distorts the far-field patterns.

In order to eliminate this undesired ellipticity in the excitation beam, a quarter-wave plate is mounted on a high-precision rotation mount and placed in the excitation arm before the beam splitter (see Figure 6.1). By iteratively tuning the relative angle between the two linear polarizers and the fast axis of the quarter-wave plate, we are able to compensate for the ellipticity and thus fully suppress the y-polarized component. According

to our experience, this step is of great importance to obtain undistorted far-field patterns.

6.1.3 Measured sample and measurement process

The measured chip is the GaAs/$Al_{0.33}Ga_{0.67}As$ membrane (U14) with PCCs but without metal gates or a back reflector. The DOE and the geometry of this sample is already introduced in section 5.2.2. As a systematic investigation, we measured 10 PCCs with lattice pitches $a_1 = 304 : 4 : 340$ nm and hole radii $r_1 = 112 : 2 : 130$ nm. Those 10 PCCs are located on a diagonal line of the third column (PCCs with four cavity openings) of the field b) with an E-beam dose of 600 $\mu C/cm^2$, as shown in Figure 5.4. Representative SEM images for four measured PCCs are depicted in Figure 6.4. As we can see, the holes are well-defined with small sidewall roughness. On the other hand, undesired E-beam resist residue is observable for some of the PCCs.

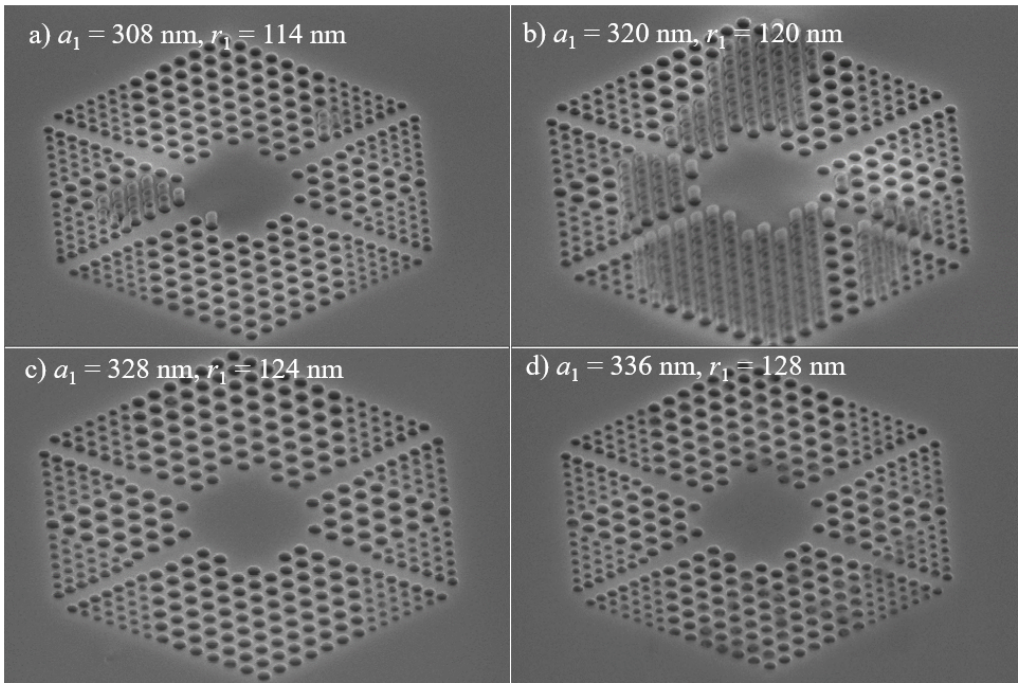

Figure 6.4: Representative SEM images of the measured PCCs. The holes are well defined, but unwanted resist residue is also present. a) $a_1 = 308$ nm, $r_1 = 114$ nm, b) $a_1 = 320$ nm, $r_1 = 120$ nm, c) $a_1 = 328$ nm, $r_1 = 124$ nm, d) $a_1 = 336$ nm, $r_1 = 128$ nm.

The measured PCCs are up-scaled from the original design to shift the

wavelength of the target mode to be larger than the bandgap wavelength of GaAs, which is 870 nm under RT. According to our simulations, the target mode is shifted from 823 nm to 873 nm and to 949 nm, for the PCC with the smallest pitch of 304 nm and the largest pitch of 340 nm, respectively. As a result, the optical absorption of GaAs is negligible for the target mode of all those 10 PCCs.

When the optical path is aligned and the optimal suppression of the excitation beam is achieved, we carry out the measurement process consisting of following steps:

1. Focus the laser beam on the selected PCC.
2. Remove the camera lens of the IR camera to observe the far-field.
3. Adjust the position of the PCC by fine-tuning the translation stage until a symmetric far-field pattern is obtained, which suggests that the center of the laser spot coincides with the cavity center.
4. Adjust the exposure time of the camera to avoid over- or under-exposure.
5. Sweep the wavelength of the tunable laser (the CTL or the NKT laser) and record the far-field patterns for each wavelength. This process is controlled by Python programs.
6. Calculate the reflection spectra by integrating the pixels of the recorded far-field patterns. This step can be further optimized by using a photodetector with a higher sensitivity and a better linear response than the CMOS sensors of the currently used IR camera.

6.2 Measurement results

6.2.1 Results with tunable diode laser

Figure 6.5(a) shows the reflection spectra of all 10 PCCs excited by the tunable diode CTL laser. The full tuning range from 910 nm to 980 nm is swept with a step size of 0.1 nm. The y-axis shows the lattice pitch a_1 of

the PCCs from 304 nm to 340 nm (from top to bottom) with a step size of 4 nm. The measured spectra are individually normalized and plotted at the vertical positions corresponding to the lattice pitches. For better visualization, Figure 6.5(b) plots the same spectra as a 2D image.

As we can see, families of resonance peaks are clearly visible in Figure 6.5(a) and (b), which are highlighted by dashed lines and are labeled by numbers from 1 to 5. As the lattice pitch a_1 increases, the wavelength of the resonance peaks also increases due to the up-scaling.

The far-field patterns for all 5 mode families are summarized in Figure 6.6. As we can see, the peaks from the same mode family have similar far-field profiles, which systematically evolve as the lattice pitch changes. Gaussian-like far-field patterns with a pronounced center lobe and symmetrical side lobes are observed for modes 2 and 3.

Figure 6.7(a) and (c) present a detailed three-dimensional view of the far-field patterns of mode 2 for $a_1 = 328$ nm at $\lambda = 960.2$ nm and of mode 3 for $a_1 = 328$ nm at $\lambda = 937.4$ nm, respectively. The x- and y- axes stand for the pixels of the CMOS sensor of the infrared camera. The z-axis shows the signal intensity of each pixel registered by 8 digital bits (value range from 0 to 255). The size of each pixel is 4.8 μm by 4.8 μm. As a comparison, Figure 6.7(b) and (d) depict the recorded far-field patterns when the laser is focused on a blank surface at the wavelength of (a) and (c), respectively.

We can clearly see that the pronounced center lobe (located at $x = y = 0$) is a result of the PCCs, as such a pronounced center lobe is missing at the same pixel position for the illuminated blank surface. Moreover, the signal intensity for illuminated PCCs is orders of magnitude stronger than for the illuminated blank surface, thanks to the cross-polarized configuration and thus the significantly suppressed excitation beam.

Figure 6.8 depicts 2D images of the far-field of the blank surface at three different wavelengths of (a) 937.4 nm, (b) 945.0 nm, and (c) 960.2 nm. The centrosymmetric intensity distribution is a result of the non-vanishing y-polarized component of the x-polarized excitation Gaussian beam, which features four lobes around the center point (Figure 2.11). Here, for the illuminated blank surface at 937.4 nm and 960.2 nm, we observe that two lobes in one of the diagonal directions are stronger than the other two. We

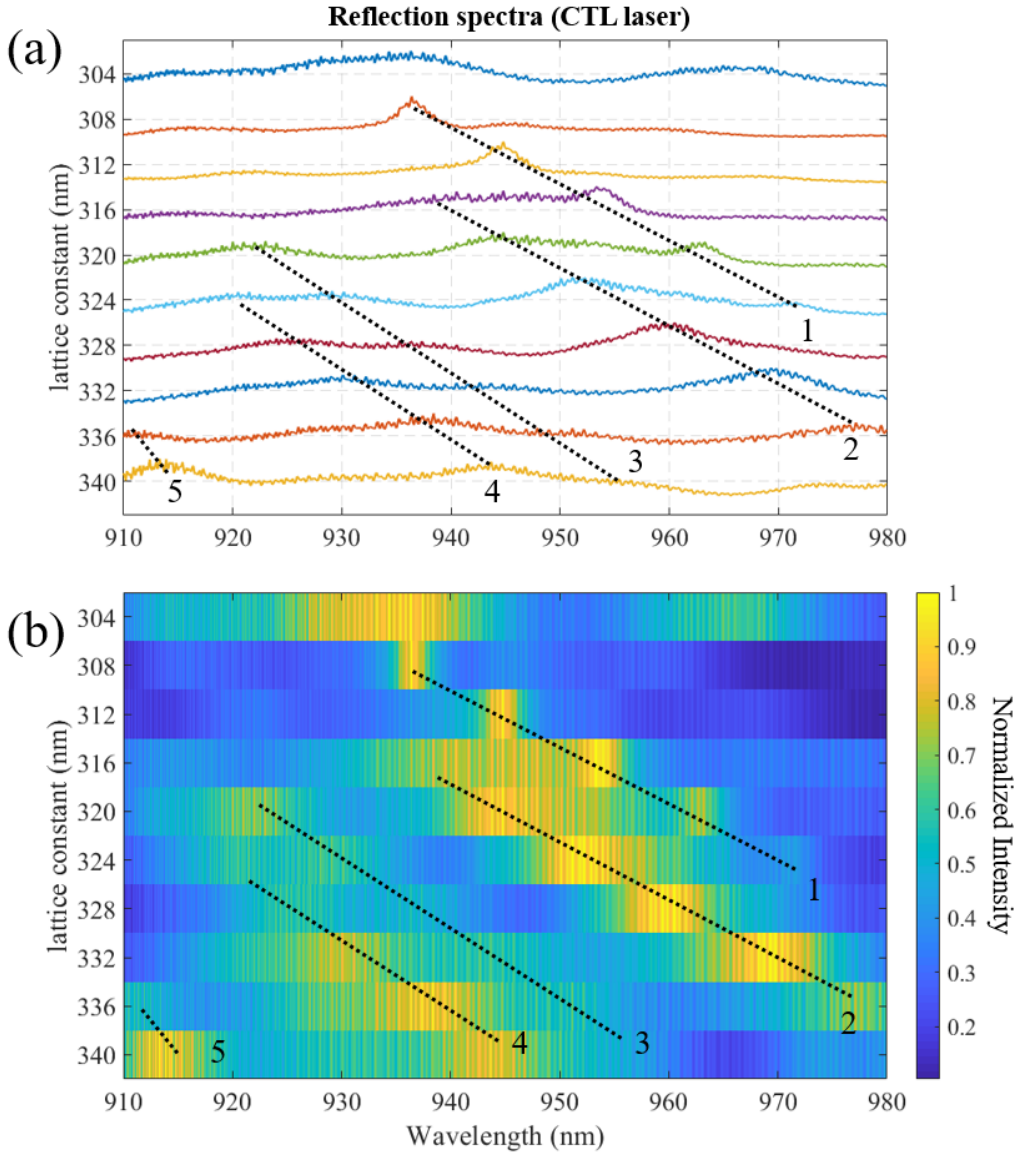

Figure 6.5: Reflection spectra of the 10 PCCs measured excited by the CTL laser from 910 nm to 980 nm. The lattice pitches are $a_1 = 304 : 4 : 340$ nm and hole radii $r_1 = 112 : 2 : 130$ nm from top to bottom. Families of resonant peaks are highlighted and labeled by numbers. (a) Normalized reflection spectra as a function of the wavelength and plotted for each PCC. (b) The same spectra plotted as a 2D image for better visualization.

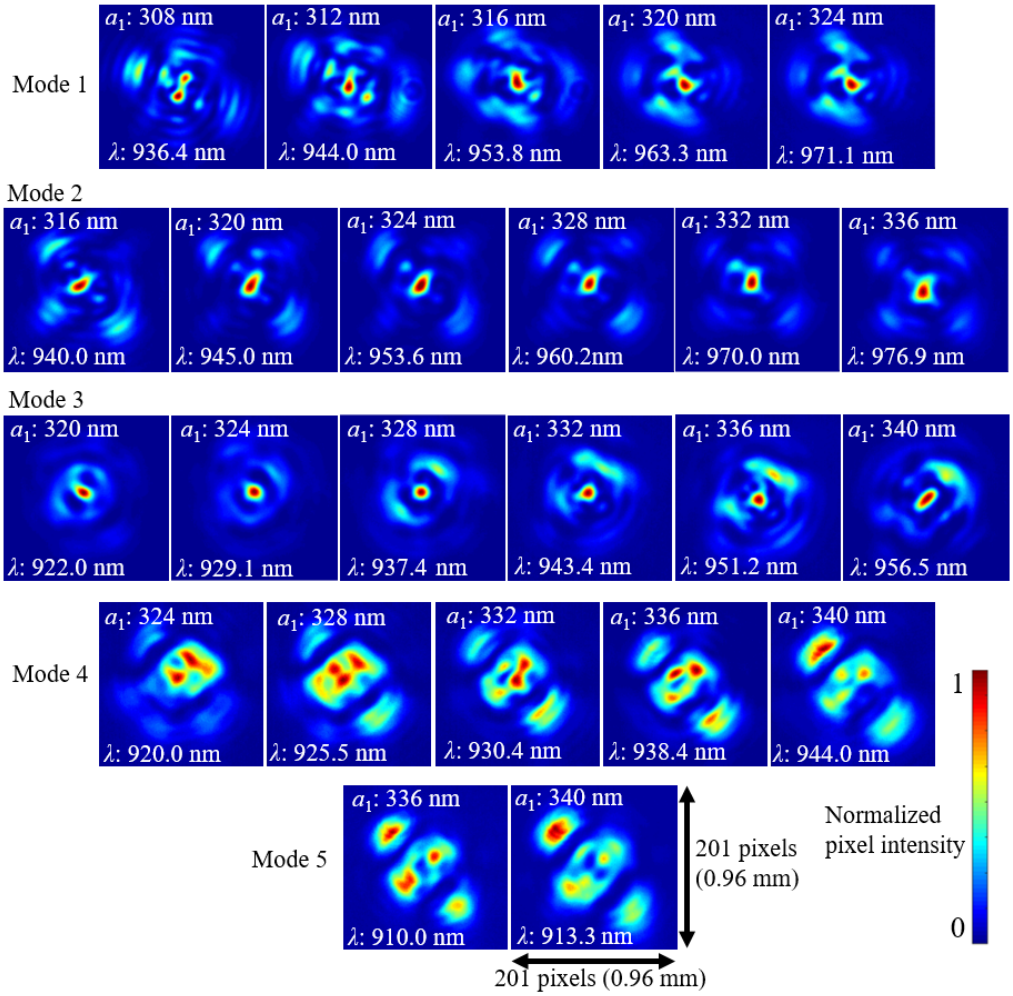

Figure 6.6: Far-field emission patterns for all five families of resonance peaks highlighted in Figure 6.5. All far-field patterns are independently normalized by their maximum values. The size of each figure is 201 by 201 pixels, which is equal to 0.96 mm by 0.96 mm. Concentrated and Gaussian-like far-field patterns are observed for modes 2 and 3.

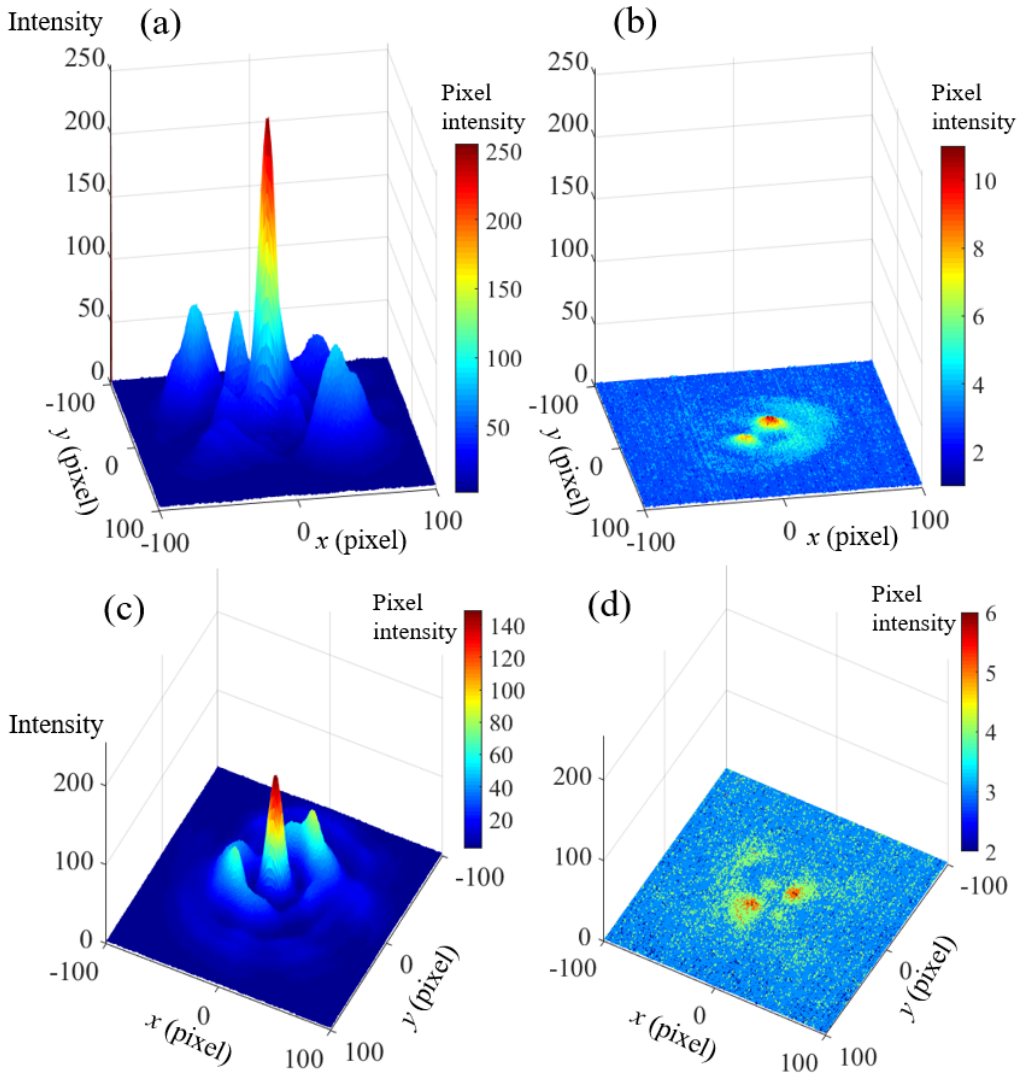

Figure 6.7: Three-dimensional view of far-field patterns. The size of each pixel is 4.8 μm by 4.8 μm. (a) Far-field of mode 2 for $a_1 = 328$ nm at $\lambda = 960.2$ nm, (b) Far-field of blank surface at $\lambda = 960.2$ nm, (c) Far-field of mode 3 for $a_1 = 328$ nm at $\lambda = 937.4$ nm, (d) Far-field of blank surface at $\lambda = 937.4$ nm.

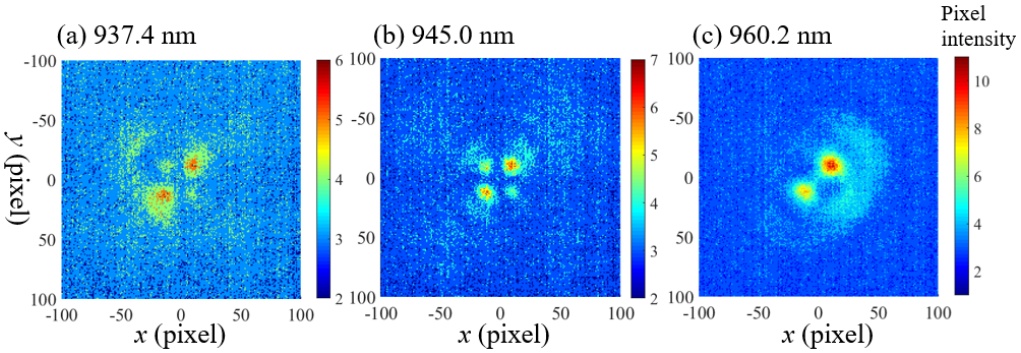

Figure 6.8: 2D images of the far-field of illuminated blank surface at (a) 937.4 nm, (b) 945.0 nm and (c) 960.2 nm. No pronounced central lobe is observed at the central location. Due to the non-ideal $\lambda/4$ plate, the far-field patterns at 937.4 nm and 960.2 nm are different from that of 945 nm, at which the $\lambda/4$ plate is aligned and optimized.

attribute this to the non-ideal $\lambda/4$ plate, which is optimized for $\lambda = 945$ nm in our experimental setup. At this optimized wavelength, the four side lobes are clearly visible (Figure 6.8(b)).

6.2.2 Gaussian fits

In this section, we quantitatively evaluate the recorded far-field patterns. Due to the absence of phase information in the recorded far-field, we are not able to calculate the full vectorial optical overlap $\mathrm{OV}(\theta)$ defined by equation 4.8 or the overall efficiency (see equation 4.9). As an alternative approach, we fit the recorded central lobe by a 2D Gaussian function and calculate the fraction of optical power in that central lobe. Thus, we evaluate the quality of the far-field based on the goodness of the fitting and the power inside the central lobe.

We fit the central lobes by a two-dimensional elliptical Gaussian function:

$$G(x, y) = A^2 \exp\left(-2\frac{x_{\mathrm{rot}}^2}{w_x^2} - 2\frac{y_{\mathrm{rot}}^2}{w_y^2}\right), \tag{6.1}$$

where the x_{rot} and y_{rot} are calculated by shifting and rotating the coordinate

system of the recorded image:

$$\begin{pmatrix} x_{\text{rot}} \\ y_{\text{rot}} \end{pmatrix} = \begin{pmatrix} \cos(\psi) & -\sin(\psi) \\ \sin(\psi) & \cos(\psi) \end{pmatrix} \begin{pmatrix} x - x_0 \\ y - y_0 \end{pmatrix}. \tag{6.2}$$

The Gaussian distribution defined by equation 6.1 and 6.2 has six fit parameters, which are the amplitude A, the $1/e^2$ radii w_x and w_y, which are the major and minor radii of the elliptical Gaussian distribution, the rotation angle ψ, and the central location x_0 and y_0.

The fit parameters are determined by minimizing the RMS (root-mean-square) value:

$$\text{RMS} = \frac{\sqrt{\frac{1}{N}\sum_i^N (D_i - G_i)^2}}{\sqrt{\frac{1}{N}\sum_i^N D_i^2}}, \tag{6.3}$$

where D_i and G_i stand for the pixel values of the recorded far-field (normalized to a range between 0 and 255) and the Gaussian function, respectively, and N is the total number of pixels. Since we are only interested in the central lobe, we restrict the fit area to 41 by 41 pixels (196.8 μm by 196.8 μm), with the central lobe placed in the center of the fit area. As an example, Figure 6.9(a) shows the fit area containing the central lobe of mode 3 with $a_1 = 324$ nm at $\lambda = 929.1$ nm, and Figure 6.9(b) displays the Gaussian fit with a minimized RMS value of 0.164.

Table 6.1 summarizes the fit parameters w_x/w_y, ψ and the minimized RMS values for all five mode families listed in Figure 6.6. We also calculate the mean RMS values for each mode family. As we can see, the mean RMS values for modes 2 and 3 are 0.215 and 0.234, respectively, which are significantly smaller than those of modes 1, 4, and 5. As a result, we conclude that the central lobes of modes 2 and 3 are more Gaussian-like compared to those of modes 1, 4, and 5.

In order to further evaluate the far-field patterns, we calculate the fraction of optical power inside an ellipse defined by the center location (x_0, y_0) with the major and minor radius (w_x, w_y) and rotated by the angle ψ. We define it as the fit efficiency η_{fit}. To maintain consistency, we use a typical $(w_{\text{typ},x}, w_{\text{typ},y}) = (64.1\,\mu\text{m}, 85.5\,\mu\text{m})$ and $\psi_{\text{typ}} = 51.9°$, obtained by fitting mode 3 with $a_1 = 324$ nm, to calculate the η_{fit} for all far-field

w_x/w_y (μm)	Mode 1	Mode 2	Mode 3	Mode 4	Mode 5
308 nm	236.8/55.2 $\psi = 70.3°$ RMS = 0.465	-	-	-	-
312 nm	138.7/60.9 $\psi = 79.8°$ RMS = 0.406	-	-	-	-
316 nm	70.9/116.2 $\psi = 25.8°$ RMS = 0.213	115.6/57.9 $\psi = 33.9°$ RMS = 0.236	-	-	-
320 nm	69.0/145.4 $\psi = 42.3°$ RMS = 0.331	113.4/62.9 $\psi = 62.3°$ RMS = 0.185	59.3/118.0 $\psi = 51.0°$ RMS = 0.280	-	-
324 nm	80.6/187.8 $\psi = 45.7°$ RMS = 0.274	109.0/60.7 $\psi = 54.9°$ RMS = 0.195	64.1/85.5 $\psi = 51.9°$ RMS = 0.164	288.9/178.9 $\psi = 29.1°$ RMS = 0.262	-
328 nm	-	108.7/67.4 $\psi = 58.7°$ RMS = 0.247	60.7/67.9 $\psi = 250.5°$ RMS = 0.228	631.9/228.1 $\psi = 38.9°$ RMS = 0.183	-
332 nm	-	103.0/71.2 $\psi = 88.2°$ RMS = 0.216	62.8/84.2 $\psi = 118.9°$ RMS = 0.257	685.9/137.8 $\psi = 66.8°$ RMS = 0.309	-
336 nm	-	110.3/86.9 $\psi = 78.6°$ RMS = 0.211	72.2/80.9 $\psi = -38.8°$ RMS = 0.314	2.92e6/238.0 $\psi = -138.5°$ RMS = 0.334	6.06e5/193.3 $\psi = -137.8°$ RMS = 0.375
340 nm	-	-	104.3/52.8 $\psi = 43.6°$ RMS = 0.163	197.4/9.14e4 $\psi = -49.1°$ RMS = 0.283	8.06e5/348.2 $\psi = -130.6°$ RMS = 0.380
Mean RMS	0.338	0.215	0.234	0.274	0.378

Table 6.1: Fit parameters w_x/w_y, ψ and the RMS values for all five mode families listed in Figure 6.6. The mean RMS values for modes 2 and 3 are smaller compared to modes 1, 4, and 5, indicating better Gaussian-like central lobes for modes 2 and 3.

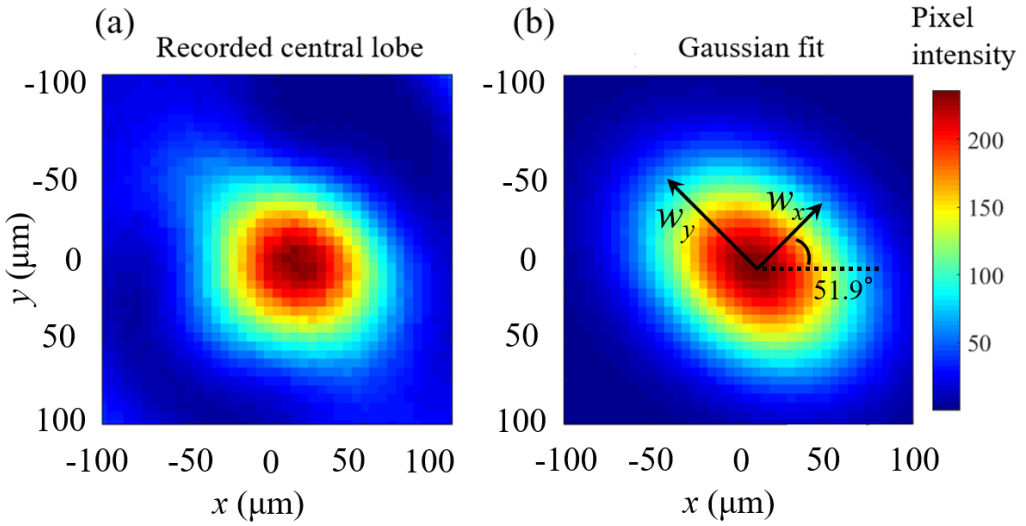

Figure 6.9: (a) The fit area showing the measured central lobe of the mode 3 with $a_1 = 324$ nm at $\lambda = 929.1$ nm. (b) The Gaussian fit with a minimized RMS = 0.164. The fitted $1/e^2$ radii are $(w_x, w_y) = (64.1\,\mu\text{m}, 85.5\,\mu\text{m})$ and the rotation angle is $\psi = 51.9°$.

patterns. We choose this far-field because of its smallest RMS value. On the other hand, the center location (x_0, y_0) is not fixed and is individually adapted to the fit values of different far-field patterns.

Mathematically, the fit efficiency η_{fit} calculated in this manner can be expressed as

$$\eta_{\text{fit}} = \frac{\iint_{S_{\text{fit}}} I(x,y)\,\mathrm{d}S}{\iint_{S_{\text{all}}} I(x,y)\,\mathrm{d}S}, \tag{6.4}$$

where S_{all} denotes the entire image surface, and $I(x, y)$ is the recorded field intensities which are represented by the pixel values. Finally, S_{fit} is the area inside the ellipse.

$$S_{\text{fit}} : \{\forall(x,y) : \frac{x^2_{\text{typ, rot}}}{w^2_{\text{typ},x}} + \frac{y^2_{\text{typ, rot}}}{w^2_{\text{typ},y}} \leq 1\}, \tag{6.5}$$

where the $x_{\text{typ, rot}}$ and $y_{\text{typ, rot}}$ are calculated according to equation 6.2 by using $\psi_{\text{typ}} = 51.9°$.

Table 6.2 summarizes the calculated η_{fit} for all 5 mode families and the average η_{fit} for each mode family. As we can see, mode 2 has the highest mean $\eta_{\text{fit}} = 14.6\%$ followed by mode 3 with a mean $\eta_{\text{fit}} = 11.1\%$. In

a_1 (nm)	308	312	316	320	324	328	332	336	340	Mean η_{fit}
Mode 1	9.1%	8.8%	11.0%	11.8%	9.0%	-	-	-	-	9.9%
Mode 2	-	-	10.3%	15.0%	15.5%	14.2%	16.3%	16.1%	-	14.6%
Mode 3	-	-	-	14.8%	14.1%	9.0%	9.2%	9.0%	10.3%	11.1%
Mode 4	-	-	-	-	9.2%	8.6%	8.6%	7.3%	4.9%	7.7%
Mode 5	-	-	-	-	-	-	-	4.6%	3.6%	4.1%

Table 6.2: Calculated η_{fit} for mode families 1 to 5. Fixed radii and rotation angle are used for all modes using a typical value: $(w_{\text{typ},x}, w_{\text{typ},y}) = (64.1\,\mu\text{m}, 85.5\,\mu\text{m})$ and $\psi_{\text{typ}} = 51.9°$, which are obtained by fitting mode 3 with $a_1 = 324$ nm.

contrast, the mean η_{fit}s for modes 1, 4, and 5 are all below 10%. Combined with the fact that modes 2 and 3 have the smallest mean RMS values, we conclude that these two modes have the better Gaussian center lobe and the higher efficiency. However, it is not clear whether or not these two modes correspond to the designed target mode, which should be at 873 nm for a_1 =304 nm and at 949 nm for a_1 =340 nm according to our simulations. To answer this question, we need more comprehensive measurement and simulation data.

6.2.3 Results with supercontinuum source

To obtain the reflection spectra over a broader wavelength range, we use the NKT supercontinuum source to compensate for the relatively narrow tuning range of the CTL laser. The wavelength of the NKT laser is tuned from 800 nm to 1000 nm with a step size of 0.2 nm. The recorded reflection spectra of all 10 measured PCCs are plotted in Figure 6.10. As we can see between 910 nm and 980 nm, the reflection spectra closely resemble those in Figure 6.5. However, due to the lower laser power and the larger laser linewidth, the mode families 1 to 4, which are clearly visible in Figure 6.5, are less distinct. For consistency, we use the same dashed lines to highlight modes 1 to 4.

On the other hand, mode 5 becomes clearly visible, and new mode families appear in the wavelength range between 800 nm and 910 nm. We

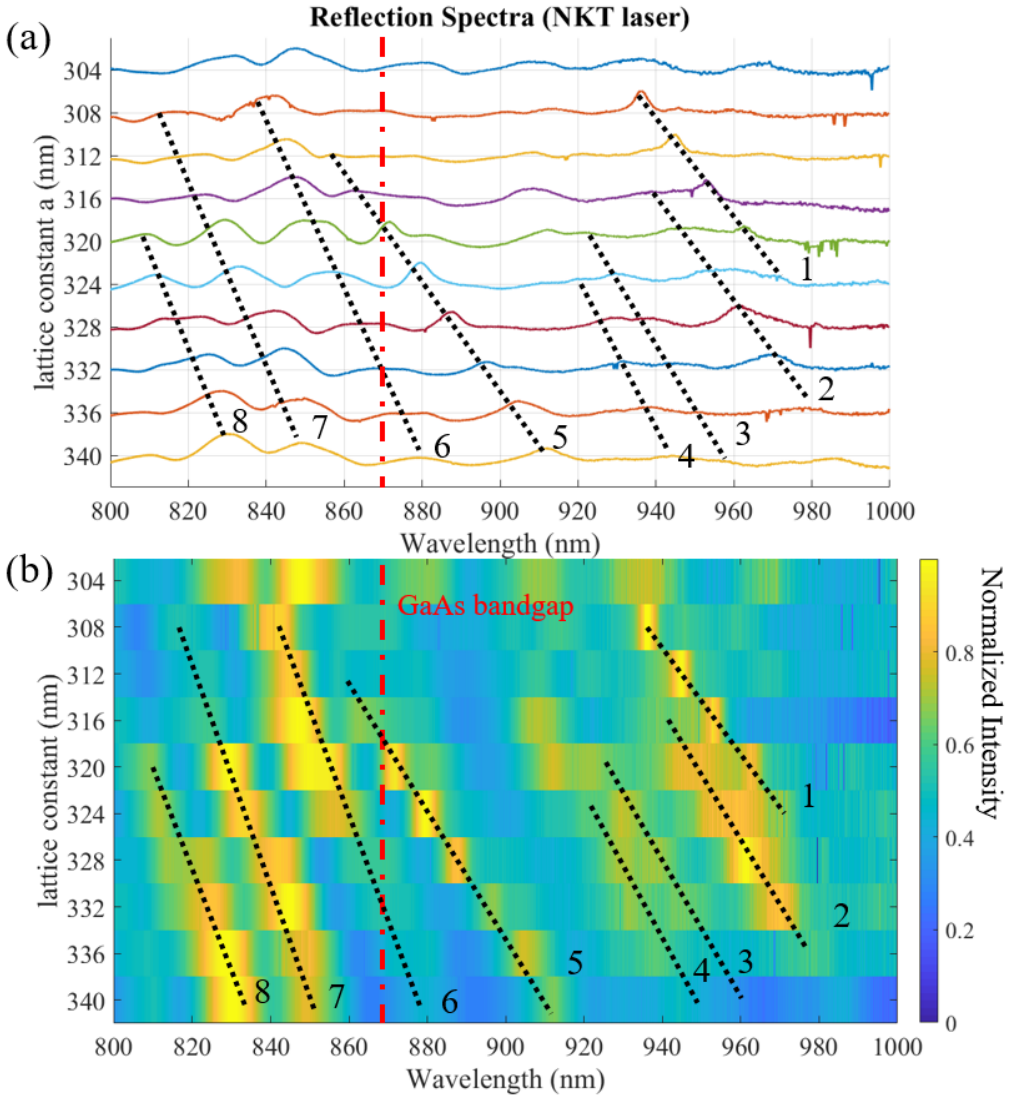

Figure 6.10: Reflection spectra (rebalanced) of the 10 PCCs excited by the NKT laser from 800 nm to 1000 nm. The lattice pitches are $a_1 = 304 : 4 : 340$ nm from top to bottom. Families of resonant peaks are highlighted by black dashed lines. The bandgap wavelength of GaAs is indicated by the red dotted line. (a) Normalized reflection spectra as a function of the wavelength. (b) The same spectra plotted as a 2D image.

label those mode families by mode 6 to mode 8. We notice that the widths of the resonant peaks are smaller for modes 1 to 5 than for those of modes 6 to 8. This difference arises from the bandgap wavelength of GaAs at room temperature, which is around 870 nm. As a result, modes 6 to 8 experience additional material absorption loss and thus have a lower quality factor compared to modes 1 to 5.

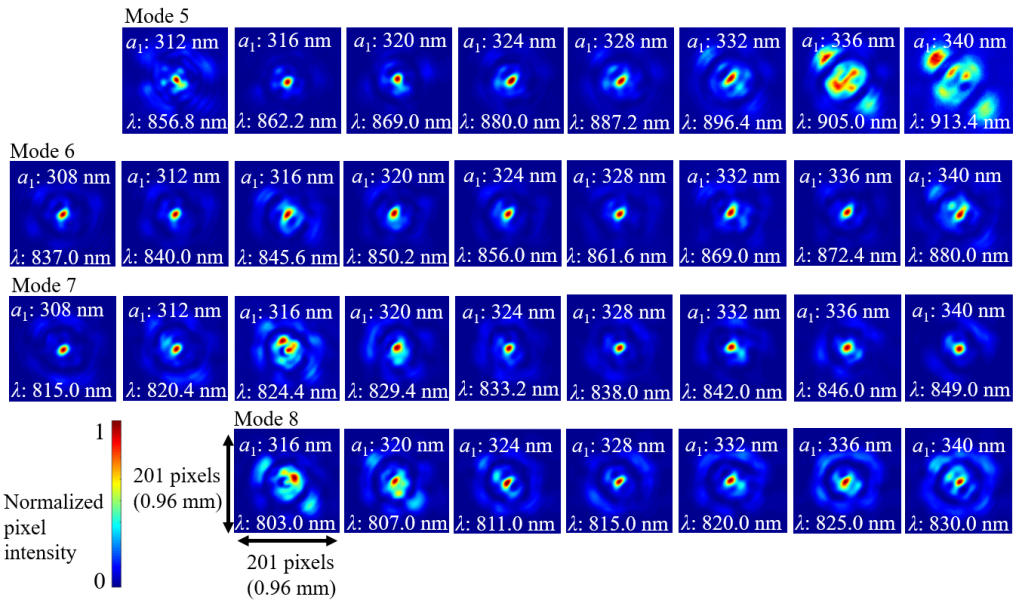

Figure 6.11: Far-field patterns for mode families 5 to 8 excited by the NKT laser. All far-field patterns are independently normalized by their maximum values. The size of each figure is 201 by 201 pixels, which is equal to 0.96 mm by 0.96 mm.

Figure 6.11 summarizes the recorded far-field patterns of modes 5 to 8, obtained using the NKT laser for excitation. Interestingly, we observe for all four mode families a pronounced central lobe, which is expected only for the designed target mode. A possible explanation is that they belong to the same Fabry-Pérot mode family as the target mode. In this case, their dominant field components are localized at similar positions and share similar distributions in k-space, differing only in their relative distances to the Γ point. As a result, the far-field patterns for these Fabry-Pérot modes are similar to that of the target mode, showing a pronounced central lobe.

However, according to our simulations, the free spectral range between Fabry-Pérot modes is around 70 nm, which is significantly larger than

the spectral spacing between the mode families 5 to 8, as observed in Figure 6.11(b). Further experimental investigation is required to answer this open question.

a_1(nm)	308	312	316	320	324	328	332	336	340	**Mean**
Mode 1	0.465	0.406	0.213	0.331	0.274	-	-	-	-	**0.338**
	9.3%	8.4%	9.7%	9.5%	7.0%					**8.8%**
Mode 2	-	-	0.236	0.185	0.195	0.247	0.216	0.211	-	**0.215**
			10.7%	15.2%	16.1%	14.1%	15.4%	15.3%		**14.5%**
Mode 3	-	-	-	0.280	0.164	0.228	0.257	0.314	0.163	**0.234**
				12.5%	12.8%	8.5%	9.2%	8.8%	10.8%	**10.4%**
Mode 4	-	-	-	-	0.262	0.183	0.309	0.334	0.283	**0.274**
					8.7%	8.0%	8.0%	6.8%	4.7%	**7.2%**
Mode 5	-	0.304	0.216	0.290	0.217	0.225	0.339	0.200	0.291	**0.260**
		6.8%	17.5%	16.0%	17.3%	12.5%	8.4%	6.5%	2.7%	**11.0%**
Mode 6	0.176	0.192	0.262	0.236	0.230	0.189	0.260	0.186	0.318	**0.228**
	15.3%	14.8%	12.5%	17.1%	15.9%	12.8%	10.9%	14.2%	8.4%	**13.5%**
Mode 7	0.153	0.326	0.312	0.242	0.277	0.186	0.316	0.207	0.223	**0.249**
	13.1%	10.6%	7.7%	15.2%	14.2%	13.6%	14.2%	15.8%	15.0%	**13.3%**
Mode 8	-	-	0.295	0.250	0.341	0.232	0.348	0.265	0.360	**0.299**
			7.3%	12.4%	12.9%	12.2%	12.3%	12.4%	8.9%	**11.2%**

Table 6.3: Calculated RMS values (black) and fit efficiencies (red) for modes 1 to 8. The far-field patterns are excited by the CTL laser for modes 1 to 4, and by the NKT laser for modes 5 to 8. To calculate the fit efficiencies, we use a typical parameter set for all modes: $(w_{\mathrm{typ},x}, w_{\mathrm{typ},y}) = (81.3\,\mu\mathrm{m}, 59.0\,\mu\mathrm{m})$ and $\psi_{\mathrm{typ}} = 39.9°$, which are fitting parameters of mode 7 at $a_1 = 308$ nm. We chose this mode because of its smallest RMS value among all far-field patterns.

Table 6.3 summarizes the RMS values and fit efficiencies for all the mode families. The RMS values are obtained by individually fitting the far-field patterns with the 2D Gaussian function (equations 6.1 and 6.2). The fit efficiencies are calculated using a typical parameter set, $((w_{\mathrm{typ},x}, w_{\mathrm{typ},y}) = (81.3\,\mu\mathrm{m}, 59.0\,\mu\mathrm{m})$ and $\psi_{\mathrm{typ}} = 39.9°)$, which are the fitting parameters of mode 7 at $a_1 = 308$ nm. We chose this mode because of its smallest RMS value. The mean RMS values and mean fit efficiencies are also calculated

for each mode family, shown in the last column.

As we can see, modes 2, 3, 6, and 7 have relatively low RMS values below 0.25. Among them, modes 2, 6, and 7 also show high fit efficiencies of 14.5%, 13.5%, and 13.3%, respectively. In contrast, modes 1, 4, 5, 8 have much larger RMS values and smaller fit efficiencies, indicating poor Gaussian-like emission profiles. Nevertheless, based on the current results, it is still unclear whether any of these mode families correspond to the designed target mode. This question will be the subject of future investigation.

6.3 Comparison to simulation results

Figure 6.12 shows the simulated reflection spectra obtained using the Lumerical FDTD package. In the simulation, the PCCs are illuminated by an x-polarized Gaussian beam, and the reflected electric field is projected to the far-field and recorded in the y-polarization. The parameters of the incident Gaussian beam are determined from measurements of the beam waist radius (or the divergence angle) of the real Gaussian beam used in the experimental setup.

As we can see in Figure 6.12, there are four distinct modes labeled by FP (Fabry-Pérot) mode 1 to 4, among which the FP mode 2 is the target mode. The spectral spacing between FP mode 1, 2, and 3 is around 70 nm. These three modes might belong to the same Fabry-Pérot mode family.

FP mode	mode 1	mode 2	mode 3	mode 4
Mean RMS	16.4	41.1	26.6	32.6
Mean η_{fit}	16.8%	11.7%	16.6%	19.0%

Table 6.4: Mean RMS values and fit efficiencies for the four FP modes in Figure 6.12.

Table 6.4 summarizes the calculated mean RMS values and fit efficiencies for all four FP modes. Interestingly, FP mode 2 (the target mode) has the largest mean RMS value and the lowest fit efficiency, indicating the least Gaussian-like emission among all four investigated modes. One possible explanation is that the target mode was originally identified using dipole excitation, as described in Chapter 4. Excitation by a Gaussian beam might

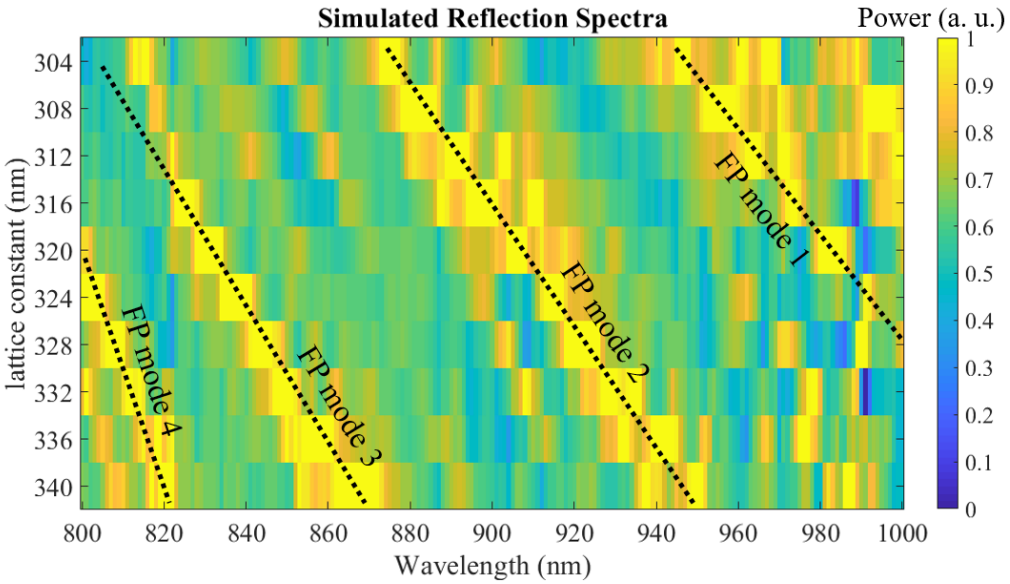

Figure 6.12: Simulated reflection spectra using the FDTD method. The cavities are illuminated by a Gaussian beam with parameters determined from the experimental setup. A cross-polarized configuration is considered in the simulation.

not correctly reproduce the characteristics of the target mode.

For a more concrete analysis, we repeated the simulation using a dipole source placed at the center of the PCCs. The relative angle between the symmetry axes of the PCC and the orientation of the dipole was fixed at 45° to maintain the cross-polarized configuration. The resulting cavity spectra are shown in Figure 6.13. Still, we are able to clearly distinguish the four FP modes from the background.

The mean RMS values and the fit efficiencies for dipole excitation are summarized in Table 6.5. In this case, we clearly see that the FP mode 2 representing the target mode has the highest mean fit efficiency of 49.5% and the smallest mean RMS value of 10.2, which is in agreement with the modeling results discussed in Chapter 4.

FP mode	mode 1	mode 2	mode 3	mode 4
Mean RMS	23.9	10.2	38.6	34.6
Mean η_{fit}	30.5%	49.5%	5.4%	32.2%

Table 6.5: Mean RMS values and fit efficiencies for the four FP modes in Figure 6.13.

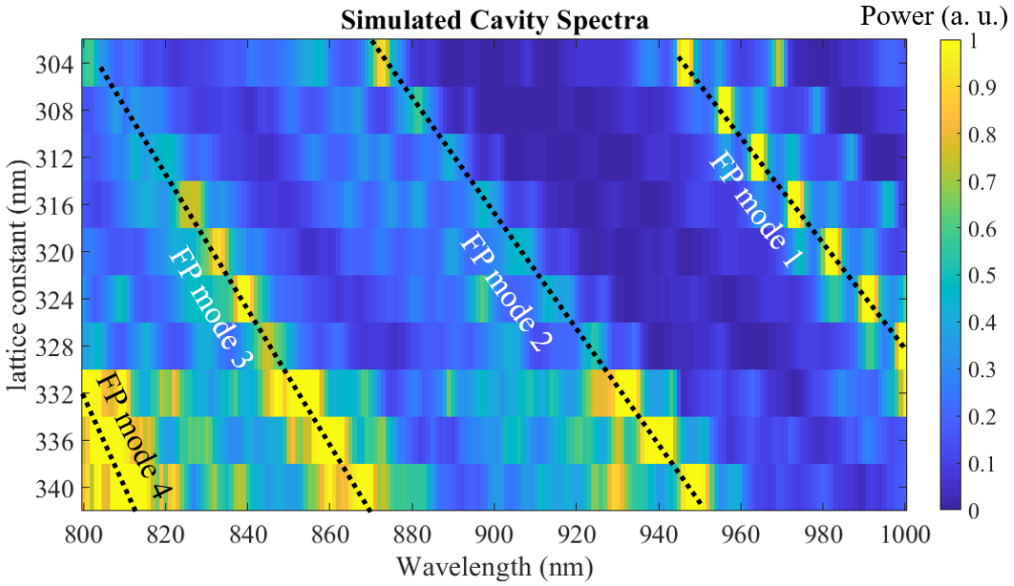

Figure 6.13: Simulated cavity spectra using the FDTD method. The cavities are excited by a dipole oriented 45° relative to the symmetry axes of the PCCs to maintain the cross-polarized configuration.

Based on these simulation results and the measurement results, we are unfortunately not able to clearly match the simulated FP modes to the measured mode families. In the measurement results, we observe more mode families with more complicated spectral shapes and far-field patterns than in the simulations. This discrepancy remains an open question and will require further investigation in the future.

6.4 Conclusion

In this chapter, we introduced the setup for cross-polarized room temperature reflection measurement and analyzed the resulting reflection spectra and far-field patterns for 10 investigated PCCS. The desired Gaussian-like far-field patterns were observed. Due to the absence of phase information, it was not possible to evaluate the full vectorial optical overlap. As an alternative, we fitted the central lobes of the far-field patterns by a 2D Gaussian function and extracted the RMS values and the fit efficiencies.

Although this alternative approach yields useful insight, the comparison between measurement and simulation results remains inconclusive. Further

experimental and theoretical investigations will be required to answer the remaining open questions and to establish a clearer correspondence between the observed mode families and the simulated Fabry-Pérot modes.

Chapter 7

Millikelvin Photoluminescence Measurements

In this chapter, we present the preliminary results of millikelvin photoluminescence (mK PL) measurements conducted at the Quantum Technology Group, Institute for Quantum Information in the RWTH Aachen University. The devices were fabricated by Sebastian Kindel. The measurements were carried out by Kui Wu, Sebastian Kindel, and Tobias Hangleiter.

7.1 Experimental setup

Figure 7.1 illustrates the measured sample and the corresponding electrical wiring of the device. A GaAs/$Al_{0.33}Ga_{0.67}As$ membrane chip is epoxy-bonded to a Si substrate and electrically connected to the external control electronic devices. The metal gates are patterned on both sides of the membrane. Purple wires are patterned on the topside connected to the top gates, while green wires are located on the backside connected to the bottom gates of the device. The PCC, the GDQD, and the OAQD are located in the center of the chip, as indicated by the red dashed circle in Figure 7.1(a). The $Al_{0.33}Ga_{0.67}As$ barriers are remotely doped by Si to induce a two-dimensional electron gas (2DEG) in the central GaAs quantum well layer.

Four gates are highlighted and labeled as BBT (Bottom Barrier Top), TBT (Top Barrier Top), TC (Top Central), and BC (Bottom Central). The labels are abbreviations of their locations and functionalities. The first T/B

indicates on which side of the membrane they are located. The last T means that it is on the top of the schematic figure. Voltage sweeps are applied to BBT, TBT, and BC, as will be discussed in the results section.

An SEM image showing the central part of the PCC with the metal gates is included in Figure 7.1(b). The nominal lattice constant of the PCC is the same as the values shown in Figure 3.5, while the hole radii are increased by 10 nm to compensate for fabrication deviations, because the radii of the etched holes are usually smaller than the E-beam written values by around 10 nm. As a result, the actual fabricated hole size is close to the design value.

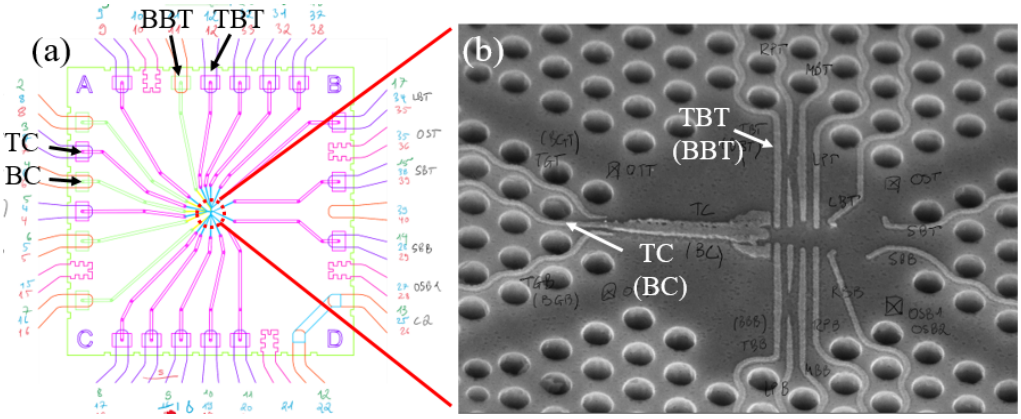

Figure 7.1: (a) The schematic overview of the electrically mounted chip. Purple wires are patterned on the top side, while green wires are on the bottom side of the GaAs/$Al_{0.33}Ga_{0.67}As$ membrane. (b) An SEM image of the central region of the chip showing the PCC, the OAQD, and the GDQD.

As we can see in Figure 7.1(b), the etched holes have a high quality with clean edges and smooth sidewalls. On the other hand, the metal gates are also well fabricated, with some slight imperfections including broken wires and residual E-beam resist on the wires connected to the OAQD.

The electrically connected chip is cooled down to millikelvin temperatures in a dilution refrigerator. A tunable continuous-wave Ti:sapphire laser is focused onto the membrane using an objective lens with a numerical aperture (NA) = 0.7. The PL signal is collected by the same lens and analyzed with a CCD spectrometer. The gates are biased with a voltage determined by the external control electronics, with the 2DEG in the center quantum well layer grounded. A detailed introduction to the utilized opto-mechanics is

available in Dr. Thomas Descamps' PhD thesis [75].

7.2 Results

The PL signal is recorded at different locations on the GaAs/$Al_{0.33}Ga_{0.67}As$ membrane under various gate voltages. The corresponding PL spectra are presented and discussed in this section.

7.2.1 Bare membrane

Figure 7.2(b) shows the PL spectrum of a bare heterostructure membrane. The measurement location is indicated in Figure 7.2(a), which is far from the central PCC and from any metal gates. No voltage is applied to the gates during the measurement.

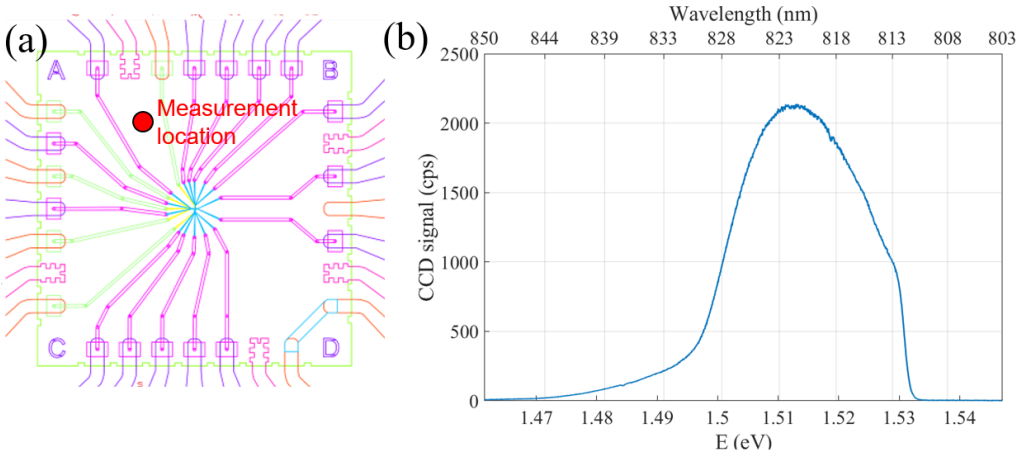

Figure 7.2: PL signal of the bare GaAs/$Al_{0.33}Ga_{0.67}As$ membrane. No bias voltage is applied to any gate. The excitation power is 5 μW at 795 nm. (a) Measurement location indicated by the red dot. (b) PL signal recorded by the spectrometer.

As we can see, the PL spectrum has a wide energy range from approximately 1.47 eV to 1.53 eV, which corresponds to a wavelength range from around 810 nm to 845 nm. Similar PL spectra recorded at cryogenic temperatures have been reported in Ref. [52, 80, 81]

On the high-energy side of the spectrum, we observe a steep drop at around 1.53 eV (810 nm). This is the Fermi edge of the 2DEG in the

quantum well [52, 80, 81]. Due to the extremely low temperature (mK range), an abrupt drop of the electron density appears at the Fermi energy level. Moreover, the PL rate at the Fermi edge is enhanced due to many-body processes [81], which make the Fermi edge more pronounced in the recorded spectrum.

The bandgap energy (wavelength) of bulk GaAs is 1.522 eV (814.6 nm) under 0 K according to Ref. [82]. We notice that the wavelength of the emission peak is around 822 nm in the spectrum, which is below the bandgap of bulk GaAs. The reason for this red-shifted bandgap energy might be the change of strain on the quantum well after substrate removal during the fabrication process [52, 83].

On the low-energy side between 1.47 eV and 1.49 eV, well below the exciton emission peak, we see a non-vanishing absorption tail with a reduced slope. This can be attributed to the Urbach tail due to localized states inside the bandgap created by disorders and dislocations [70].

Another possible explanation for the below-bandgap emission might be the exciton binding energy associated with the heavy hole. As reported in Ref. [84], this exciton binding energy is around 10 meV in GaAs quantum wells. Assuming a similar exciton binding energy and a bandgap energy of 1.522 eV in our case, the heavy hole emission wavelength is approximately 820 nm, which is close to the observed peak wavelength. However, this is only an assumption without considering other relevant physical effects such as the quantization energy due to the confinement in the perpendicular direction. According to Ref. [81], excitons do not exist in quantum wells with a high free electron density because of screening and phase-space occupation. So the assumption of bound excitons needs to be further verified and treated with caution.

7.2.2 Gated membrane

Figure 7.3(a) and (b) show the measurement location on the heterostructure and the recorded PL spectra as a function of energy for different voltages applied to the TBT gate. At this location, the width of the gates is sufficiently large to entirely cover the excitation laser spot. During the

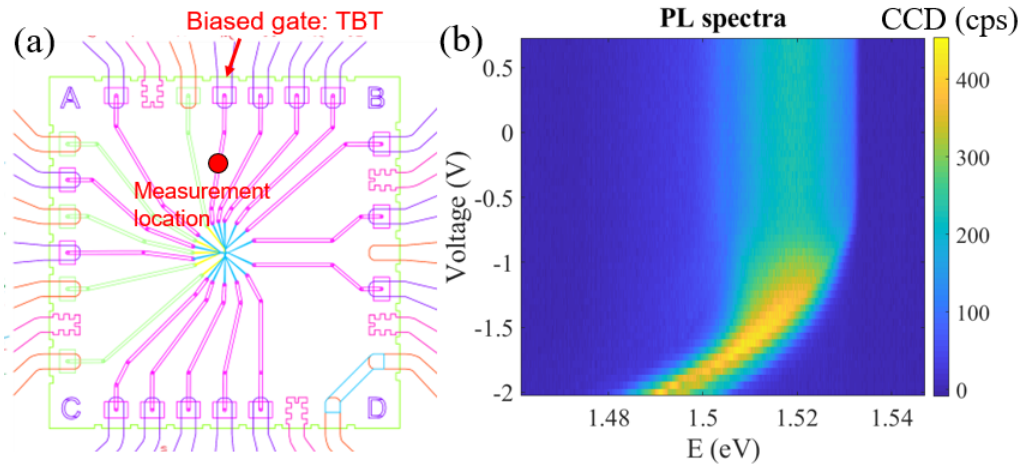

Figure 7.3: PL signal of the bare GaAs/$Al_{0.33}Ga_{0.67}As$ membrane with voltage sweep applied to the TBT gate. The excitation power is kept constant under 1 μW at 795 nm. (a) Measurement location indicated by the red dot. (b) 2D image plot of the PL signals for different gate voltages and photon energies.

voltage sweep, the 2DEG in the central quantum well layer is constantly grounded via Ohmic contacts.

As we can see, when the gate is negatively biased by more than 1 V, the PL emission shifts to lower energies (longer wavelengths) due to the quantum-confined Stark effect. This shift only occurs when the negative bias is large enough to deplete the 2DEG in the quantum well layer, which otherwise screens the external electric field [52].

Figure 7.4 summarizes the PL spectra from a similar measurement on top of the BBT gate, which is located on the bottom side of the membrane. We observe a similar Stark shift for negative biases larger than 1 V. However, in this case, the signal intensity is much weaker compared to Figure 7.3(b), as indicated by the color bars. The underlying reason might be the destructive interference caused by the BBT gate, which acts like a metal mirror and prohibits emission in the perpendicular direction. In other words, the destructive interference reduces the optical density of states in the quantum well layer and suppresses the spontaneous emission.

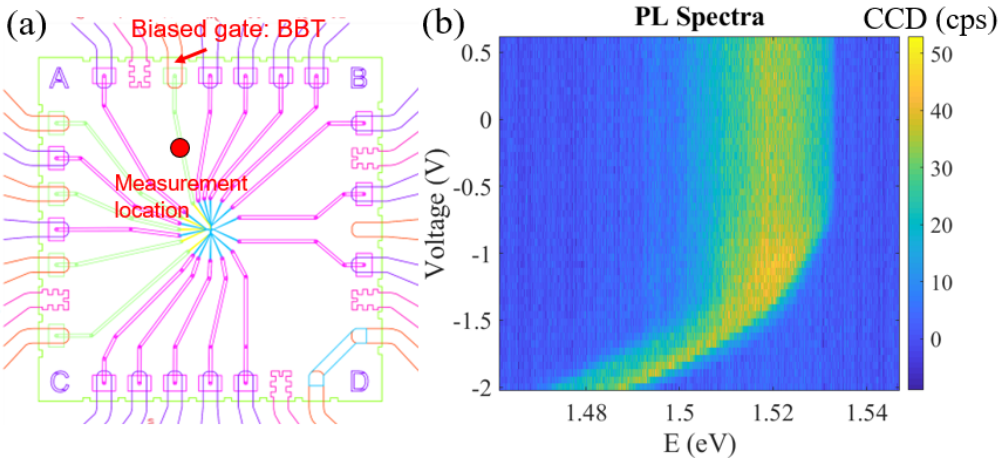

Figure 7.4: PL signal of the bare GaAs/$Al_{0.33}Ga_{0.67}As$ membrane with voltage sweep applied to the BBT gate. The excitation power is kept constant under 1 μW at 795 nm. (a) Measurement location indicated by the red dot. (b) 2D image plot of the PL signals for different gate voltages and photon energies.

7.2.3 Gated PCC

Figure 7.5 shows the PL spectra with the laser focused on the PCC in the center of the chip, as indicated in Figure 7.5(a). A voltage bias is applied to the BC gate and tuned between 0.5 V and -2 V in Figure 7.5(b), and between -1.5 V and -3 V in Figure 7.5(c) and (d).

In contrast to the spectra recorded on the bare heterostructure, we observe an additional peak at around 843 nm (1.475 eV) for voltage biases between -2 V and 0.5 V. Moreover, the intensity and energy of this peak decrease as the voltage bias is increased from -2 V to -3 V (Figure 7.5(c) and (d)).

There are two possible explanations for this peak. First, it can be one of the cavity modes of the PCC that enhances the spontaneous emission via the Purcell effect. Considering that the target mode is located at 823 nm according to the modeling results, the observed peak at 843 nm could be the target mode with a shifted wavelength due to fabrication uncertainties. The additional red shift for a large negative bias can be attributed to the quantum-confined Stark shift, and the reduced intensity is thus a result of the increased spectral mismatch between the cavity mode and the quantum well emission.

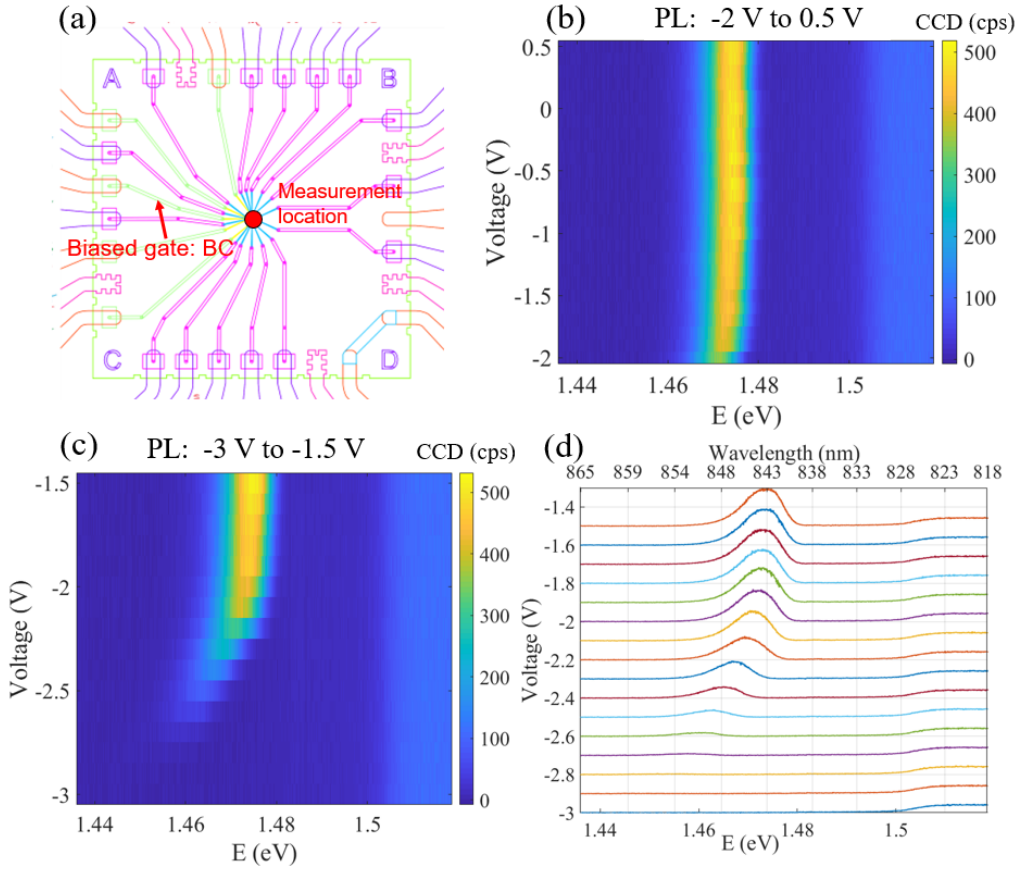

Figure 7.5: PL signals of the central gated PCC as a function of photon energy and gate bias. Voltage biases are applied to the BC gate. The excitation power is kept constant under 1 μW at 795 nm. (a) Schematic figure showing the measurement location and the biased gate BC. (b) PL spectra plotted as 2D image for voltage biases between -2 V and 0.5 V. (c) PL spectra plotted as 2D image for voltage biases between -3 V and -1.5 V. (d) Individual PL spectra for voltage biases between -3 V and -1.5 V.

Another possible explanation is the Fermi-level pinning of the etched holes caused by the surface charges trapped on the hole sidewalls. Those surface charges deplete the free electrons and accumulate free holes in their vicinity and bend the band diagram in the quantum well plane, resulting in a reduced effective bandgap. According to Ref. [85], the Fermi-level pinning is around 0.12 eV for a two-dimensional photonic crystal etched in n-doped InP. In our case, the energy difference is around 0.05 eV (from 816 nm to 843 nm), which is of the same order of magnitude as the literature value. In this case, the red shift for a large negative bias is caused by the Stark shift and the intensity reduction due to carrier depletion by the voltage bias. Further experimental investigation is required to distinguish between these two assumptions.

Figure 7.6 shows the results of photoluminescence excitation (PLE) measurement, in which the excitation wavelength and power are systematically swept. Figure 7.6(a) illustrates the PL spectra as a function of emitted photon energy (x-axis) and excitation wavelength (y-axis) under a constant excitation power of 5 μW. Figure 7.6(b) depicts the spectra recorded under different excitation powers up to 1 μW (y-axis) at a fixed excitation wavelength of 810 nm. The data in both figures are plotted on a logarithmic scale.

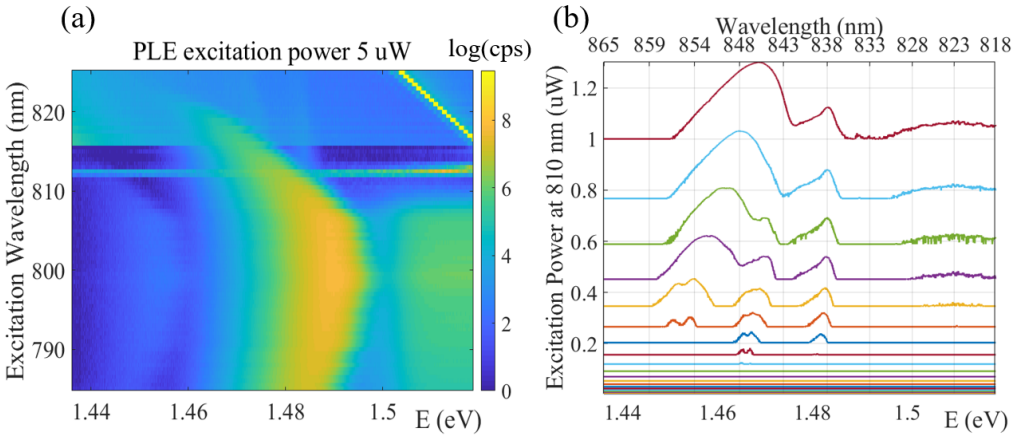

Figure 7.6: PLE measurement results on a logarithmic scale. (a) PL spectra plotted against photon energy and excitation wavelength under a constant excitation power of 5 μW. The excitation beam is also visible in the upper-right corner. (b) PL spectra for different excitation powers at a fixed wavelength of 810 nm

The first observation in Figure 7.6(a) is that the emission peak is blue-shifted to around 1.49 eV compared to 1.475 eV in Figure 7.5. The underlying reason is the increased excitation power from 1 μW to 5 μW, which generates more photo-excited electron-hole pairs and pushes the electron/hole Fermi energy to a larger value. As a result, the quantum well emission shifts to a higher energy range accordingly. A similar power-dependent blue shift is also observed in Figure 7.6(b).

On the other hand, we see multiple other peaks in Figure 7.6(a) and (b). These could be the different PCC cavity modes that require further experimental investigation. Another interesting observation is that the wavelength of the peak shifts in parallel with the excitation wavelength, as seen in Figure 7.6(a) for excitation wavelengths above 810 nm. The physical origin of this effect is still unclear and requires further investigation.

7.2.4 Bare PCCs on a different sample

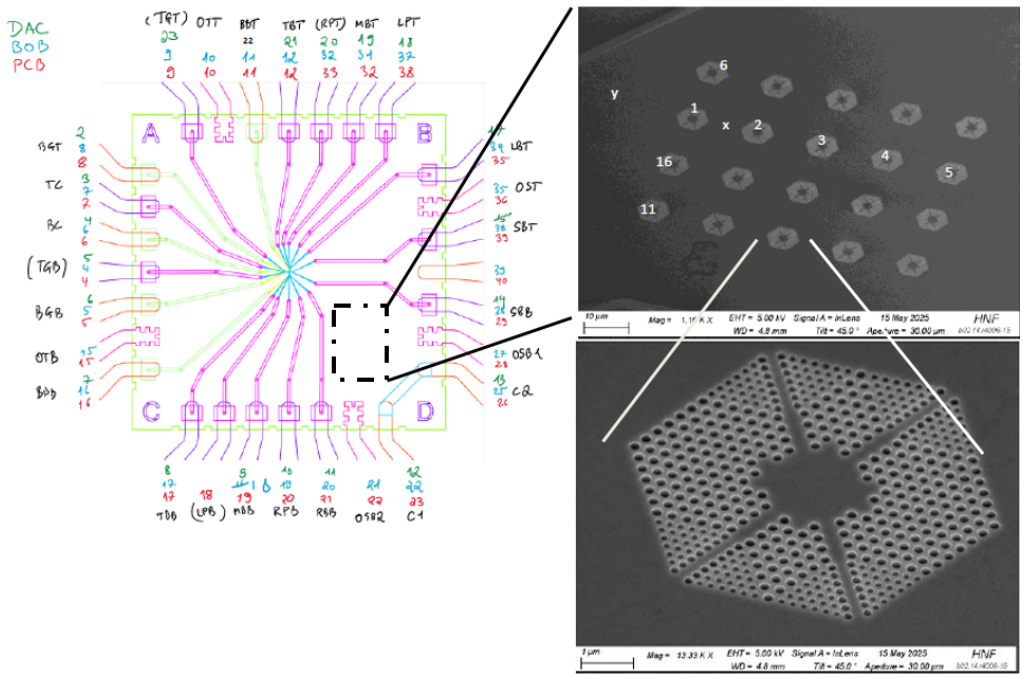

Figure 7.7: A different membrane chip with an array of 20 PCCs etched into the blank area. All 20 PCCs are nominally identical.

Figure 7.7 shows a schematic figure and two SEM images of a different

membrane chip. On this chip, an array of 20 PCCs is fabricated in the blank area of the chip away from any metal gates. All 20 PCCs are nominally identical and share the same design parameters as those described in Figure 3.5. The central gated PCC on this sample has unfortunately poor quality, with broken metal gates and significant residual E-beam resist. Consequently, no voltage bias could be applied to the central PCC during the measurement.

We recorded the PL spectra of all 20 PCCs. Figure 7.8 shows five representative spectra recorded on cavities labeled 1, 4, 7, 8, and 10. All five spectra feature a local maximum at around 818 nm, which is absent in the PL signal of the bare heterostructure membrane. The wavelength of this peak is also close to the wavelength of the target mode at 823 nm according to the modeling results. There is a good chance that the observed peak is the desired target mode. Nevertheless, further experimental verification is necessary to confirm this assumption.

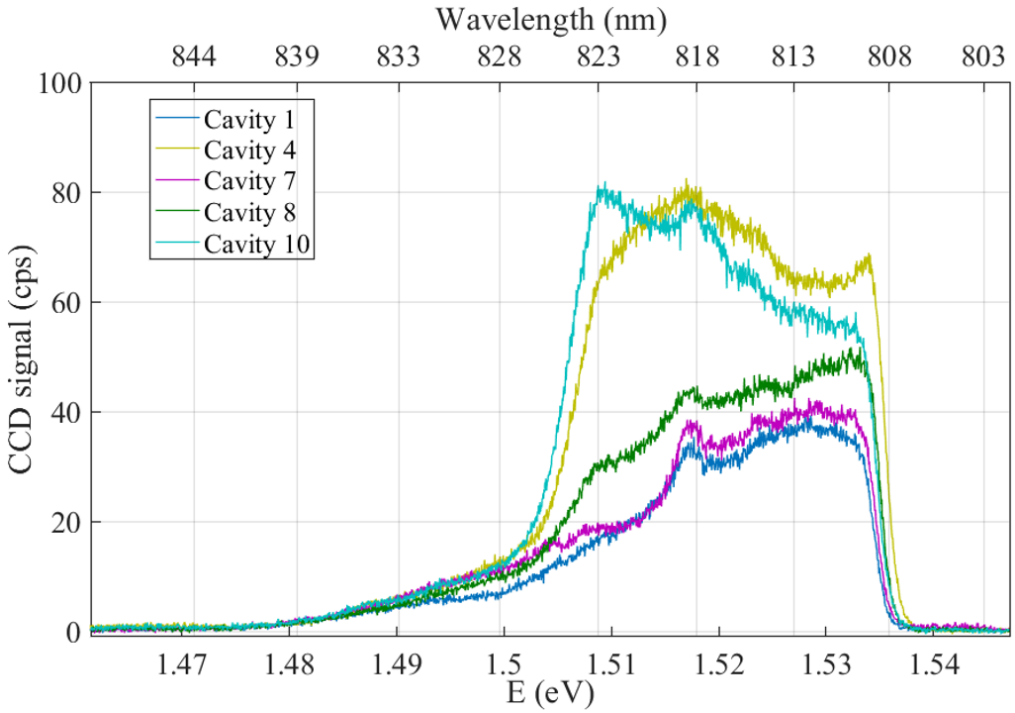

Figure 7.8: PL spectra of five PCCs from the array. All five spectra feature a local maximum near 818 nm, which may correspond to the target mode predicted by simulations.

We also notice that the unexpected signal peak observed in Figure 7.5 at around 843 nm is absent in Figure 7.8. The underlying reason remains unclear, but it may be related to the presence of metal gates or to differences in the fabrication quality of the two chips.

7.3 Conclusion

In this chapter, we introduced the experimental setup for millikelvin photoluminescence measurements and presented preliminary results showing promising potential. From the measurements on a bare heterostructure membrane, we reproduced the typical PL spectrum reported in the literature, confirming both the reliability of our setup and the quality of the sample. For the gated membrane, quantum-confined Stark shift is observed as expected. For the PCC with metal gates, we detected an unexpected signal peak, which requires further experimental investigation. Finally, for PCCs without metal gates, we noticed a local maximum at 818 nm in 5 out of 20 cavities, which may correspond to the predicted target mode.

Chapter 8

Summary and Outlook

In this thesis, we presented and analyzed an efficient optical interface between a singlet-triplet spin qubit and a photonic qubit. The optical interface integrates a gate system (the GDQD, the OAQD, the quantum dot charge sensor) with a photonic crystal cavity based on a modified H4 cavity with carefully engineered cavity openings. The entire structure can be fully lithographically defined and deterministically fabricated, which greatly increases the scalability of on-chip integration.

The photonic crystal cavity is designed such that the dominant wave vectors of the cavity mode at the working wavelength of the OAQD coincide with the reciprocal lattice vectors of the photonic crystal. As a result of strong Bragg scattering, we obtain enhanced vertical emission with a pronounced central lobe. The carefully designed cavity openings enable a continuous two-dimensional electron gas, which is otherwise depleted by the surface charges on the hole sidewalls, in the quantum well layer to support the functionality of the quantum dot charge sensor. In the meantime, thanks to the mini-stopband of the cavity openings, in-plane optical confinement is preserved.

According to our modeling results presented in Chapter 4, our design reaches a radiation efficiency of 54.7% and an optical overlap of 0.526 with a narrow Gaussian beam compatible with low-numerical-aperture collection optics. As a result, we expect an overall efficiency of 28.7%. The performance can be further increased by undercutting the SiO_2 interlayer between the semiconductor membrane and the gold reflector. In this case, the overall

efficiency is estimated to be 48.5% with an optical overlap equal to 0.839 and a radiation efficiency of 57.8%.

The desired Gaussian-like far-field patterns are confirmed by cross-polarized reflection measurements under room temperature, as discussed in Chapter 6. The recorded reflection spectra of 10 probed photonic crystal cavities show systematic variations with lattice pitch.

Preliminary results of millikelvin photoluminescence measurements also demonstrate promising potential. The typical photoluminescence spectrum of a bare heterostructure membrane and the expected quantum-confined Stark shift on a gated membrane are successfully reproduced. For photonic crystal cavities with metal gates, we recorded an unexpected signal peak that requires further experimental investigation. For bare photonic crystal cavities, we identified an enhanced emission peak close to the target wavelength. These preliminary but promising results provide strong motivation for further experimental investigation in the future.

Literature

[1] C. H. Bennett et al. “Quantum cryptography: Public key distribution and coin tossing.” In: *Theoretical Computer Science* 560 (2014), pp. 7–11.

[2] W. Wootters et al. “A single quantum cannot be cloned.” In: *Nature* 299 (1982), pp. 802–803.

[3] P. W. Shor. “Algorithms for quantum computation: discrete logarithms and factoring.” In: *Proceedings 35th Annual Symposium on Foundations of Computer Science*. 1994, pp. 124–134.

[4] D. P. DiVincenzo. “The Physical Implementation of Quantum Computation.” In: *Fortschritte der Physik* 48.9-11 (2000), pp. 771–783.

[5] D. P. DiVincenzo. “Quantum gates and circuits.” In: *Proc. R. Soc. Lond. A.* 454 (1998), pp. 261–276.

[6] D. P. DiVincenzo. “Quantum Computation.” In: *Science* 270.5234 (1995), pp. 255–261.

[7] N. P. de Leon et al. “Materials challenges and opportunities for quantum computing hardware.” In: *Science* 372.6539 (2021), eabb2823.

[8] D. Loss et al. “Quantum computation with quantum dots.” In: *Phys. Rev. A* 57 (1998), p. 120.

[9] J. Levy. “Universal Quantum Computation with Spin-1/2 Pairs and Heisenberg Exchange.” In: *Phys. Rev. Lett.* 89 (14 2002), p. 147902.

[10] J. R. Petta et al. “Coherent Manipulation of Coupled Electron Spins in Semiconductor Quantum Dots.” In: *Science* 309.5744 (2005), pp. 2180–2184.

[11] A. Shields. “Semiconductor quantum light sources.” In: *Nature Photon.* 1 (2007), pp. 215–223.

[12] D. Bimberg et al. *Quantum Dot Heterostructures*. Wiley, 1999.

[13] P. Michler et al. “A Quantum Dot Single-Photon Turnstile Device.” In: *Science* 290.5500 (2000), pp. 2282–2285.

[14] R. Hanson et al. “Spins in few-electron quantum dots.” In: *Rev. Mod. Phys.* 79 (2007), p. 1217.

[15] L. P. Kouwenhoven et al. “Electron transport in quantum dots.” In: *Mesoscopic Electron Transport*. Ed. by L. P. Kouwenhoven et al. Vol. 345. NATO ASI Series E: Applied Sciences. Springer, 1997, pp. 105–214.

[16] M. W. Doherty et al. “The nitrogen-vacancy colour centre in diamond.” In: *Physics Reports* 528.1 (2013), pp. 1–45.

[17] I. Aharonovich et al. “Solid-state single-photon emitters.” In: *Nature Photonics* 10 (2016), pp. 631–641.

[18] T. E. Roth et al. “An Introduction to the Transmon Qubit for Electromagnetic Engineers.” In: *IEEE Antennas Propag. Mag.* 65 (2023), pp. 8–20.

[19] J. Clarke et al. “Superconducting quantum bits.” In: *Nature* 453 (2008), pp. 1031–1042.

[20] M. Kjaergaard et al. “Superconducting Qubits: Current State of Play.” In: *Annual Review of Condensed Matter Physics* 11 (2020), pp. 369–395.

[21] D. J. Wineland et al. “Experimental Issues in Coherent Quantum-State Manipulation of Trapped Atomic Ions.” In: *Journal of Research of the National Institute of Standards and Technology* 103 (1998), p. 259.

[22] H.-J. Briegel et al. “Quantum repeaters: The role of imperfect local operations in quantum communication.” In: *Physical Review Letters* 81.26 (1998), pp. 5932–5935.

[23] N. Akopian et al. “Entangled photon pairs from semiconductor quantum dots.” In: *Physical Review Letters* 96.13 (2006), p. 130501.

[24] E. M. Purcell. “Spontaneous emission probabilities at radio frequencies.” In: *Physical Review* 69 (1946), p. 681.

[25] D. Englund et al. “Controlling the Spontaneous Emission Rate of Single Quantum Dots in a Two-Dimensional Photonic Crystal.” In: *Phys. Rev. Lett.* 95 (2005), p. 013904.

[26] T. Yoshie et al. “Vacuum Rabi splitting with a single quantum dot in a photonic crystal nanocavity.” In: *Nature* 432 (2004), pp. 200–203.

[27] J. Claudon et al. “A highly efficient single-photon source based on a quantum dot in a photonic nanowire.” In: *Nature Photonics* 4 (2010), pp. 174–177.

[28] S. Reitzenstein et al. “AlAs/GaAs micropillar cavities with quality factors exceeding 150.000.” In: *Applied Physics Letters* 90.25 (2007), p. 251109.

[29] X. Ding et al. “On-Demand Single Photons with High Extraction Efficiency and Near-Unity Indistinguishability from a Resonantly Driven Quantum Dot in a Micropillar.” In: *Phys. Rev. Lett.* 116 (2 2016), p. 020401.

[30] R. W. Andrews et al. “Bidirectional and efficient conversion between microwave and optical light.” In: *Nature Phys* 10 (2014), pp. 321–326.

[31] M. Bayer et al. “Electron and Hole g Factors and Exchange Interaction from Studies of the Exciton Fine Structure in $In_{0.60}Ga_{0.40}As$ Quantum Dots.” In: *Phys. Rev. Lett.* 82 (8 1999), pp. 1748–1751.

[32] H. Kosaka et al. “Coherent Transfer of Light Polarization to Electron Spins in a Semiconductor.” In: *Phys. Rev. Lett.* 100 (9 2008), p. 096602.

[33] M. Kuwahara et al. “Single charge detection of an electron created by a photon in a g-factor engineered quantum dot.” In: *Appl. Phys. Lett.* 96 (16 2010), p. 163107.

[34] H. Kosaka. “Photon-to-electron quantum information transfer.” In: *J. Appl. Phys.* 109 (10 2011), p. 102414.

[35] B. Joecker et al. “Transfer of a quantum state from a photonic qubit to a gate-defined quantum dot.” In: *Phys. Rev. B* 99 (20 2019), p. 205415.

[36] P. Lodahl et al. “Interfacing single photons and single quantum dots with photonic nanostructures.” In: *Rev. Mod. Phys.* 87 (2 2015), pp. 347–400.

[37] S. Strauf et al. “High-frequency single-photon source with polarization control.” In: *Nature Photon.* 1 (2007), pp. 704–708.

[38] M. Gschrey et al. “Highly indistinguishable photons from deterministic quantum-dot microlenses utilizing three-dimensional in situ electron-beam lithography.” In: *Nat. Commun.* 6 (2015), p. 7662.

[39] K. Xiong et al. “Efficient generation of single photons by quantum dots embedded in bullseye cavities with backside dielectric mirrors.” In: *Opt. Express* 31.12 (2023), pp. 19536–19543.

[40] R. Hekmati et al. “Bullseye dielectric cavities for photon collection from a surface-mounted quantum-light-emitter.” In: *Sci. Rep.* 13 (2023), p. 5316.

[41] K. Wu et al. “Modeling an efficient singlet-triplet-spin-qubit-to-photon interface assisted by a photonic crystal cavity.” In: *Phys. Rev. Appl.* 21 (5 2024), p. 054052.

[42] K. Wu et al. “High-efficiency gate-defined quantum dot to single mode fiber interface assisted by a photonic crystal cavity.” In: *AIP Advances* 10 (11 2020), p. 115016.

[43] L. V. H. Rodgers et al. “Materials challenges for quantum technologies based on color centers in diamond.” In: *MRS Bulletin* 46 (2021), pp. 623–633.

[44] J. M. Moison et al. “Self-organized growth of regular nanometer-scale InAs dots on GaAs.” In: *Applied Physics Letters* 64.2 (Jan. 1994), pp. 196–198.

[45] P. Cerfontaine et al. “High-Fidelity Single-Qubit Gates for Two-Electron Spin Qubits in GaAs.” In: *Phys. Rev. Lett.* 113 (15 2014), p. 150501.

[46] P. Cerfontaine et al. “Closed-loop control of a GaAs-based singlet-triplet spin qubit with 99.5% gate fidelity and low leakage.” In: *Nature Communications* 11.1 (2020), p. 4144.

[47] J. M. Elzerman et al. “Few-electron quantum dot circuit with integrated charge read out.” In: *Phys. Rev. B* 67 (16 2003), p. 161308.

[48] J. Elzerman et al. “Single-shot read-out of an individual electron spin in a quantum dot.” In: *Nature* 430 (2004), pp. 431–435.

[49] H. Bluhm et al. “Dephasing time of GaAs electron-spin qubits coupled to a nuclear bath exceeding 200 μs.” In: *Nature Physics* 7 (2011), pp. 109–113.

[50] E. Chekhovich et al. “Nuclear spin effects in semiconductor quantum dots.” In: *Nature Materials* 12 (2013), pp. 494–504.

[51] J. Yoneda et al. “A quantum-dot spin qubit with coherence limited by charge noise and fidelity higher than 99.9%.” In: *Nature Nanotechnology* 13 (2018), pp. 102–106.

[52] T. Descamps et al. “Semiconductor Membranes for Electrostatic Exciton Trapping in Optically Addressable Quantum Transport Devices.” In: *Phys. Rev. Appl.* 19 (4 2023), p. 044095.

[53] H. Bluhm et al. *Electrons in Solids: Mesoscopics, Photonics, Quantum Computing, Correlations, Topology*. Graduate Texts in Condensed Matter. Berlin, Boston: De Gruyter, 2019.

[54] G. Burkard et al. “Semiconductor spin qubits.” In: *Reviews of Modern Physics* 95.2 (2023), p. 025003.

[55] C. Barthel et al. “Fast sensing of double-dot charge arrangement and spin state with a radio-frequency sensor quantum dot.” In: *Phys. Rev. B* 81 (16 2010), p. 161308.

[56] C. Barthel et al. “Interlaced Dynamical Decoupling and Coherent Operation of a Singlet-Triplet Qubit.” In: *Phys. Rev. Lett.* 105 (26 2010), p. 266808.

[57] M. Bayer et al. “Fine structure of neutral and charged excitons in self-assembled In(Ga)As/(Al)GaAs quantum dots.” In: *Phys. Rev. B* 65 (19 2002), p. 195315.

[58] E. Yablonovitch. “Inhibited Spontaneous Emission in Solid-State Physics and Electronics.” In: *Phys. Rev. Lett.* 58 (20 1987), pp. 2059–2062.

[59] S. John. “Strong localization of photons in certain disordered dielectric superlattices.” In: *Phys. Rev. Lett.* 58 (23 1987), pp. 2486–2489.

[60] J. D. Joannopoulos et al. *Photonic Crystals: Molding the Flow of Light*. 2nd. Princeton, NJ: Princeton University Press, 2008.

[61] Y. Akahane et al. “High-Q photonic nanocavity in a two-dimensional photonic crystal.” In: *Nature* 425.6961 (2003), pp. 944–947.

[62] Y. Akahane et al. “Fine-tuned high-Q photonic-crystal nanocavity.” In: *Opt. Express* 13.4 (2005), pp. 1202–1214.

[63] J. W. Goodman. *Introduction to Fourier Optics*. 4th. Macmillan Learning / W. H. Freeman, 2017.

[64] U. Levy et al. “Weakly diverging to tightly focused Gaussian beams: a single set of analytic expressions.” In: *Journal of the Optical Society of America A* 33.10 (2016), pp. 1999–2004.

[65] U. Levy et al. “Weakly diverging to tightly focused Gaussian beams: a single set of analytic expressions: continuation—symmetric beams.” In: *Journal of the Optical Society of America A* 34.3 (2017), pp. 331–335.

[66] S. Olivier et al. “Coupled-mode theory and propagation losses in photonic crystal waveguides.” In: *Optics Express* 11.13 (2003), pp. 1490–1496.

[67] J.-P. Berenger. “A perfectly matched layer for the absorption of electromagnetic waves.” In: *Journal of Computational Physics* 114.2 (1994), pp. 185–200.

[68] L. Novotny et al. *Principles of Nano-Optics*. Cambridge University Press, 2006.

[69] S. A. Lourenço et al. “Temperature dependence of optical transitions in AlGaAs.” In: *Journal of Applied Physics* 89.11 (June 2001), pp. 6159–6164.

[70] A. V. Lehmen et al. “Investigation of Urbach tail absorption in GaAs quantum wells by two-wavelength modulation spectroscopy.” In: *International Quantum Electronics Conference*. Optica Publishing Group, 1986, MGG6.

[71] J. Talghader et al. “Thermal dependence of the refractive index of GaAs and AlAs measured using semiconductor multilayer optical cavities.” In: *Applied Physics Letters* 66.3 (Jan. 1995), pp. 335–337.

[72] M. Bertolotti et al. “Temperature dependence of the refractive index in semiconductors.” In: *J. Opt. Soc. Am. B* 7.6 (1990), pp. 918–922.

[73] S. Romero-García et al. “Alignment Tolerant Couplers for Silicon Photonics.” In: *IEEE Journal of Selected Topics in Quantum Electronics* 21.6 (2015), pp. 765–778.

[74] Y. Tanaka et al. “Investigation of point-defect cavity formed in two-dimensional photonic crystal slab with one-sided dielectric cladding.” In: *Applied Physics Letters* 88.1 (Jan. 2006), p. 011112.

[75] T. Descamps. “Electrostatic exciton trap in a thin semiconductor membrane for optical coupling to a GaAs spin qubit.” PhD thesis. Aachen, Germany: RWTH Aachen University, 2021.

[76] K. Wu et al. “Highly efficient spin qubit to photon interface assisted by a photonic crystal cavity.” In: *Physics and Simulation of Optoelectronic Devices XXX*. Vol. 11995. Proceedings of SPIE. 2022, p. 1199507.

[77] H. Tamura et al. “GaAs and GaAlAs Reactive Ion Etching in BCl3-Cl2 Mixture.” In: *Japanese Journal of Applied Physics* 23.9A (1984), p. L731.

[78] A. V. Kuhlmann et al. “A dark-field microscope for background-free detection of resonance fluorescence from single semiconductor quantum dots operating in a set-and-forget mode.” In: *Review of Scientific Instruments* 84.7 (July 2013), p. 073905.

[79] W. C. Stumpf et al. “Reflectance measurement of two-dimensional photonic crystal nanocavities with embedded quantum dots.” In: *Phys. Rev. B* 82 (7 2010), p. 075119.

[80] D. Kamburov et al. “Use of micro-photoluminescence as a contactless measure of the 2D electron density in a GaAs quantum well.” In: *Applied Physics Letters* 110.26 (June 2017), p. 262104.

[81] M. S. Skolnick et al. “Observation of a Many-Body Edge Singularity in Quantum-Well Luminescence Spectra.” In: *Phys. Rev. Lett.* 58 (20 1987), pp. 2130–2133.

[82] M. B. Panish et al. “Temperature Dependence of the Energy Gap in GaAs and GaP.” In: *Journal of Applied Physics* 40.1 (Jan. 1969), pp. 163–167.

[83] Y. Mei et al. “Optical Properties of a Wrinkled Nanomembrane with Embedded Quantum Well.” In: *Nano Letters* 7.6 (2007). PMID: 17461606, pp. 1676–1679.

[84] S. Tarucha et al. “Exciton binding energy in GaAs quantum wells deduced from magneto-optical absorption measurement.” In: *Solid State Communications* 52.9 (1984), pp. 815–819.

[85] A. Berrier et al. “Carrier transport through a dry-etched InP-based two-dimensional photonic crystal.” In: *Journal of Applied Physics* 101.12 (June 2007), p. 123101.